

Novel Radio-over-Fiber Systems and Microwave Doppler Frequency Shift Measurement Using Standard Silicon Photonics Building Blocks

Nieuwe radio-over-vezelsystemen en microgolf-doppler-frequentieverschuivingsmeting met standaardbouwstenen van het silicium-fotonica-platform

Zhenzhou Tang

**Promotoren: prof. dr. ir. D. Van Thourhout, prof. dr. S. Pan
Proefschrift ingediend tot het behalen van de graad van
Joint Doctor in de ingenieurswetenschappen: fotonica**



**Vakgroep Informatietechnologie
Voorzitter: prof. dr. ir. B. Dhoedt
Faculteit Ingenieurswetenschappen en Architectuur
Academiejaar 2019 – 2020**

**Department of Electronic Science and Technology
College of Electronic and Information Engineering
Academic year 2019 – 2020**

ISBN
NUR 950
Wettelijk depot:



Universiteit Gent
Faculteit Ingenieurswetenschappen en Architectuur
Vakgroep Informatietechnologie

Nanjing University of Aeronautics and Astronautics
College of Electronic and Information Engineering
Department of Electronic Science and Technology

Promotors:

prof. dr. ir. Dries Van Thourhout (Universiteit Gent)
prof. dr. Shilong Pan (Nanjing University of Aeronautics and Astronautics)

Exam Commission:

Prof. dr. ir. Fangzheng Zhang (Chair)	Nanjing University of Aeronautics and Astronautics
prof. dr. ir. Filip De Turck (co-chair)	Universiteit Gent
prof. dr. ir. Gunther Roelkens	Universiteit Gent
prof. dr. ir. Xin Yin	Universiteit Gent
Prof. dr. Dan Zhu	Nanjing University of Aeronautics and Astronautics
prof. dr. ir. Mingshan Zhao	Dalian University of Technology
prof. dr. ir. Yiping Cui	Southeast University

Universiteit Gent
Faculteit Ingenieurswetenschappen en Architectuur
Vakgroep Informatietechnologie
Technologiepark-Zwijnaarde 126 iGent B-9052 Gent, België

Tel.: +32 (0) 9264 3316
Fax.: +32 (0) 9264 3593

Nanjing University of Aeronautics and Astronautics
College of Electronic and Information Engineering
29 Jiangjun Avenue, Nanjing, Jiangsu, 211106, China

Tel.: +86 (025) 8489 2452

Acknowledgements

Studying in the Photonics Research Group (PRG) of Ghent University (UGent, Belgium) is definitely one of the most important experiences in my life.

Before I went to the PRG in 2017, I mainly studied on the Microwave Photonic (MWP) systems at Nanjing University of Aeronautics and Astronautics (NUAA, China), under the guidance of Prof. Shilong Pan. At that time, the knowledge and skills I had about photonic integrated circuits are quite insufficient. Therefore, I want to express my sincere gratitude to Dries for his 'courage' to accept a layman like me as a visiting PhD student, and his effort to help me to change my role from a visiting PhD student to a joint PhD student afterwards. I feel lucky that I can meet such a nice supervisor. His smart intelligence, patient directions and insightful opinions make my research much easier. Every time I discussed with him, I can always obtain something new and helpful from him. Without his guidance, I cannot finish this thesis. His enthusiasm in research taught me how to do research in a rigorous and patient way, which is quite important for my career in the future. Hope Dries can visit China again!

I would also thank my Chinese supervisor professor Shilong Pan. He encouraged me to apply the visiting PhD student position of UGent when I applied for the scholarship of China Scholarship Council (CSC). He also helped me to promote the sign of the joint PhD student agreement. Thanks very much!

Special thanks also go to Prof. Roel Beats and Prof. Gunther Roelkens. Prof. Roel Beats built such a fantastic group with so many interesting activities. During my one-year stay in this group, I attended the 2017 and 2018 Photonics Day (I also won a medal in the 2017 Photonics Day^^), 2018 Photonics Dinner, 2017 Photonics Retreat, 2018 Silicon Photonics Summer School and many other meaningful activities. Prof. Gunther Roelkens

allowed me to do some experiments on Jing's chip, and helped me to revise my paper.

I'd like to express my gratitude to other professors, administrative staff and supporting staff, who helped me a lot either directly or indirectly. Thanks a lot!

Besides the professors and administrative staff, my should also thank the kind and intelligent colleagues. Their expertise in respective topics have offered me a lot of knowledge through discussions or presentations. Especially thanks to Kasper and Paul. Kasper helped me during the design of my first silicon photonic chip, and also taught me to do the high-speed measurements. Paul taught me the knowledge about optomechanics effect (i.e., stimulated Brillouin scattering effect) in the silicon waveguide. He shown me how to design, fabricate and characterize this kind of chip. I am grateful for all of you.

Now, my gratitude goes to my Chinese colleagues, including Yufei, Jing, Yang, Qiang, Yuxin, Xiangfeng, Ruijun, Naidi, Haolan, Yuting, Yunpeng, Ang, Xiaomin, Xiaoning, Mi, Chonghuai, Chupao, Hong, Yanlu and Guanyu (forgive me if some names are missing). We organized countless and various get-togethers, such as hot-pot party, BBQ party, badminton, boating (at Dinant), squash, Go-kart, etc., which contributes to most of my fun in the living at Ghent. I wish this friendship can last forever.

Last but not the least, I thank my families. Thanks to my parents for bring me to this world in 1990. They support me all the time, no matter who I am, where I am, what I have got. Thanks to my twin brother and my sister, thanks for their understanding for all my decisions. Thanks for their continuous love and support! Your love really means a lot to me!

*Zhenzhou Tang
Nanjing, November 2019*

Contents

Acknowledgements.....	i
Contents.....	iii
List of Figures.....	v
List of Tables.....	ix
List of Acronyms.....	xi
Summary.....	xv
Samenvatting.....	xxv
Chapter 1 Introduction	1
1.1 Microwave photonics	1
1.2 Photonic integrated circuit	3
1.3 Integrated microwave photonics.....	5
1.4 The work presented in this thesis.....	7
1.5 Publications	8
References.....	9
Chapter 2 RoF system based on silicon ring modulator	15
2.1 Introduction.....	15
2.2 Principle of silicon ring modulator	20
2.3 Full-duplex radio-over-fiber system with local single sideband modulation and remote carrier reuse	25
2.4 Conclusion.....	32
Reference.....	33
Chapter 3 RoF system based on III-V-on-silicon transceiver.....	39
3.1 Introduction.....	39
3.2 Transfer printing technology	44
3.3 Full-duplex RoF system based on transfer-printed III-V-on-silicon transceiver.....	47
3.4 Conclusion.....	56
Reference.....	57
Chapter 4 Microwave Doppler frequency shift measurement based on	

coherent receiver.....	63
4.1 Introduction.....	63
4.2 Integrated coherent receiver.....	76
4.3 Photonic Doppler frequency shift measurement based integrated coherent receiver.....	89
4.4 Conclusion.....	94
Reference.....	95
Chapter 5 Conclusions and perspectives	101
5.1 Overview.....	101
5.2 Perspectives	102
Reference.....	109

List of Figures

Fig. 1. Silicon ring modulator characterization	xvi
Fig. 2. The structure and transmission performance of the proposed full-duplex RoF system	xvii
Fig. 3. Integrated III-V-on-silicon transceiver	xviii
Fig. 4. The proposed full-duplex RoF system based on the III-V-on-silicon transceiver	xix
Fig. 5. The proposed silicon coherent receiver	xxi
Fig. 6. Photonic DFS measurement system based on the integrated coherent receiver	xxii
Fig. 1. Karakterisatie van siliconenringmodulator	xxvi
Fig. 2. Structuur en transmissieprestaties van het voorgestelde full-duplex RoF-systeem	xxvii
Fig. 3. Geïntegreerde III-V-op-siliconen transceiver	xxviii
Fig. 4. Het voorgestelde full-duplex RoF-systeem op basis van de III-V-on-silicon transceiver	xxx
Fig. 5. De voorgestelde siliconen coherente ontvanger	xxxii
Fig. 6. Fotonisch DFS-meetsysteem op basis van de geïntegreerde coherente ontvanger	xxxiii
Fig. 1.1. Typical MWP systems	2
Fig. 1.2. Typical photonic integrated circuits based on different materials ..	3
Fig. 1.3. Typical silicon-based integrated circuits	5
Fig. 1.4. Typical IMWP circuits based on silicon photonics	6
Fig. 2.1. Typical structure of a radio over fiber system	16
Fig. 2.2. Different SSB modulation methods	18
Fig. 2.3. RoF systems enabled integrated circuits	19

Fig. 2.4. All-pass silicon ring resonator	21
Fig. 2.5. Transmission response of an all-pass silicon ring resonator	21
Fig. 2.6. Principle of silicon ring modulator	23
Fig. 2.7. Cross section of different silicon ring modulator structures based on different mechanisms for manipulation of the free carrier concentrations	23
Fig. 2.8. Different silicon ring modulators	24
Fig. 2.9. Ring modulator and characterization	26
Fig. 2.10. Schematic diagram of the proposed full-duplex RoF system based on an integrated silicon ring modulator	27
Fig. 2.11. Downstream RF signal obtained in the RRH	29
Fig. 2.12. Measured EVM versus received optical power for back-to-back (b2b) and 5-km downstream link	29
Fig. 2.13. Upstream RF signal obtained in the CO	30
Fig. 2.14. Measured EVM versus received optical power for b2b and 5-km upstream link	30
Fig. 2.15. Bias independence and stability	31
Fig. 3.1. Processing flow of wafer bonding	40
Fig. 3.2. Processing flow of III-V devices after wafer bonding	40
Fig. 3.3. Semiconductor optical fiber based on wafer-bonding	41
Fig. 3.4. III-V-on-silicon laser	42
Fig. 3.5. Typical process for III-V-on-silicon integration by direct epitaxy	43
Fig. 3.6. An example of III-V-on-silicon laser based on direct epitaxy	43
Fig. 3.7. Illustration of the transfer printing concept	44
Fig. 3.8. Schematic flow of the transfer printing process	45
Fig. 3.9. Example of devices based on transfer printing	46
Fig. 3.10. Cross-section of the transfer-printed III-V-on-silicon transceiver	47
Fig. 3.11. Static characterization of the ring modulator	48
Fig. 3.12. Electro-optic modulation bandwidth of the ring modulator with 1 V DC bias	48
Fig. 3.13. III-V PD and transfer printed transceiver	49
Fig. 3.14. Performances of the transfer printed III-V PD	50
Fig. 3.15. Structure of the full-duplex RoF system based on the integrated III-V-on-silicon transceiver	51

Fig. 3.16. Measured transmission performance of the downstream link	52
Fig. 3.17. Measured transmission performance of the upstream link	53
Fig. 3.18. Spurious free dynamic range (SFDR) of the RoF system	54
Fig. 3.19. Measured EVM versus the wavelength offset	54
Fig. 3.20. Illustration of a full-integrated transceiver with transfer-printed LD and PD	56
Fig. 4.1. Photonic DFS measurement system based on FWM in HNLf	65
Fig. 4.2. Photonic DFS measurement system based on a microwave photonic mixer by using cascaded MZMs	67
Fig. 4.3. Photonic DFS measurement system with direction identification	68
Fig. 4.4. DFS measurement system with direction identification based on a photonic I/Q mixer	70
Fig. 4.5. DFS measurement system with direction identification based on a I/Q mixer by using a 90-degree optical hybrid	73
Fig. 4.6. Different types of 90-degree optical hybrid	78
Fig. 4.7. The proposed 90-degree optical hybrid based on silicon MMI	79
Fig. 4.8. Simulated mode distributions of the proposed MMI	81
Fig. 4.9. Simulation of wavelength dependence of the proposed MMI	82
Fig. 4.10. Calculated power ratio between the positive and negative components of the complex signal versus the phase deviation θ	84
Fig. 4.11. Simulation of fabrication tolerance of the proposed MMI	85
Fig. 4.12. Proposed BPD	86
Fig. 4.13. Performances of the single-ended PD	87
Fig. 4.14. The proposed silicon coherent receiver	87
Fig. 4.15. Photonic DFS measurement system based on the integrated coherent receiver	90
Fig. 4.16. Measured optical spectra of the proposed DFS system	91
Fig. 4.17. Measured electrical spectrum and electrical waveform of the DFS when the transmitted frequency is 20 GHz and the echo frequency is 20.005 GHz	92
Fig. 4.18. Measured electrical spectrum and electrical waveform of the DFS when the transmitted frequency is 20 GHz and the echo frequency is 20.005 GHz	92
Fig. 4.19. Measured DFS and measurement error when the transmitted	

frequency is 20 GHz and the DFS is changed from -100 kHz to +100 kHz. Resolution bandwidth and video bandwidth of the electrical spectrum analyser are 1 Hz	93
Fig. 4.20. Measured DFS and measurement error when the transmitted frequency is 10 GHz and the DFS is changed from -100 kHz to +100 kHz. Resolution bandwidth and video bandwidth of the electrical spectrum analyser are 1 Hz	93
Fig. 5.1. Linearized ring modulator	103
Fig. 5.2. Wavelength-locking of the ring modulator	104
Fig. 5.3. Instantaneous frequency measurement system based on a silicon ring modulator and a reflector	104
Fig. 5.4. Phase-stable RF signal transmission based on a silicon ring modulator.	106
Fig. 5.5. Future work of coherent receiver	108

List of Tables

Tab 1.1. Comparison between MWP system and conventional microwave system	2
Tab 2.1. Comparison of silicon ring modulators and LiNbO ₃ MZM	25
Tab 3.1. Layer stack for the O-band III-V PD	49
Tab 4.2. Comparison between 90-degree optical hybrid and the electrical quadrature hybrid coupler and microwave photonic phase shifter	76
Tab 4.2. Key parameters of the designed MMI-based optical hybrid	79
Tab 4.3. Comparison of state-of-the-art coherent receivers and the receiver used in this thesis	88
Tab 4.4. Performances comparison between the proposed and state-of-the-art DFS measurement systems	94

List of Acronyms

ADC	Analog to Digital Converter
AOM	Acousto-Optic Modulator
AR	Augmented Reality
AWG	Arrayed Waveguide Grating
BiDi	Bidirectional
BPD	Balanced Photodetector
CMMR	Common Mode Rejection Ratio
CO	Central Office
CROW	Coupled Resonator Waveguide
CS-DSB	Carrier-Suppressed Double Sideband
CS-SSB	Carrier-Suppressed Single Sideband
DBR	Distributed Bragg Reflector
DFB	Distributed Feedback
DFS	Doppler Frequency Shift
DMZM	Dual-Drive Mach-Zehnder Modulator
DPMZM	Dual-Parallel Mach-Zehnder Modulator
DSP	Digital Signal Processing
EAM	Electroporation Modulator
EDFA	Erbium Doped Fiber Amplifier
ER	Extinction Ratio
EVNA	Electrical Vector Network Analyzer
EW	Electrical Warfare
EMI	Electromagnetic Interference
EVM	Error Vector Magnitude
FBG	Fiber Bragg Grating
FIR	Finite Impulse Response
FPGA	Field Programmable Gate Array
FSR	Free Spectral Range

FWHM	Full Width at Half Maximum
FWM	Four-Wave Mixing
HNLF	Highly Nonlinear Fiber
IF	Intermediate Frequency
IIR	Infinite Impulse Response
IMWP	Integrated Microwave Photonics
LED	Light Emitting Diode
LPF	Low Pass Filter
MITP	Minimum Transmission Point
MLL	Mode-Locked Laser
MMI	Multimode Interference
MPF	Microwave Photonic Filter
MPW	Multi-Project Wafer
MWP	Microwave Photonics
OAM	Optical Modulation Amplitude
OBPF	Optical Bandpass Filter
OEO	Optoelectronic Oscillator
OOK	On/Off Keying
OPLL	Optical Phase Lock Loop
OVDL	Optical Variable Delay Line
PC	Polarization Controller
PD	Photodetector
PDK	Process Design Kit
PIC	Photonics Integrated Circuit
PoIM	Polarization Modulator
PM	Phase Modulator
PMF	Polarization Maintaining Fiber
QTP	Quadrature Transmission Point
RBW	Resolution Bandwidth
RoF	Radio-over-Fiber
RRH	Remote Radio Head
RSOA	Reflective Semiconductor Optical Amplifier
SAR	Synthetic Aperture Radar
SBS	Stimulated Brillouin Scattering
SMF	Single Mode Fiber

SOA	Semiconductor Optical Amplifier
SOI	Silicon-on-Insulator
SSB	Single Sideband
SUT	Signal-Under-Test
TW	Traveling Wave
VBW	Video Bandwidth
VR	Virtual Reality
WDM	Wavelength Division Multiplexer
XGM	Cross Gain Modulation
XPM	Cross Phase Modulation
XPolM	Cross Polarization Modulation

Summary

Microwave photonics (MWP) is an interdisciplinary field that combines microwave technology and optical technology to realize numerous microwave functions, including microwave signal generation, processing, distribution and control. Thanks to its advantages in terms of wide bandwidth, low transmission loss, light weight and immunity to electromagnetic interference (EMI), MWP is regarded as one of the most promising candidates for applications such as next-generation wireless communications, communication satellites, sensor networks, synthetic aperture radars (SARs), instrumentations and electrical warfare (EW) systems in the future. Although some exciting results have been reported, most of the MWP systems still suffer from poor reliability, a bulky configuration, high cost and large power consumption. The main reason is that most of the conventional MWP systems are built based on discrete optical and electrical devices. These problems can be solved by integrated silicon photonic circuits. With photonic integration, one can achieve a reduction of footprint, reduced inter-element coupling loss, reduced packaging loss as well as reduced power dissipation. Thus, some interesting results in the domain of integrated MWP have been proposed very recently.

With this background, we aim to develop MWP systems using integrated standard silicon photonic building blocks such as silicon ring modulators and multimode interference (MMI) waveguides integrated with detectors originally designed as a coherent receiver. By exploring the feasibility of using these silicon building blocks in an MWP system, we aim to find a low-cost solution for some MWP applications. In a first project, a C-band silicon ring modulator is used to realize a full-duplex radio-over-fiber (RoF) communication system with local single-sideband (SSB) modulation and remote carrier reuse. Then, the C-band silicon ring modulator is co-integrated with an O-band III-V photodetector (PD) through the transfer-printing technology to construct a III-V-on-silicon RoF transceiver. Based on the III-V-

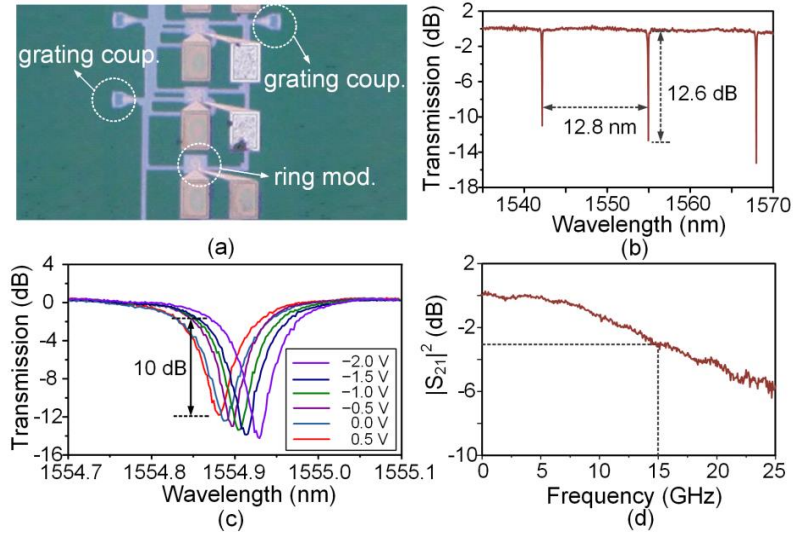


Fig. 1. Silicon ring modulator characterization. (a) Microscopic image, (b) transmission response, (c) resonant wavelength shift versus bias voltage increasing from -2 to 0.5 V with a step of 0.5 V, and (d) normalized $|S_{21}|^2$ response of the ring modulator.

on-silicon transceiver, a bidirectional (BiDi), wavelength-multiplexed full-duplex RoF system is constructed. In a second subproject, an integrated silicon coherent receiver, which is assembled with an optical 90-degree hybrid based on an MMI waveguide and a pair of balanced PDs (BPDs), is used to build a Doppler frequency shift (DFS) measurement system.

Fig. 1(a) shows the microscopic image of the silicon ring modulator together with two grating couplers, which was fabricated in the imec iSIPP25G platform. The electro-optic modulation is realized by the plasma dispersion effect in a PN-doped silicon waveguide. The static response is measured and shown in Fig. 1(b). The free spectral range (FSR) is about 12.8 nm, which is determined by the radius of the ring modulator (i.e., 7.5 μm in this case). The extinction ratio (ER) around 1554.96 nm is about 12.6 dB. The resonant wavelength at different bias voltages are presented in Fig. 1(c), from which can be seen that the extinction ratio is about 10 dB for a 2.5 Vpp voltage swing. The electro-optic dynamic response is also measured by an electrical vector network analyser (EVNA) and presented in Fig. 1(d). The 3-dB bandwidth is about 15 GHz at -1 V bias.

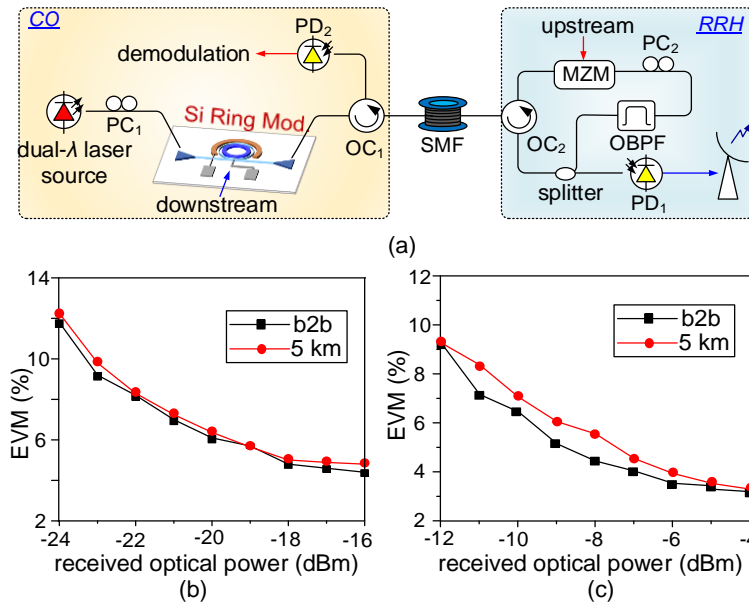


Fig. 2. The structure and transmission performance of the proposed full-duplex RoF system. (a) Schematic diagram of the system. (b) EVM versus received optical power for back-to-back (b2b) and 5-km downstream link, and (c) EVM versus received optical power for b2b and 5-km upstream link. PC: polarization controller; PD: photodetector; SMF: single-mode fiber; MZM: Mach-Zehnder modulator; OC: optical circulator; OBPF: optical bandpass filter; CO: central office; RRH: remote radio head.

Since only the optical carrier around the resonant wavelength can obtain sufficient modulation efficiency, optical SSB modulation can be realized by injecting two optical carriers into the ring modulator, and of which one is aligned to the resonant wavelength of the ring modulator. Based on this idea, a full-duplex RoF system with local SSB modulation and remote carrier reuse is proposed and experimentally demonstrated. The diagram of the proposed full-duplex RoF system is depicted in Fig. 2(a). In the central office (CO), two optical carriers produced by a dual-wavelength (dual- λ) laser source is sent to the ring modulator. After passing through the ring modulator, one of the optical carriers is modulated by the baseband data applied to the ring modulator. Then the SSB-modulated signal is transmitted to the remote radio head (RRH) by low loss single mode fiber (SMF). In the RRH, the optical signal is split into two portions. One portion is directly sent to a PD to realize photodetection. The other portion is sent to an optical bandpass filter (OBPF),

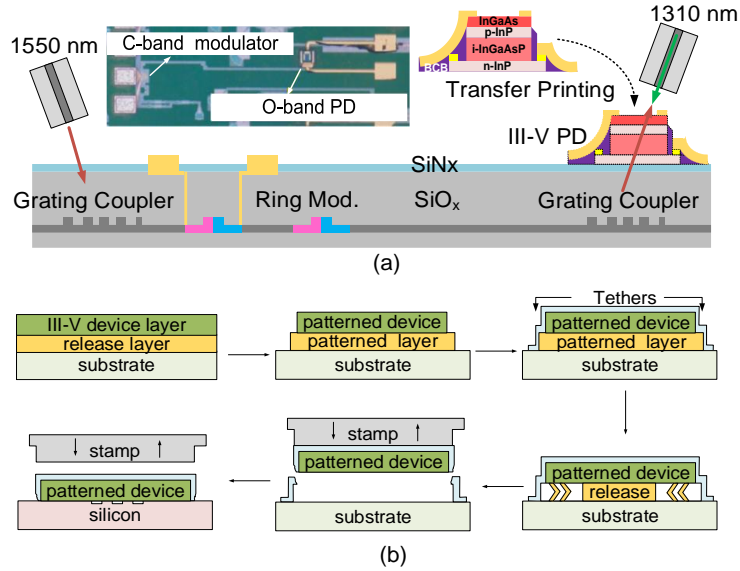


Fig. 3. Integrated III-V-on-silicon transceiver. (a) Cross-section and microscopic figure of the integrated transceiver (b) schematic flow of the transfer printing process.

which selects the unmodulated optical carrier. Then the selected unmodulated optical carrier is reused as the optical carrier for the upstream link, which is modulated with the upstream data by a Mach-Zehnder modulator (MZM). The modulated optical upstream signal is transmitted back to the CO and converted back to an electrical signal through another PD.

In the experiment, the frequency spacing of the dual- λ laser source is 20 GHz. For the downstream link, the downstream data is a 1-GHz intermediate frequency (IF) signal carrying 250-Mbaud 16QAM data. Fig. 2(b) shows the performance of the downstream link with and without 5-km fiber link. As can be seen, for a received optical power of -18 dBm, the error vector magnitude (EVM) is lower than 5%. Since the SSB modulation can combat the fiber dispersion, negligible deterioration in the EVM can be observed after fiber transmission. For the upstream link, the unmodulated optical carrier selected in the RRH is re-modulated by a 10-GHz RF signal carrying 50-Mbaud 16QAM data. Fig. 2b shows the measured EVM as a function of the received optical power for the upstream link. As can be seen, when the received optical power is larger than -7 dBm, the EVM is lower than 5%.

To further reduce the system complexity, an O-band III-V PD is integrated

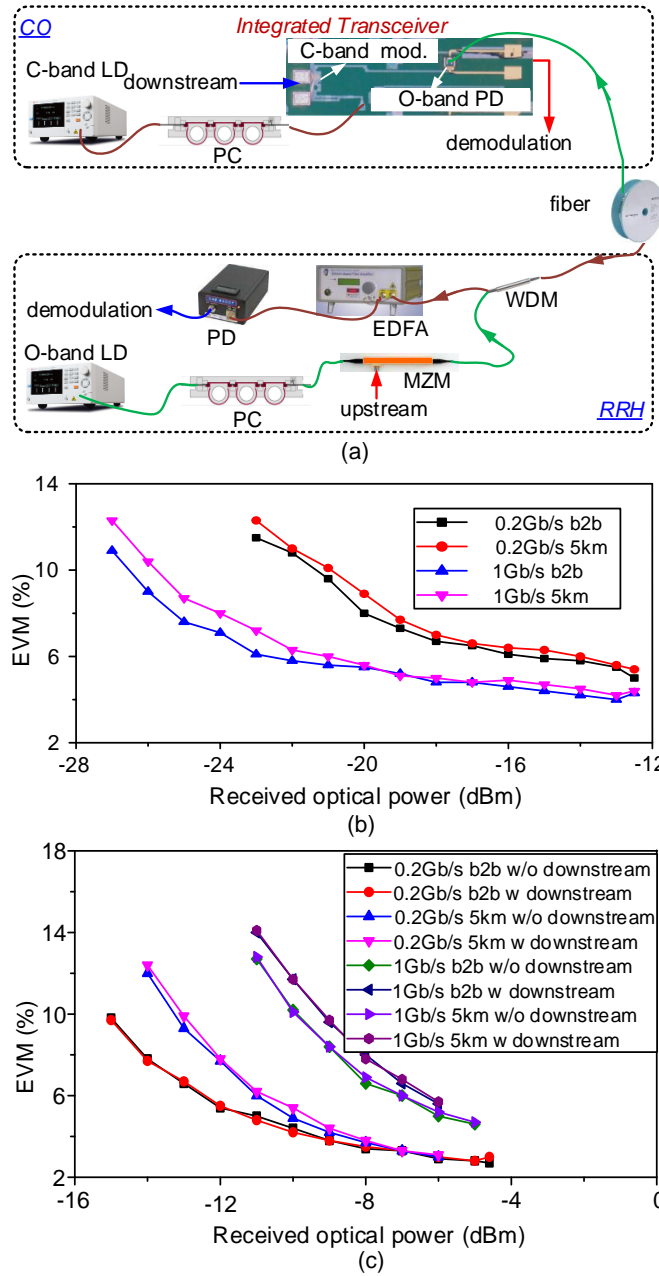


Fig. 4. The proposed full-duplex RoF system based on the III-V-on-silicon transceiver. (a) Schematic diagram of the system structure. (b) Measured EVM versus received optical power for back-to-back (b2b) and 5-km downstream link. (c) Measured EVM versus received optical power for b2b and 5-km upstream link with the downstream link operational or off.

communication systems, of which the C-band silicon ring modulator is used for the electro-optic modulation of the downstream data and the O-band III-V PD is applied for the photodetection of the upstream data. The proposed III-V-on-silicon transceiver is shown in Fig. 3(a). Again, two grating couplers are used for coupling of the light. Between the two grating couplers, a silicon ring modulator is integrated, which is operated at the C-band. A III-V PD is placed on top of the grating coupler, whose working frequency range is designed at the O-band. To achieve the III-V-on-silicon integration, a technology called transfer printing is employed. The schematic processing flow is shown in Fig. 3(b). First of all, III-V PD is fabricated on the source substrate. Then it is encapsulated by a 2.5- μm thick photoresist layer with narrow tethers. Next, wet etching is used to etch the release layer (1 μm thick InGaAs) and undercut the pre-fabricated PD. Finally, a PDMS stamp is used to pick-up and print the III-V PD to the target substrate (SOI in this paper).

Based on the proposed III-V-on-silicon transceiver, a full-duplex bidirectional RoF system is demonstrated, as shown in Fig. 4(a). For the downstream link, a C-band optical carrier is coupled into the silicon ring modulator through a polarization controller (PC) in the CO. The downstream signal applied to the ring modulator is a 10-GHz RF signal carrying 50- and 250-Mbaud 16QAM data. The modulated optical downstream signal is coupled out via another grating coupler and the transfer printed PD on top of it. After a 5-km optical fiber link, the optical signal is transmitted to the RRH. In the RRH, an electrical downstream RF signal is recovered when the optical signal is directly sent to a PD. For the upstream link, an O-band optical carrier is produced by an O-band laser source and sent to an O-band MZM, which is driven by an upstream signal. The upstream signal is an 8-GHz RF signal carrying 50- and 250-Mbaud 16QAM data. The optical signal at the output of the O-band MZM is duplexed with the C-band downstream signal by a wavelength division multiplexer (WDM) and transmitted back to the CO through the same optical fiber. In the CO, the O-band signal is launched to the transfer-printed PD, and an electrical signal is thereby obtained. Fig. 4(b) shows the transmission performance of the downstream link. As can be seen, when the received optical power is >-22 dBm, the EVM is $<6\%$, for the transmission of the 0.2-Gb/s 16QAM data. When the downstream signal is a 1-Gb/s 16QAM data, the measured EVM is $<6\%$ if the received optical power

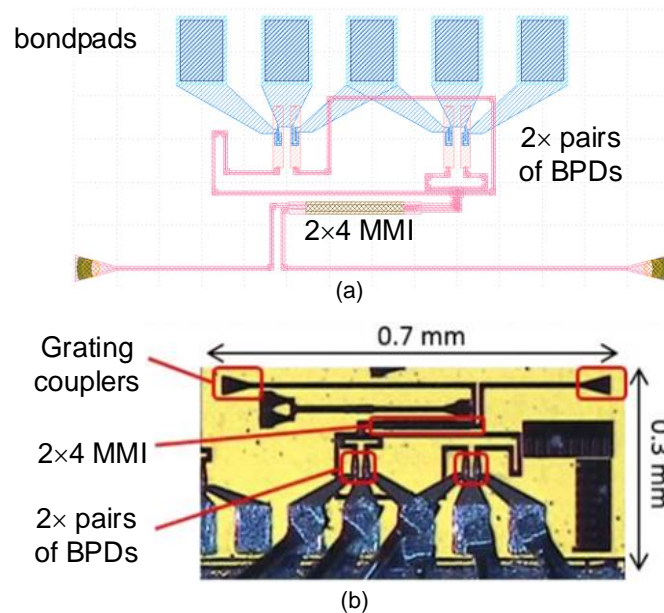


Fig. 5. The integrated silicon coherent receiver. (a) Layout and (b) microscope picture of the coherent receiver.

is > -15 dBm. Fig. 4(c) presents the transmission performance of the upstream link with the downstream link operational or off. For the 0.2-Gb/s upstream link, the obtained EVM is lower than 6% after 5-km fiber transmission, when the received optical power is > -11 dBm. For the 1-Gb/s link, an EVM of $< 6\%$ is obtained when the received optical power is larger than -6 dBm. Besides, a slight deterioration in the EVM is introduced by the fiber transmission link, which may result from the relatively higher fiber transmission loss in the O-band. Further, the downstream link introduces neglectable influence on the upstream link, which can also be seen from the results shown in Fig. 4(c).

In addition to the ring modulator, an integrated silicon coherent receiver is functioned as a building block to realize microwave doppler frequency shift (DFS) measurement. Fig. 5 shows the integrated silicon coherent receiver, which consists of an MMI-based 90-degree optical hybrid and a pair of balanced PDs realized by two SiGe PDs working at the photocurrent subtraction mode. Making use of this silicon coherent receiver, a photonic DFS measurement system with a structure shown in Fig. 6(a) is proposed. The structure of the photonic DFS measurement system is presented in Fig. 6(a). An optical carrier is split into two branches and modulated by the

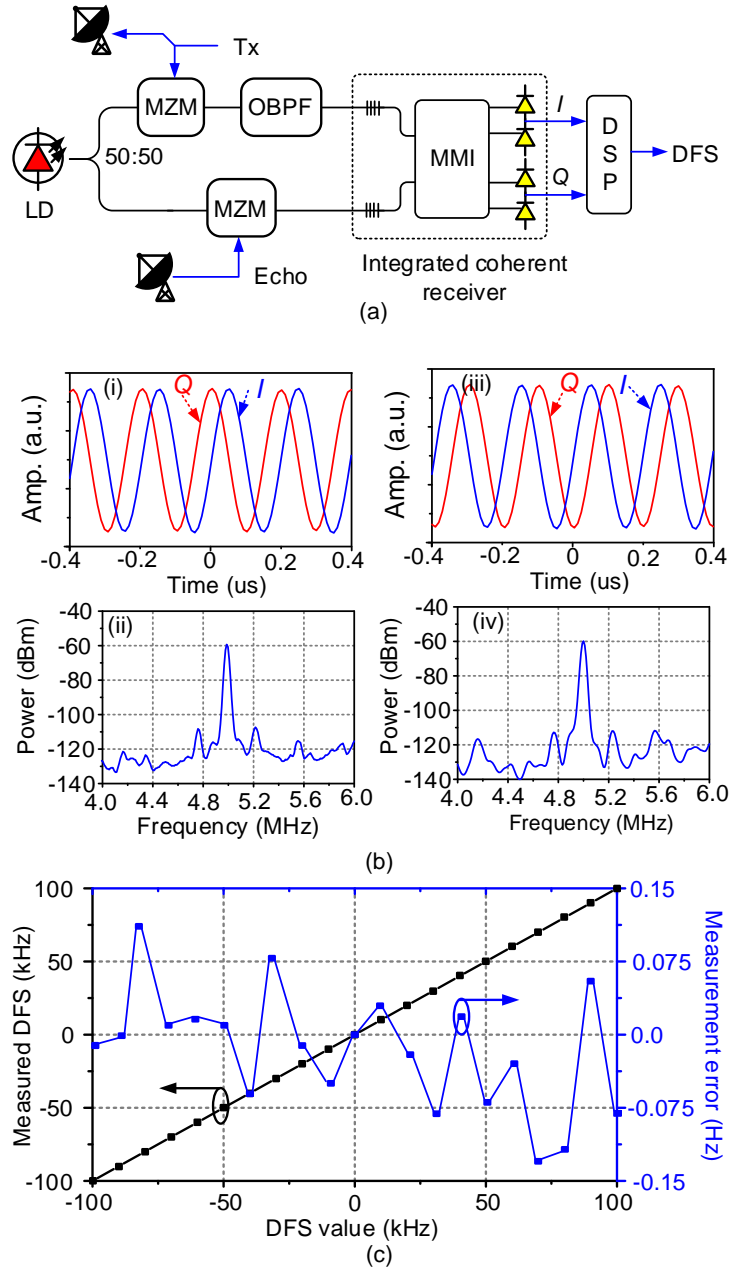


Fig. 6. Photonic DFS measurement system based on the integrated coherent receiver. (a) Schematic diagram. (b) Electrical waveforms of the negative (i) and positive (iii) 5 MHz DFS signals and (ii, iv) the corresponding electrical spectra. (c) Measured DFS and the measurement error.

transmitted signal and the echo signal, respectively. An optical bandpass

filter (OBPF) is inserted in the upper branch to select one of the 1st-order sidebands. Then the two optical signals are sent to the integrated coherent receiver as the *Signal* light and *Local Oscillator (LO)* light. Then a pair of quadrature IF signals (I and Q) can be obtained at the outputs of the two BPDs. Thus, the DFS value can be obtained by measuring the frequency of the IF signal and more importantly, the direction of the DFS can be identified by comparing the phase difference between the two quadrature outputs. If I is delayed with respect to Q , a positive DFS is derived. In contrast, a positive DFS is derived. The figures (i) and (ii) in Fig. 6(b) show the waveforms of the I and Q signals, and the electrical spectrum of the IF signal. As can be seen, the DFS value is 5 MHz and the direction is negative. The figures (iii) and (iv) in Fig. 6(b) present the waveforms and spectrum when a positive DFS is obtained. Fig. 6(c) depicts the measured DFS and the corresponding measurement error. The measurement error, by comparing the measured values with the theoretical ones, is less than ± 0.15 Hz.

In conclusion, photonics integrated circuits will play a more and more important role in future MWP systems to reduce the complexity and power consumption of the systems. In this work, we focus on RoF systems and photonic DFS measurement systems enabled by silicon photonic building blocks such as a silicon ring modulator and a 4-port MMI-based coherent receiver. A silicon ring modulator is applied to realize a full-duplex RoF system with local SSB modulation and remote carrier reuse. Besides, when co-integrating an O-band III-V PD by transfer printing, a III-V-on-silicon transceiver is achieved to implement a BiDi RoF system with a C-band downstream link and an O-band upstream link. Finally, a photonic DFS measurement system with direction identification based on a coherent receiver is also demonstrated.

Samenvatting

Microgolffotonica is een interdisciplinair vakgebied dat microgolf- en optische technologie combineert om functies zoals het genereren, verwerken en distribueren van microgolfsignalen te realiseren. Gegeven voordelen zoals brede bandbreedte, laag transmissieverlies, laag gewicht en immuniteit voor elektromagnetische interferentie, wordt microgolffotonica beschouwd als een van de meest veelbelovende kandidaten voor toepassingen in de volgende generatie draadloze communicatiesystemen, communicatiesatellieten, sensornetwerken, synthetische apertuurradars, algemene instrumentatie en defensie systemen. Hoewel al verschillende veelbelovende resultaten werden gerapporteerd, lijden de meeste microgolffotonicasystemen nog steeds onder beperkte betrouwbaarheid, te grote afmetingen, hoge kosten en een groot vermogenverbruik. De belangrijkste reden is dat de meeste tot dusver gedemonstreerde microgolffotonica systemen zijn gebouwd op basis van discrete optische en elektrische componenten. Deze problemen kunnen worden opgelost door geïntegreerde silicium fotonische circuits te gebruiken. Met fotonische integratie kunnen de dimensies worden gereduceerd, kan het koppelverlies tussen de bouwblokken worden gereduceerd, en kan verminderde vermogensdissipatie worden bekomen. Aldus zijn zeer recent enkele interessante resultaten op het gebied van geïntegreerde microgolffotonica voorgesteld.

Dit in acht nemende, is het ons doel microgolffotonica systemen te ontwikkelen met behulp van geïntegreerde silicium fotonische bouwstenen zoals silicium ringmodulatoren en multimode interferentie golfgeleiders (MMI) geïntegreerd met detectoren die oorspronkelijk zijn ontworpen als een coherente ontvanger. Door de haalbaarheid van het gebruik van deze siliciumbouwstenen in een MWP-systeem te onderzoeken, proberen we een goedkope oplossing te vinden voor sommige MWP-toepassingen. In een

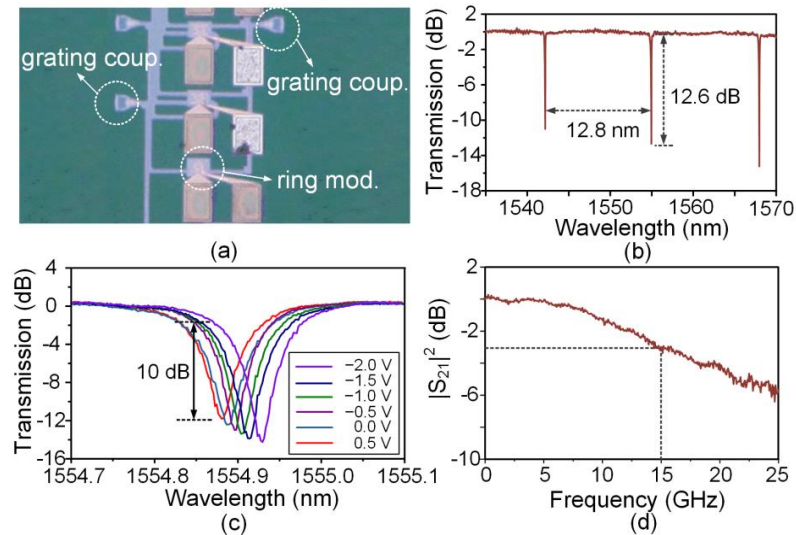


Fig. 1. Karakterisatie van siliciumringmodulator. (a) Microscopisch beeld, (b) transmissierespons, (c) resonantiegolflengteverschuiving versus voorspanningsspanning toenemend van -2 tot 0,5 V met een stap van 0,5 V, en (d) genormaliseerde $|S_{21}|^2$ respons van de ringmodulator.

eerste project werd een C-band siliciumringmodulator gebruikt om een full-duplex radio-over-fiber (RoF) communicatiesysteem met lokale single-sideband (SSB) modulatie en drager hergebruik te realiseren. Vervolgens werd de C-band siliciumringmodulator geïntegreerd met een O-band III-V fotodetector via de transfer-printtechnologie om een III-V-op-silicium RoF-transceiver te construeren. Gebaseerd op de III-V-on-silicon transceiver, is een bidirectioneel, golflengte-gemultiplexeerd volledig full-duplex RoF-systeem geconstrueerd. In een tweede subproject wordt een geïntegreerde silicium-coherente ontvanger, geassembleerd met een optische 90-graden hybride op basis van een multimode interferentie golfgeleider en een paar gebalanceerde fotodetectoren, gebruikt om een Doppler frequency shift (DFS) meetsysteem te bouwen.

Fig. 1(a) toont het microscopische beeld van de siliciumringmodulator samen met twee roosterkoppelaars, die werd vervaardigd in het imec iSIPP25G-platform. De elektro-optische modulatie is gebaseerd op het plasmadispersie-effect in een PN-gedoteerde siliciumgolfgeleider. De

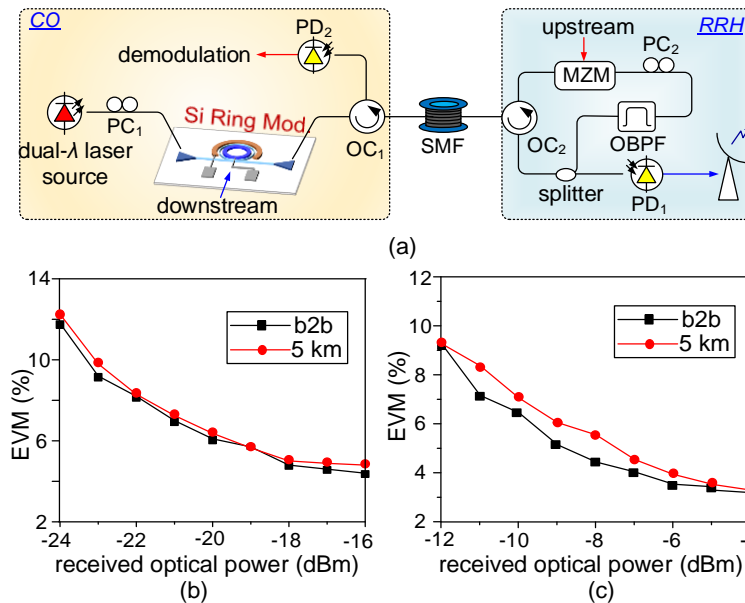


Fig. 2. Structuur en transmissieprestaties van het voorgestelde full-duplex RoF systeem. (a) Schematische weergave van het systeem. (b) EVM versus ontvangen optisch vermogen voor back-to-back (b2b) en 5 km downstream-verbinding, en (c) EVM versus ontvangen optisch vermogen voor b2b en 5 km upstream-verbinding. PC: polarisatiecontroller; PD: fotodetector; SMF: single-mode vezel; MZM: Mach-Zehnder modulator; OC: optische circulator; OBPF: optisch banddoorlaatfilter; CO: centraal kantoor; RRH: radiokop op afstand.

opgemeten statische respons is getoond in Fig. 1(b). Het vrije spectrale bereik (FSR of periode) is ongeveer 12,8 nm, en wordt bepaald door de straal van de ringmodulator (7,5 μm in dit geval). De extinctieverhouding rond 1554,96 nm is ongeveer 12,6 dB. De resonantiegolflengte bij verschillende spanningen wordt weergegeven in Fig. 1(c), waaruit blijkt dat de extinctieverhouding ongeveer 10 dB is voor een spanningsvariatie van 2,5 Volt. De elektro-optische dynamische respons werd ook gemeten met een elektrische vectornetwerkanalysator en is gepresenteerd in Fig. 1(d). De 3-dB bandbreedte is ongeveer 15 GHz bij -1 V bias.

Omdat alleen de optische drager rond de resonantiegolflengte sterk wordt gemoduleerd, kan optische SSB-modulatie worden gerealiseerd door twee optische dragers in de ringmodulator te injecteren, waarvan er één is uitgelijnd met de resonantiegolflengte van de ringmodulator. Op basis van

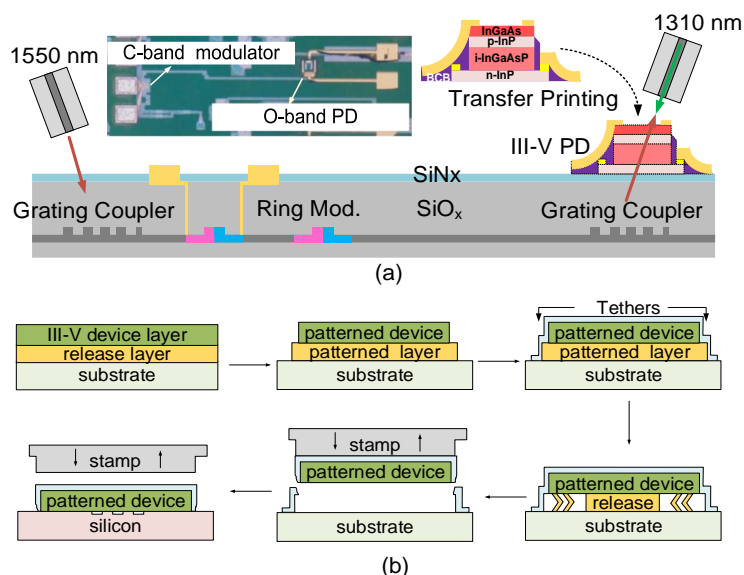


Fig. 3. Geïntegreerde III-V-op-siliconen transceiver. (a) Dwarsdoorsnede en microscopische afbeelding van de geïntegreerde transceiver (b) schematische stroom van het transferprintproces.

dit idee werd een full-duplex RoF-systeem met lokale SSB-modulatie en hergebruik op afstand voorgesteld en experimenteel aangetoond. Het diagram van het voorgestelde full-duplex RoF-systeem is afgebeeld in figuur 2 (a). In het central office worden twee optische dragers geproduceerd door een laserbron met dubbele golflengte (dual- λ) en naar de ringmodulator gestuurd. Na het passeren van de ringmodulator wordt een van de optische dragers gemoduleerd. Vervolgens wordt het SSB-gemoduleerde signaal naar de externe radio verzonden door een single-mode vezel met laag verlies. In de externe radio wordt het optische signaal in twee delen gesplitst. Eén portie wordt direct naar een fotodetector gestuurd om fotodetectie te realiseren. Het andere deel wordt verzonden naar een optisch banddoorlaatfilter, dat de niet-gemoduleerde optische drager selecteert. Vervolgens wordt de geselecteerde niet-gemoduleerde optische drager hergebruikt als de optische drager voor de stroomopwaartse verbinding, die wordt gemoduleerd met de stroomopwaartse gegevens door een Mach-Zehnder-modulator (MZM). Het gemoduleerde optische stroomopwaartse signaal wordt dan teruggestuurd naar het centrale kantoor en via een andere fotodetector weer omgezet in een elektrisch signaal.

In het experiment was de frequentieafstand van de dual- λ laserbron 20 GHz. Voor de stroomafwaartse verbinding, bestond het signaal uit 250 Mbaud 16QAM data. Fig. 2 (b) toont de prestaties van de stroomafwaartse verbinding met en zonder 5 km vezelverbinding. Zoals te zien, voor een ontvangen optisch vermogen van -18 dBm is de vector magnitude fout (EVM) lager dan 5%. Aangezien de SSB-modulatie tolerant is voor vezeldispersie, wordt de EVM nauwelijks slechter na transfer van het signaal door de vezel. Voor de stroomopwaartse verbinding wordt de niet-gemoduleerde optische draaggolf geselecteerd in de externe radio opnieuw gemoduleerd met een 10-GHz RF-signaal dat 50-Mbaud 16QAM-gegevens draagt. Fig. 2(b) toont de gemeten EVM als een functie van het ontvangen optische vermogen voor de stroomopwaartse verbinding. Zoals te zien, wanneer het ontvangen optische vermogen groter is dan -7 dBm, is de EVM lager dan 5%.

Om de systeemcomplexiteit verder te verminderen werd een O-band III-V fotodetector geïntegreerd met de C-band siliciumringmodulator om een transceiver te construeren voor RoF-communicatiesystemen, waarvan de C-band siliciumringmodulator wordt gebruikt voor de elektro-optische modulatie van de stroomafwaartse gegevens en de O-band III-V fotodetector wordt gebruikt voor de fotodetectie van de stroomopwaartse gegevens. De voorgestelde III-V-op-silicium zendontvanger wordt getoond in Fig. 3(a). Opnieuw worden twee roosterkoppelaars gebruikt voor het koppelen van het licht. Tussen de twee roosterkoppelaars is een siliciumringmodulator geïntegreerd, die in de C-band opereert. Een O-band III-V-fotodetector werd bovenop de roosterkoppelaar geplaatst. Daartoe werd een technologie genaamd "transfer printing" gebruikt. Het integratieschema wordt getoond in Fig. 3(b). Allereerst wordt de III-V fotodetector op zijn bronsubstraat gefabriceerd. Vervolgens wordt hij ingekapseld door een $2,5\text{-}\mu\text{m}$ dikke fotolaklaag. Vervolgens wordt nat etsen gebruikt om de sacrificiële laag (1 micrometer InGaAs) te etsen en de geprefabriceerde fotodetector van het substraat vrij te maken. Ten slotte wordt een PDMS-stempel gebruikt om de III-V-fotodetector op te nemen en af te drukken op het doelsubstraat (SOI in dit geval).

Met deze III-V-op-silicium zendontvanger, werd een full-duplex bidirectioneel RoF-systeem gedemonstreerd, zoals getoond in Fig. 4 (a). Voor de stroomafwaartse verbinding wordt een C-band optische drager

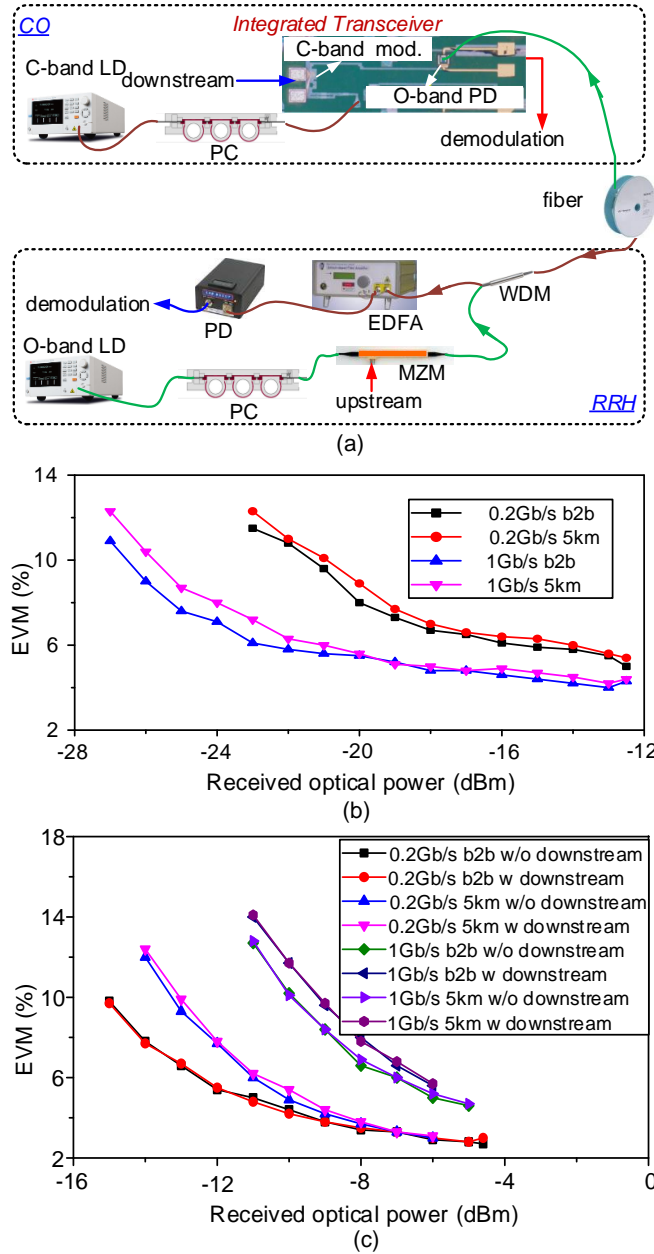


Fig. 4. Het voorgestelde full-duplex RoF-systeem op basis van de III-V-on-silicon transceiver. (a) Schematische weergave van de systeemstructuur. (b) Gemeten foutvectorgrootte versus ontvangen optisch vermogen voor back-to-back (b2b) en 5 km downstream-verbinding. (c) Gemeten foutvectorgrootte versus ontvangen optisch vermogen voor b2b en 5 km stroomopwaartse verbinding met de stroomafwaartse verbinding operationeel of uitgeschakeld.

central office. Het stroomafwaartse signaal dat wordt toegepast op de ringmodulator is een 10-GHz RF-sigitaal dat 50- en 250-Mbaud 16QAM-gegevens draagt. Het gemoduleerde optische stroomafwaartse signaal wordt via een andere rooster-koppelaar met de getransferprinte fotodetector er bovenop uitgekoppeld. Na een 5 km lange glasvezelverbinding, wordt het optische signaal dan terug naar het elektrische domein geconverteerd met een fotodetector. Voor de stroomopwaartse verbinding wordt een O-band optische drager geproduceerd door een O-band laserbron en gemoduleerd met een O-band MZM. Het stroomopwaartse signaal is een 8-GHz RF-sigitaal met 50- en 250-Mbaud 16QAM-gegevens. Het optische signaal aan de uitgang van de O-band MZM wordt door een golflengtemultiplexer en via dezelfde optische vezel als het afwaartse signaal teruggestuurd naar het central office. Daar wordt het O-bandsigitaal gedetecteerd door de getransferprinte fotodetector. Fig. 4(b) toont de performantie van de stroomafwaartse verbinding. Zoals te zien, wanneer het ontvangen optische vermogen groter is dan -22 dBm, is de EVM $< 6\%$ voor de overdracht van de 16QAM-gegevens van 0,2 Gb/s. Voor een 1-Gb/s 16QAM stroomafwaarts signaal is de EVM $< 6\%$ als het ontvangen optische vermogen groter is dan -15 dBm. Fig. 4(c) presenteert de performantie van de stroomopwaartse verbinding met de stroomafwaartse verbinding wel of niet operationeel. Voor de stroomopwaartse link van 0,2 Gb/s, is de EVM lager dan 6% na 5 km vezeloverdracht, wanneer het ontvangen optische vermogen groter is dan -11 dBm. Voor de 1-Gb/s link, wordt een EVM $< 6\%$ verkregen wanneer het ontvangen optische vermogen groter is dan -6 dBm. De vezelverbinding veroorzaakt een lichte verslechtering van de EVM, waarschijnlijk door het iets hogere verlies in de O-Band geïntroduceerd door de vezeltransmissieverbinding, die kan voortvloeien uit het relatief hogere vezeloverdrachtsverlies in de O-band. Verder heeft de stroomafwaartse verbinding een verwaarloosbare invloed op de kwaliteit van de stroomopwaartse verbinding, zoals kan worden afgeleid uit de resultaten getoond in Fig. 4(c).

In een tweede subproject demonstreerden we hoe een geïntegreerde silicium-coherente ontvanger kan fungeren als bouwsteen voor het realiseren van een microgolf DFS meting (Doppler Frequency Shift). Fig. 5 toont de geïntegreerde silicium-coherente ontvanger, die bestaat uit een op een MMI

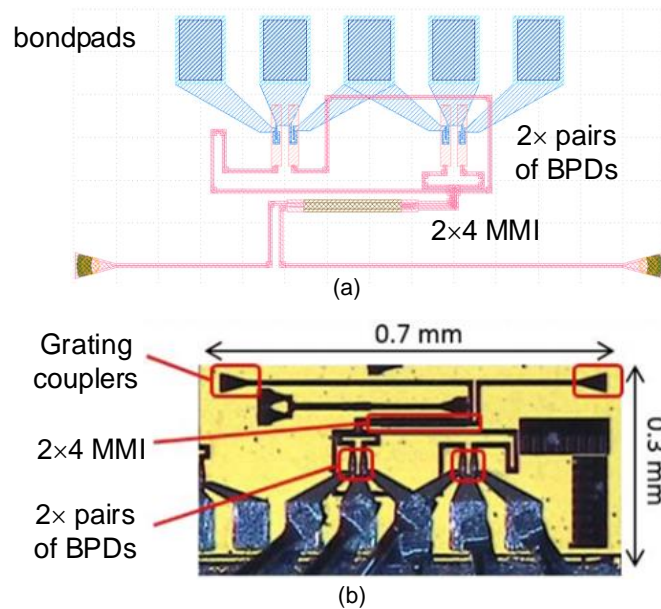


Fig. 5. De voorgestelde siliconen coherente ontvanger. (a) Layout en (b) microscoopbeeld van de coherente ontvanger.

gebaseerde 90-graden optische hybride en een paar gebalanceerde PD's gerealiseerd door twee geconnecteerde SiGe-fotodetectors. Gebruikmakend van deze silicium-coherente ontvanger, werd een fotonisch DFS-meetsysteem met de structuur getoond in Fig. 6(a) voorgesteld. De structuur van het fotonische DFS-meetsysteem is weergegeven in Fig. 6(a). Een optische draaggolf wordt opgesplitst in twee takken en gemoduleerd door respectievelijk het verzonden signaal en het echosignaal. Een optisch banddoorlaatfilter wordt in de bovenste tak geplaatst om een van de 1e orde zijbanden te selecteren. Vervolgens worden de twee optische signalen als signaal en lokal oscillator naar de geïntegreerde coherente ontvanger gestuurd. Dan kan een paar kwadratuur IF-signalen (I en Q) worden verkregen aan de uitgangen van de twee gebalanceerde fotodetectors. De DFS-waarde kan dan worden verkregen door de frequentie van het IF-signaal te meten en, nog belangrijker, de richting van de DFS kan worden geïdentificeerd door het faseverschil tussen de twee kwadratuuruitgangen te bepalen. Als I is vertraagd ten opzichte van Q, is de DFS positief. De figuren (i) en (ii) in Fig. 6(b) tonen de golfvormen van de I- en Q-signalen en het

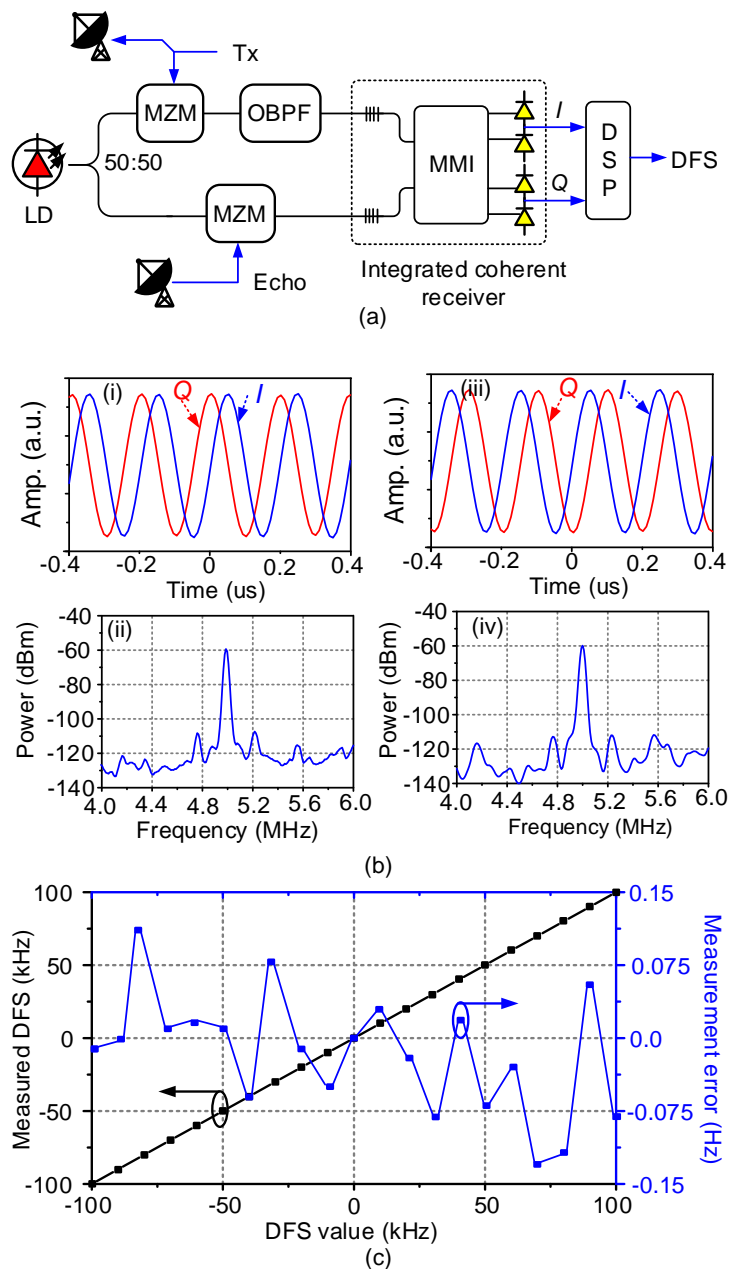


Fig. 6. Fotonisch DFS-meetsysteem op basis van de geïntegreerde coherente ontvanger. (a) Schematische weergave. (b) Elektrische golfvormen van de negatieve (i) en positieve (iii) 5 MHz DFS-signalen en (ii, iv) de overeenkomstige elektrische spectra. (c) Gemeten DFS en de meetfout.

elektrische spectrum van het IF-signaal. Zoals te zien, is de DFS-waarde 5

MHz en is de richting negatief. De figuren (iii) en (iv) in Fig. 6(b) geven de golfvormen en het spectrum weer bij een positieve DFS. Fig. 6(c) geeft de gemeten DFS en de bijbehorende meetfout weer. De meetfout, bekomen door de meetwaarden te vergelijken met de theoretische, is minder dan $\pm 0,15$ Hz.

Als besluit kunnen we stellen dat we geloven dat fotonische geïntegreerde schakelingen een steeds belangrijkere rol zullen spelen in toekomstige microgolf fotonische systemen omdat ze de complexiteit en het vermogensverbruik ervan sterk kunnen verminderen. In dit werk richtten we ons op RoF-systemen en fotonische DFS-meetsystemen, mogelijk gemaakt door het combineren van bestaande fotonische bouwstenen uit het silicium fotonica platform, zoals een siliciumringmodulator en een coherente 4-poorts MMI-gebaseerde ontvanger. Een silicium ringmodulator werd gebruikt om een full-duplex RoF systeem met lokale SSB-modulatie en hergebruik op afstand van de carrier te realiseren. Door deze component verder te combineren met een O-band III-V fotodetector, geïntegreerd gebruikmakend van transferprinting, kon een volledige III-V-op-silicium transceiver worden gedemonstreerd als basis van een bidirectioneel RoF-systeem met een C-band stroomafwaartse link en een O-band stroomopwaartse link. Ten slotte wordt ook een fotonisch DFS-meetsysteem met richtingidentificatie op basis van een coherente ontvanger aangetoond.

Chapter 1

Introduction

THIS thesis aims to realize microwave photonic systems based on silicon photonic building blocks. In this introductory chapter, the background and motivation of this thesis will be given, which includes the basic knowledge and the state-of-the-art of microwave photonics, silicon photonics, and integrated microwave photonics, respectively.

1.1 Microwave photonics

Microwave photonics (MWP) is an interdisciplinary field that mainly focuses on microwave signal generation, processing, transmission and control based on photonics technologies [1-4]. As compared with the conventional pure electronic technologies, MWP has several advantages, which are shown in Tab. 1.1. Firstly, since the carrier frequency of the MWP system is hundreds of THz, the operational bandwidth of the MWP system can be very high, typically tens of GHz or even terahertz. Limited by the electronic bottleneck, the bandwidth of conventional microwave systems is typically only a few GHz. Secondly, MWP systems can be connected by optical fiber, the best transmission medium in the world, with a transmission loss as low as 0.2 dB/km. Purely electronic systems on the other hand, are connected by coaxial cables, of which the transmission loss is much higher, typically larger than 600 dB/km. Thirdly, conventional microwave systems, based on metallic waveguides, usually have a serious electromagnetic interference (EMI) problem. In contrast, an MWP system is basically based on dielectric waveguides, which are immune to EMI. Since optical fiber is very light (<

Tab 1.1. Comparison between MWP system and conventional microwave system

	Microwave system	Microwave photonic system
Bandwidth	Several GHz	Tens of GHz or THz
Trans. Loss	>600 dB/km	0.2 dB/km
EMI	Serious	Immunity
Weight	Heavy	Light
Isolation	Low	High (>60 dB)

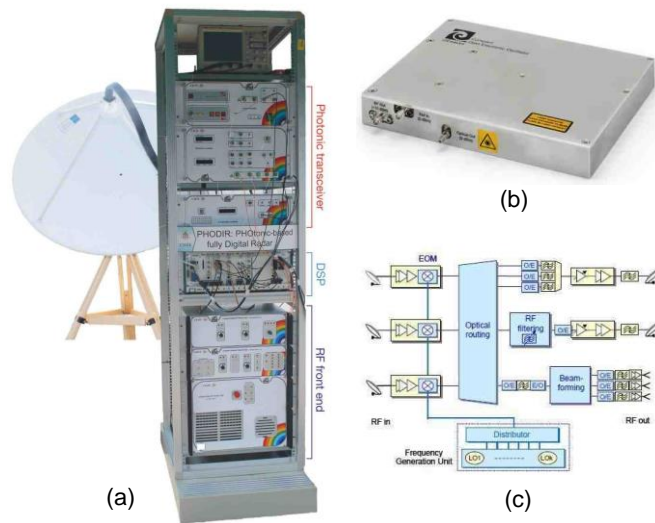


Fig. 1.1. Typical MWP systems. (a) Photonics-based coherent radar (figure from [5]), (b) optoelectronic oscillator (figure from [8]), and (c) photonic satellite payload (figure from [16]).

70g/km) and EMI shielding can be reduced, the weight of a MWP system is lower than that of a classical microwave system, which uses heavy cables (>200 kg/km) and requires strict EMI shielding. Finally, MWP systems also have better isolation (>60 dB) than microwave systems. Due to these distinct advantages, the domain of MWP has become the focus of intense research activities, and various exciting results have been presented in recent years, including a coherent photonics-based radar (Fig. 1.1(a)) [5, 6], photonic generation of low phase noise microwave signal (widely known as optoelectronic oscillator (OEO, Fig. 1.1(b)) [7, 8], reconfigurable microwave photonic filters (MPFs) [9, 10], analogy RoF communication systems [11, 12], photonics-based measurement systems [13, 14] and photonic communication satellite repeater (Fig. 1(c)) [15, 16]. However, most of the MWP systems are

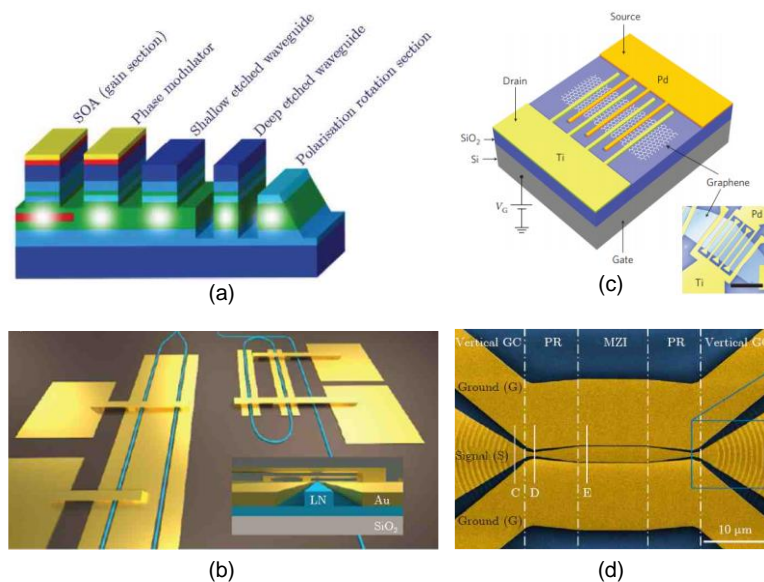


Fig. 1.2. Typical photonic integrated circuits based on different materials. (a) structure of InP-based circuits, (b) Si-LiNbO₃ hybrid electrooptic modulator (figure from [22]), (c) graphene photodetector (figure from [25]) and (d) plasmonic modulator (figure from [27]).

based on discrete electro-optic fiber-optic devices (e.g. stand-alone laser sources, electro-optic modulators and photodetectors (PDs)), which occupy a large size and lead to high system complexity and cost. This is the main reason that prevents MWP systems from being implemented in real life applications and replacing conventional electronic concepts. As a result, photonic integration is regarded as one of the most promising candidates to fill the gap between laboratory demonstrations and real world applications.

1.2 Photonic integrated circuit

Without doubt, photonics integration, which aims to realize all-optical or electro-optic functions on a chip scale, will significantly enhance the robustness of the system and reduce the size, weight, cost and power consumption as well. A wide range of materials can be used to realize

photonic integrated circuits (PICs). For instance, InP is widely used for the integration of both active devices (e.g., laser source [17], optical amplifier, electro-optic modulator [18] and photodetector) and passive devices (e.g., arrayed waveguide grating (AWG) [19], polarization converter [20] and ring resonator). However, as can be seen from the structure of typical InP-based devices shown in Fig. 1.2(a), many different regrowth processes have to be used, which makes the fabrication complicated and costly. Furthermore, passive InP waveguides usually have a larger loss and larger bend radii compared to silicon-based circuits as discussed below. Since LiNbO₃ has an ultra-strong electro-optic nonlinear effect, it is typically used to realize electro-optic modulators with low half-wave voltages [21]. However, these modulators usually have a large size (several centimetres) and are hard to integrate with other devices. To solve this problem, LiNbO₃ thin film was invented in recent years. Novel modulators based on LiNbO₃ film have been proposed [22], as shown in Fig. 1.2(b). More recently, by bonding a LiNbO₃ thin film to a SiO₂ layer, Si-LiNbO₃ modulators are also reported, which combine the advantages of high electro-optic nonlinearity of the LiNbO₃ thin film and low loss of silicon waveguides [23, 24]. Some new materials are also used to fabricate PICs, e.g. for ultra-fast graphene PDs (Fig. 1.2(c)) [25], polymer-based ultra-wideband modulators [26], plasmonic modulators (Fig. 1.2(d)) [27] and PZT-SiN modulators [28].

Compared with the aforementioned materials, silicon-based circuits (i.e., silicon photonics) attract significant interests from both academics and industrials, due to its compatibility with the mature fabrication technology of the CMOS industry [29, 30]. Making use of the strong optical confinement coming with the high index contrast between silicon ($n=3.45$) and SiO₂ ($n=1.45$) of the silicon-on-insulator (SOI) wafer, miniaturization, large volume and low-cost integration of photonic circuits becomes possible. The typical loss of a silicon waveguide is lower than 1 dB/cm and can be further reduced to be lower than 0.5 dB/cm if a rib waveguide is used [31]. Several passive components, such as high quality-factor (Q-factor) ring resonators (Fig. 1.3(a)) [32], polarization converters [33], on chip optical splitters [34] and high-resolution AWGs (Fig. 1.3(b)) [35], have been developed. Moreover, the SOI material can also be used to realize different types of active devices. For instance, electro-optic Mach-Zehnder modulators (MZMs) [36] or ring

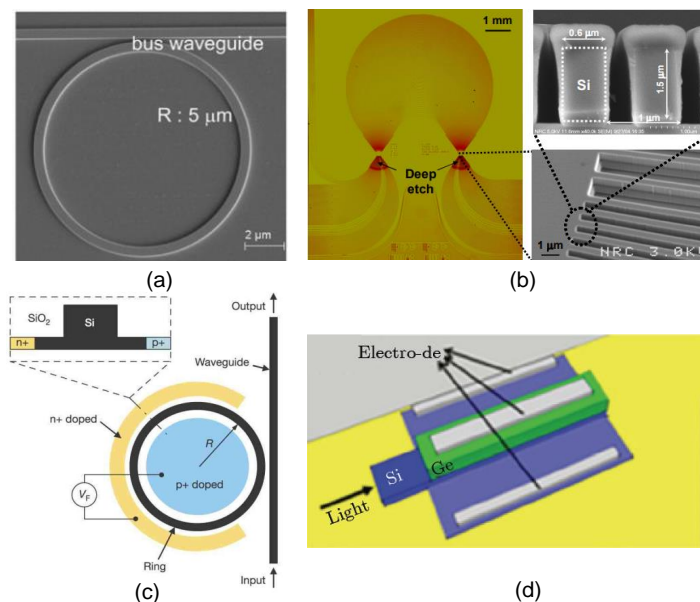


Fig. 1.3. Typical silicon-based integrated circuits. (a) ring resonator (figure from [32]), (b) arrayed waveguide grating (figure from [35]), (c) PN-doped ring modulator (figure from [37]) and (d) Si-Ge photodetector (figure from [38]).

modulators (Fig. 1.3(c)) [37] based on PN-doping, or high-speed PDs by co-integrating germanium with silicon [38] (Fig. 1.3(d)). It should be noted that, to reduce the cost, the most common and basic devices, such as MZMs, ring modulators, electro-absorption modulators (EAM), PDs, *etc.*, have already been integrated as basic building blocks in mature silicon photonic multi-project wafer (MPW) platforms, like imec iSiPP50G (Belgium) [39], AMF (Singapore) [40] and AIM Photonics (USA) [41].

1.3 Integrated microwave photonics

Obviously, when combining MWP technology and silicon photonics to realize integrated microwave photonics (IMWP), the cost-efficiency and scalability of MWP systems can be largely increased, which makes them more comparable to their electronic counterparts [42, 43]. Several advances have

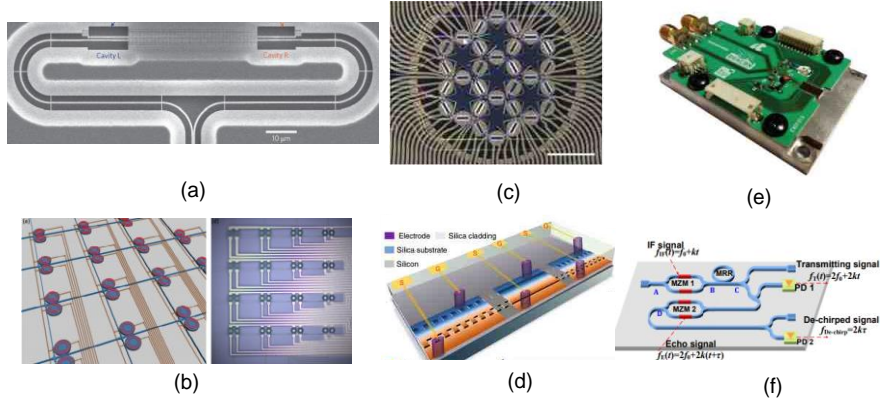


Fig. 1.4. Typical IMWP circuits based on silicon photonics. (a) microwave photonic filter based on silicon optomechanical structure (figure in [45]), (b) microdisk array (figure from [46]), (c) reconfigurable processor based on hexagonal mesh (figure from [47]), (d) programmable waveguide grating (figure from [48]), (e) photonic integrated chip bond-wired to a printed circuit board for satellite communication (figure from [49]), and (f) silicon-based microwave photonic radar circuit (figure from [50]).

been made. For example, using the stimulated Brillouin scattering (SBS) effect, an integrated MPF with 6 GHz tuning range, 98 MHz linewidth and 48 dB rejection was demonstrated. The SBS effect thereby was generated in a 1.25-cm-long partially suspended silicon nanowire [44]. In [45], as shown in Fig. 1.4(a), a silicon optomechanical structure was proposed to realize a microwave photonic bandpass filter with a central frequency of 6 GHz and an ultra-narrow bandwidth of 17 kHz. In addition, a lot of efforts are devoted to developing programmable microwave photonic processors, the equivalent of a Field Programmable Gate Array (FPGA) in the electrical domain. For instance, a photonic integrated processor based on a silicon microdisk array was reported, as shown in Fig. 1.4(b), which can realize reconfigurable optical filtering and optical true time delay [46]. Similarly, a two-dimensional silicon photonic waveguide hexagonal mesh, which consists of 30 independent MZI and 60 thermo-optic heaters, was fabricated in the SOI platform [47], as depicted in Fig. 1.4(c). Since the routing of the light can be dynamically changed, different structures can be implemented, enabling 21 different functionalities including a finite impulse response (FIR) MWP filter, an infinite impulse response (IIR) MWP filter, a ring cavity, complex coupled

resonator waveguides (CROW) and so on. More recently, a reconfigurable signal processor based on a programmable Bragg grating was developed [48]. The reconfigurability was realized by adjusting the carrier-based phase shifters in a silicon waveguide grating (Fig. 1.4 (d)). In addition to the basic devices and modules, IMWP chips are also demonstrated for some specific applications. In [49], a silicon photonic integrated and packaged circuit was invented for the satellite communication applications, as illustrated in Fig. 1.4(e). In another example, to minimize the size of a conventional microwave photonic radar system, an integrated silicon radar system-on-chip was proposed (Fig. 1.4(f)) [50].

1.4 The work presented in this thesis

As compared with the specially-designed and -fabricated devices used in the conventional MWP systems [44-50], this thesis focuses on MWP systems enabled by standard silicon photonic building blocks. By exploring the feasibility of using these silicon building blocks in an MWP system, we aim to find a low-cost solution for some MWP applications. The work presented in this thesis can be divided into three parts:

Firstly, a silicon ring modulator is integrated and applied in a radio-over-fiber (RoF) communication system. Based on the fact that the modulation efficiency of the silicon ring modulator is sensitive to the wavelength of the optical carrier injected into it, a RoF system with local single sideband (SSB) modulation and remote carrier reuse is proposed. The principle and the experimental results are detailed in Chapter 2.

Then, an O-band III-V PD is co-integrated with the C-band silicon ring modulator by transfer printing to realize a wavelength-multiplexed III-V-on-silicon transceiver. A bidirectional (BiDi) RoF system was developed based on this transceiver, in which the C-band silicon ring modulator is used for the electro-optic modulation of the downstream link and the transfer-printed O-band III-V PD is used for the photodetection of the upstream link. The transfer printing technology and the proposed RoF system are presented in Chapter 3.

The third part is about a photonic microwave Doppler frequency shift (DFS) measurement system based on an integrated silicon coherent receiver. A silicon coherent receiver consisting of a 90-degree optical hybrid based on a 2×4 multi-mode interferometer (MMI) coupler and a pair of SiGe balanced PDs (BPDs) is proposed. By using the coherent receiver, a photonic DFS measurement system, which can obtain both the DFS value and DFS direction, is demonstrated and shown in Chapter 4.

Finally, in Chapter 5, a conclusion and future perspectives are given.

The chips employed in the proposed microwave photonic systems are designed by my colleague J. Zhang. More specifically, the silicon ring modulators and SiGe PDs are directly from the process design kit (PDK) of imec. The III-V O-band PD and MMI-based optical 90-degree hybrid is designed by J. Zhang, and the transfer printing is also implemented by J. Zhang. The main works and contributions of the candidate are: 1) Characterization of the chips, including measuring the static and dynamic responses of the ring modulators and PDs, simulating the mode distributions of the MMI-based 90-degree hybrid, calculating the phase error and its influence, and designing an experiment to measure the phase error of the MMI-based 90-degree optical hybrid. 2) Designing and carrying out the RoF and microwave DFS measurement systems, including building up the setups, collecting and analyzing the data, and discussing the results.

1.5 Publications

- [1] Z. Tang, J. Zhang, S. Pan, G. Roelkens, D. Van Thourhout, "ring-modulator-based RoF system with local SSB modulation and remote carrier reuse," *Electronics Letters*, vol. 55, no. 20, pp. 1101-1104, 2019.
- [2] Z. Tang, J. Zhang, S. Pan, G. Roelkens, D. Van Thourhout, "RoF System based on a III-V-on-Silicon Transceiver with a Transfer-Printed PD," *IEEE Photonics Technology Letters*, vol. 31, no. 13, pp.1045-1048, 2019.
- [3] Z. Tang, J. Zhang, S. Pan, G. Roelkens, D. Van Thourhout, "Full-Duplex Analog Radio-Over-Fiber System Based on An Integrated Transceiver with A Silicon Microring Modulator and A Transfer-Printed III-V

Photodetector," in *European Conference on Integrated Optics (ECIO 2019)*, Belgium, pp. T.B2.2, 2019.

- [4] Z. Tang, J. Zhang, Z. Q. He, S. Pan, G. Roelkens, D. Van Thourhout, "Photonic Doppler Frequency Shift Measurement Enabled by an Integrated Photonic Six-Port Receiver," *IEEE Transactions on Instrumentation and Measurement*, under preparation.

References

- [1] J. Capmany and D. Novak, "Microwave Photonics Combines Two Worlds," *Nature Photonics*, vol. 1, no. 6, p. 319, 2007.
- [2] J. Yao, "Microwave Photonics," *Journal of Lightwave Technology*, vol. 27, no. 3, pp. 314-335, 2009.
- [3] A. J. Seeds and K. J. Williams, "Microwave Photonics," *Journal of Lightwave Technology*, vol. 24, no. 12, pp. 4628-4641, 2006.
- [4] A. J. Seeds, "Microwave Photonics," *IEEE Transactions on Microwave Theory and Techniques*, vol. 50, no. 3, pp. 877-887, 2002.
- [5] P. Ghelfi et al., "A Fully Photonics-Based Coherent Radar System," *Nature*, vol. 507, no. 7492, p. 341, 2014.
- [6] F. Zhang et al., "Photonics-Based Broadband Radar for High-Resolution and Real-Time Inverse Synthetic Aperture Imaging," *Optics Express*, vol. 25, no. 14, pp. 16274-16281, 2017.
- [7] X. S. Yao and L. Maleki, "Optoelectronic Oscillator for Photonic Systems," *IEEE journal of Quantum Electronics*, vol. 32, no. 7, pp. 1141-1149, 1996.
- [8] L. Maleki, "Sources: The Optoelectronic Oscillator," *Nature Photonics*, vol. 5, no. 12, p. 728, 2011.
- [9] J. Capmany, B. Ortega, and D. Pastor, "A Tutorial on Microwave Photonic Filters," *Journal of Lightwave Technology*, vol. 24, no. 1, pp. 201-229, 2006.
- [10] V. Supradeepa et al., "Comb-Based Radiofrequency Photonic Filters with Rapid Tunability And High Selectivity," *Nature Photonics*, vol. 6, no. 3, p. 186, 2012.

- [11] C. Lim, Y. Tian, C. Ranaweera, T. A. Nirmalathas, E. Wong, and K. Lee, "Evolution of Radio-Over-Fiber Technology," *Journal of Lightwave Technology*, vol. 37, no. 6, pp. 1647-1656, 2019.
- [12] D. Wake, A. Nkansah, and N. J. Gomes, "Radio Over Fiber Link Design for Next Generation Wireless Systems," *Journal of Lightwave Technology*, vol. 28, no. 16, pp. 2456-2464, 2010.
- [13] S. Pan and J. Yao, "Photonics-based Broadband Microwave Measurement," *Journal of Lightwave Technology*, vol. 35, no. 16, pp. 3498-3513, 2016.
- [14] X. Zou, B. Lu, W. Pan, L. Yan, A. Stöhr, and J. Yao, "Photonics for Microwave Measurements," *Laser & Photonics Reviews*, vol. 10, no. 5, pp. 711-734, 2016.
- [15] S. Pan et al., "Satellite Payloads Pay Off," *IEEE Microwave Magazine*, vol. 16, no. 8, pp. 61-73, 2015.
- [16] M. Sotom, B. Benazet, A. Le Kernec, and M. Maignan, "Microwave Photonic Technologies for Flexible Satellite Telecom Payloads," in *Proceedings of the 35th European conference on optical communication*, 2009, pp. 1-4.
- [17] S. Andreou, K. A. Williams, and E. A. J. M. Bente, "An InP-Based DBR Laser with an Intra-Cavity Ring Resonator with 130 kHz Linewidth and 65 dB SMSR," in *2018 IEEE International Semiconductor Laser Conference (ISLC)*, pp. 1-2, 2018.
- [18] M. U. Sadiq et al., "Efficient Modelling Approach for an InP Based Mach-Zehnder Modulator," in *25th IET Irish Signals & Systems Conference 2014*, 2014.
- [19] M. Kohtoku, H. Sanjoh, S. Oku, Y. Kadota, Y. Yoshikuni, and Y. Shibata, "InP-based 64-Channel Arrayed Waveguide Grating with 50 GHz Channel Spacing and up to-20 dB Crosstalk," *Electronics Letters*, vol. 33, no. 21, pp. 1786-1787, 1997.
- [20] L. Augustin, R. Hanfoug, J. Van der Tol, W. De Laat, and M. Smit, "A Compact Integrated Polarization Splitter/Converter in InGaAsP-InP," *IEEE Photonics Technology Letters*, vol. 19, no. 17, pp. 1286-1288, 2007.
- [21] M. Howerton, R. Moeller, A. Greenblatt, and R. Krahenbuhl, "Fully Packaged, Broad-Band LiNbO₃ Modulator with Low Drive Voltage," *IEEE Photonics Technology Letters*, vol. 12, no. 7, pp. 792-794, 2000.

-
- [22] C. Wang, M. Zhang, B. Stern, M. Lipson, and M. Lončar, "Nanophotonic Lithium Niobate Electro-Optic Modulators," *Optics Express*, vol. 26, no. 2, pp. 1547-1555, 2018.
- [23] C. Wang, M. Zhang, X. Chen, M. Bertrand, A. Shams-Ansari, S. Chandrasekhar, P. Winzer, and M. Lončar, "Integrated Lithium Niobate Electro-Optic Modulators Operating at CMOS-Compatible Voltages," *Nature*, vol. 562, no. 7725, p. 101, 2018.
- [24] M. He et al., "High-Performance Hybrid Silicon and Lithium Niobate Mach-Zehnder Modulators for 100 Gbit s⁻¹ and Beyond," *Nature Photonics*, vol. 13, no. 5, pp. 359-364, 2019.
- [25] F. Xia, T. Mueller, Y.-m. Lin, A. Valdes-Garcia, and P. Avouris, "Ultrafast Graphene Photodetector," *Nature nanotechnology*, vol. 4, no. 12, p. 839, 2009.
- [26] M. Lee et al., "Broadband Modulation of Light by Using an Electro-Optic Polymer," *Science*, vol. 298, no. 5597, pp. 1401-1403, 2002.
- [27] S. Ummethala et al., "THz-to-optical Conversion in Wireless Communications Using an Ultra-Broadband Plasmonic Modulator," *Nature Photonics*, vol. 13, no. 8, pp. 519-524, 2019.
- [28] K. Alexander et al., "Nanophotonic Pockels Modulators on a Silicon Nitride Platform," *Nature Communications*, vol. 9, no. 1, p. 3444, 2018.
- [29] R. Soref, "The Past, Present, and Future of Silicon Photonics," *IEEE Journal of Selected Topics in Quantum Electronics*, vol. 12, no. 6, pp. 1678-1687, 2006.
- [30] B. Jalali and S. Fathpour, "Silicon Photonics," *Journal of Lightwave Technology*, vol. 24, no. 12, pp. 4600-4615, 2006.
- [31] P. Dong et al., "Low Loss Shallow-Ridge Silicon Waveguides," *Optics Express*, vol. 18, no. 14, pp. 14474-14479, 2010.
- [32] W. Bogaerts et al., "Silicon Microring Resonators," *Laser & Photonics Reviews*, vol. 6, no. 1, pp. 47-73, 2012.
- [33] H. Subbaraman et al., "Recent Advances in Silicon-Based Passive and Active Optical Interconnects," *Optics Express*, vol. 23, no. 3, pp. 2487-2511, 2015.
- [34] D. Dai and J. E. Bowers, "Novel concept for Ultracompact Polarization Splitter-Rotator Based on Silicon Nanowires," *Optics Express*, vol. 19, no. 11, pp. 10940-10949, 2011.

- [35] P. Cheben et al., "A High-Resolution Silicon-On-Insulator Arrayed Waveguide Grating Microspectrometer With Sub-Micrometer Aperture Waveguides," *Optics Express*, vol. 15, no. 5, pp. 2299-2306, 2007.
- [36] P. Dong, L. Chen, and Y.-k. Chen, "High-Speed Low-Voltage Single-Drive Push-Pull Silicon Mach-Zehnder Modulators," *Optics Express*, vol. 20, no. 6, pp. 6163-6169, 2012.
- [37] Q. Xu, B. Schmidt, S. Pradhan, and M. Lipson, "Micrometre-Scale Silicon Electro-Optic Modulator," *Nature*, vol. 435, no. 7040, p. 325, 2005.
- [38] T. Yin et al., "31GHz Ge nip waveguide Photodetectors on Silicon-on-Insulator Substrate," *Optics Express*, vol. 15, no. 21, pp. 13965-13971, 2007.
- [39] iSiPP50G MPW, online source, website: <http://europpractice-ic.com/mpw-prototyping/siphotonics/imec/>
- [40] AMF MPW, online source, website: <http://www.advmf.com/wp-content/uploads/2018/09/MPW-Brochure-2018.pdf>
- [41] AIM Photonics MPW, online source, website: <https://aimphotonics.academy/industry/mpw-runs>
- [42] D. Marpaung, C. Roeloffzen, R. Heideman, A. Leinse, S. Sales, and J. Capmany, "Integrated Microwave Photonics," *Laser & Photonics Reviews*, vol. 7, no. 4, pp. 506-538, 2013.
- [43] D. Marpaung, J. Yao, and J. Capmany, "Integrated Microwave Photonics," *Nature Photonics*, vol. 13, no. 2, pp. 80, 2019.
- [44] A. Casas-Bedoya, B. Morrison, M. Pagani, D. Marpaung, and B. J. Eggleton, "Tunable Narrowband Microwave Photonic Filter Created By Stimulated Brillouin Scattering From A Silicon Nanowire," *Optics Letters*, vol. 40, no. 17, pp. 4154-4157, 2015.
- [45] K. Fang, M. H. Matheny, X. Luan, and O. Painter, "Optical Transduction and Routing of Microwave Phonons in Cavity-Optomechanical Circuits," *Nature Photonics*, vol. 10, no. 7, pp. 489-496, 2016/07/01 2016.
- [46] W. Zhang and J. Yao, "Programmable On-Chip Photonic Signal Processor Based on a Microdisk Resonator Array," in *2018 International Topical Meeting on Microwave Photonics (MWP)*, pp. 1-4, 2018.
- [47] D. Pérez et al., "Multipurpose Silicon Photonics Signal Processor Core," *Nature Communications*, vol. 8, no. 1, pp. 636, 2017.

- [48] W. Zhang and J. Yao, "A Fully Reconfigurable Waveguide Bragg Grating for Programmable Photonic Signal Processing," *Nature Communications*, vol. 9, no. 1, p. 1396, 2018.
- [49] V. C. Duarte et al., "Modular Coherent Photonic-Aided Payload Receiver for Communications Satellites," *Nature Communications*, vol. 10, no. 1, pp. 1984, 2019.
- [50] S. M. L, Z. Cui et al., "Chip-Based Photonic Radar for High-Resolution Imaging," *arXiv preprint arXiv:1905.12802*, 2019.

Chapter 2

RoF system based on silicon ring modulator

IN this chapter, we present a radio-over-fiber system based on a silicon ring modulator. Since the ring modulator can only perform sufficient electro-optic modulation when the wavelength of the incoming optical carrier is around the resonant wavelength of the ring modulator, a dual-wavelength optical carrier, with one of the carriers aligned to the resonant wavelength, is employed in the central office and injected into the ring modulator to realize local single sideband modulation. In the remote site, to avoid the usage of an additional laser source in the remote radio head, the unmodulated optical carrier in the single-sideband-modulated downstream signal is filtered out and reused as the optical carrier for the upstream link. The material presented in this chapter has in part been published in [1].

2.1 Introduction

High-speed wireless communication is one of the most important foundations of our modern society. Both civilian and military applications rely highly on high-speed and high-quality wireless communications. According to the prediction of Cisco [2], globally mobile data traffic will grow 7-fold from 2017 to 2022 with a compound annual growth rate of 46%. The monthly data traffic will reach 396 Exabytes in 2022, up from 122 Exabytes in 2017, due to the increasing popularity of bandwidth-hungry services, such as high-definition (HD) video streaming, online games, virtual reality (VR) and augmented reality (AR), intelligent transportation, hospital communications and so on. Although the bandwidth of current wireless communications,

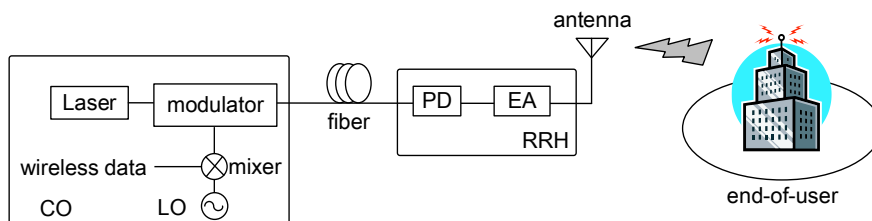


Fig. 2.1. Typical structure of a radio over fiber system.

taking the most advanced 5G technology as an example, has been significantly increased from several kHz to even 1 GHz, it is still insufficient for future services, which typically need several or even tens-of-GHz bandwidth.

An effective way to increase the data rate is to push the carrier to the higher frequency band, since the bandwidth in the lower frequency band is fully occupied. For example, China chooses the sub-6 GHz frequency band (i.e., 3.5, 2.6 and 4.9 GHz) [3] and the USA prefers the 28 GHz-band to build their 5 GHz networks [4], respectively. Besides, since there is plenty of unlicensed spectrum around the 60 GHz and THz frequency band, such as W-band (75-100 GHz) and D-band (110-170 GHz), a lot of groups are working on these frequency bands, and various key technologies and system demonstrations have been reported recently [5-10]. However, due to the high propagation loss in air, the coverage of high-frequency wireless services is usually limited and cannot meet the requirement for ubiquitous access of future communications. To solve this problem, the concept of RoF has been invented. RoF allows to transport millimetre wave signals over low loss optical fibers [11-14]. A typical RoF system structure is shown in Fig. 2.1. In the central office (CO), wireless data is upconverted to the desired frequency band by mixing with a local oscillator (LO) using an electrical- or photonics-based microwave frequency mixer. Then the upconverted RF signal is converted to the optical domain by sending it to an electro-optic modulator. The modulated optical signal is transmitted to a remote radio head (RRH) through a low-loss optical fiber link. In the RRH, the received optical signal is directly converted back to an electrical signal by a PD and emitted to free space after electrical amplification. As can be seen from Fig. 2.1, the RRH in the RoF system is simple, and only contains photodetection and the necessary

electrical amplification and antenna, while other complex and expensive devices and signal processing modules can be shifted to the CO. As a result, a unified platform that connects multiple RRHs is enabled, allowing centralized signal processing and dynamic resource allocation.

Since RoF technology combines the advantages of flexible connection (wireless technology) and large coverage (wired technology), numerous RoF systems focusing on different aspects were proposed in the literature. For example, photonics-based approaches are widely employed to generate high-quality and high-frequency LOs, since it is usually a big challenge for pure electronics to directly generate LO when the frequency is higher than 60 GHz. The most common and popular method is based on external modulation. By adjusting the bias voltage to make an MZM work at the carrier-suppressed double sideband (CS-DSB) modulation condition, the optical carrier can be suppressed, and frequency doubling can be achieved [15, 16]. Based on CS-DSB modulation, frequency-quadrupling [17, 18] or sextupling [19, 20] can also be realized. Another flexible mm-wave generation method is selecting two or more frequency modes from a mode-locked laser (MLL) [21] or a pulsed semiconductor laser [22]. With the generated optical LO, photonics-based up- and down-conversion become straightforward. In [23], multiband frequency upconversion is realized by using a polarization-multiplexed MZM, and a 60-GHz band RoF system is reported. Nonlinearities in an semiconductor optical amplifier (SOA), e. g., cross gain modulation (XGM) [24], cross phase modulation (XPM) [25], cross polarization modulation (XPolM) [26] and four-wave mixing (FWM) [27], can also be used to realize frequency up- or down-conversion for RoF communications. A comprehensive review on photonics-based microwave frequency mixing can be found in [28]. Because an RoF system is usually an analog system, it is easily influenced by the noise and nonlinearity of the link, especially when a high-order modulated signal (e.g., 1024 QAM) is transmitted. Main efforts are undertaken to increase the linearity of the analog photonic link [29]. For example, by placing a polarization modulator (PolM) in a Sagnac loop, a polarization-modulated signal and an unmodulated optical carrier is generated. When the two optical signals are combined at a polarizer, the 3-order intermodulation distortion (IMD3) terms will be cancelled, and then a high dynamic range analog photonic link for RoF communication was

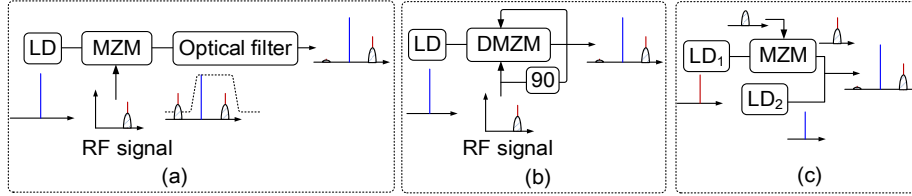


Fig. 2.2. Different SSB modulation methods. SSB modulation based on (a) filtering, (b) a pair of quadrature signals and (c) combining of modulated and unmodulated signals.

achieved [30]. Recently, an optical phase lock loop (OPLL) was designed to achieve a phase-modulated link with a spurious free dynamic range (SFDR) of $129 \text{ dBc}\cdot\text{Hz}^{2/3}$ [31]. Other techniques, such as multi-input multi-output (MIMO) [32, 33], power-over-fiber [34], mode-division-multiplexing [35], are deployed to realize high-capacity RoF communication systems as well.

Although RoF systems with different frequency bands, different data rates and different techniques were reported, the cost of RoF systems is still a very important issue that need to be taken into consideration especially when the number of connected devices is increased. To do so, several strategies can be utilized:

1) Optical SSB modulation: Fiber is regarded as the best medium for signal transmission. However, for a conventional DSB-modulated system, a fiber transmission link introduces significant fiber dispersion, with a transmission function shown as follows

$$H(\omega) = \cos\left(\frac{1}{2} D_{\omega} \omega_m^2\right) \quad (1)$$

where D_{ω} is the dispersion constant, which is determined by the fiber length and the optical carrier wavelength, and ω_m is the frequency of the transmitted RF signal. This *cos*-like transmission function causes frequency-dependent power fading. By using optical SSB modulation, power fading introduced by the fiber dispersion can be naturally compensated, which can reduce the signal processing cost related to the dispersion compensation in the receiver [36]. Fig. 2.2 illustrates three different kinds of SSB modulation approaches. In Fig. 2.2(a), an optical filter such as a fiber Bragg grating (FBG) [37] or a

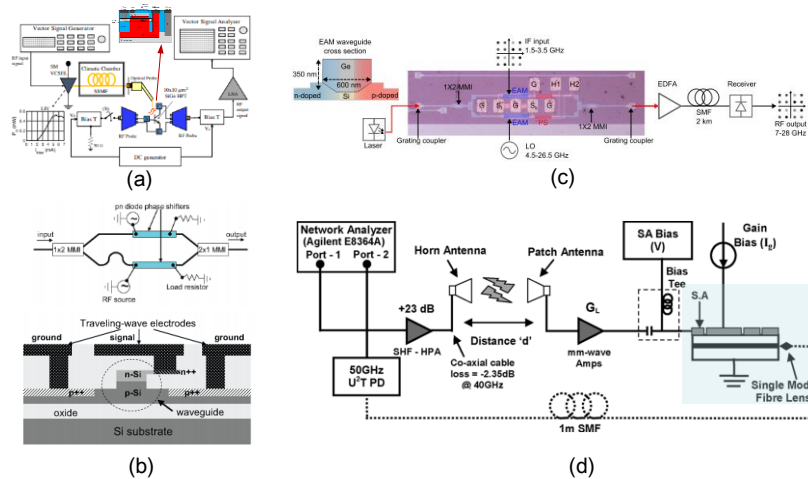


Fig. 2.3. RoF systems enabled integrated circuits. (a) SiGe photo-transistor (figure from [50]), (b) silicon modulator (figure from [51]), (c) EAM-based mixer (figure from [52]), (d) integrated MLL (figure from [53]).

diffraction grating [38] is used to directly remove one of the sidebands. The advantage of this method is its simple configuration, but the drawback is its low flexibility and its frequency dependence. Fig. 2.2 (b) shows another SSB modulation method, relying on introducing a pair of quadrature RF signals to a dual-drive MZM (DMZM) [39], dual parallel MZM (DPMZM) [40] or a pair of PolMs [41]. The main disadvantage of this scheme is that the sideband suppression ratio is dependent on the electrical 90-degree hybrid coupler, so wideband SSB modulation with high sideband suppression ratio is hard to achieve. The third approach is realized by combining a modulated signal with an unmodulated carrier [42, 43], which has the advantage of flexible operation and broad bandwidth. To ensure a high coherence between the two optical laser sources, a pair of coherent dual-wavelength laser sources is usually used.

2) Optical carrier reuse: For a full-duplex RoF communication system, an additional laser source is usually required in the RRH. By using optical carrier reuse, the extra light sources and their drivers can be removed, which not only reduces the complexity, but also reduce the power consumption of the RRH. Several wavelength reuse methods are reported. In [44], based on the signal erasing effect of a reflective SOA (RSOA), the carried downstream

data can be erased in the RRH and then the carrier can be reused for the upstream link. However, the bandwidth is usually lower than 10 GHz. Alternatively, an optical filter can be used in the RRH to select an unmodulated optical carrier for remodulation of the upstream data [45]. Another method is based on using different modulation schemes for the downstream and upstream links. For example, if phase modulation [46] or polarization modulation [47] is applied to the downstream link, amplitude modulation can be applied to the upstream link without affecting the downstream data. Furthermore, a polarization-multiplexed technique was reported to realize wavelength reuse as well [48].

3) Photonic integration: integrated, especially SOI-based, optical circuits will be the driving force to further lower the cost of the system [49]. Fig. 2.3 shows some RoF system examples enabled by photonic integrated circuits. A SiGe hetero-junction photo-transistor, as shown in Fig. 2.3(a), was used as a low cost photo-receiver for the detection of a 20 MHz LTE signal [50]. Besides, a linear silicon MZM was proposed for the RoF transmission of 802.11 OFDM signals [51], as shown in Fig. 2.3(b). In Fig. 2.3(c), a pair of broadband electro-optic modulators (EOMs) are integrated for frequency upconversion in the RoF system [52]. Fig. 2.4(d) presents an integrated MLL for LO-free RoF system [53], which enables 22-Mb/s binary phase shift keying data transmission at 40 GHz band.

2.2 Principle of silicon ring modulator

In this thesis, we propose a full-duplex RoF system with local SSB modulation and remote carrier reuse based on a silicon ring modulator. This proposed RoF concept presents three main advantages in response to the aforementioned three low-cost strategies:

1) An integrated silicon ring modulator is used for the electro-optic modulation, which is much more compact and potentially cheaper than the conventional modulators based on LiNbO₃ crystals.

2) since the electro-optic modulation efficiency is highly dependent on the optical carrier wavelength input to the ring modulator, optical SSB modulation can be easily realized by employing a dual-wavelength (dual- λ)

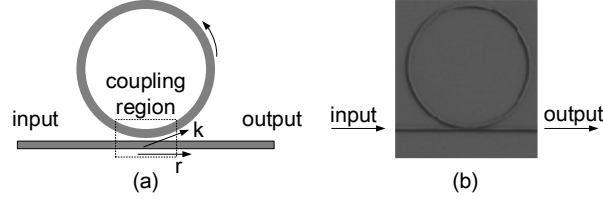


Fig. 2.4. All-pass silicon ring resonator. (a) structure and (b) picture.

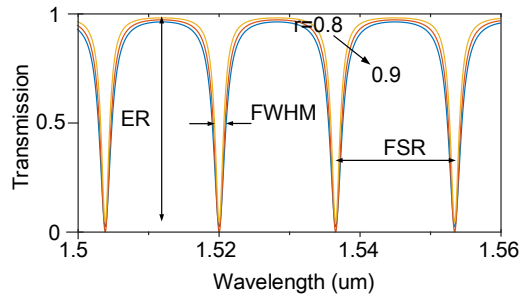


Fig. 2.5. Transmission response of an all-pass silicon ring resonator.

optical laser source, with one of the wavelengths aligned to the resonant wavelength of the ring modulator. This is much simpler than conventional methods, since a sophisticated transmitter based on sidebands separation, modulation, and recombination is no more required [42, 43].

3) since one of the optical carriers is unmodulated, it is selected in the RRH for reuse in the upstream link, which avoid the need of an additional laser source in the RRH. All these properties are realized by the silicon ring modulator, so the principle of the silicon ring modulator will be comprehensively introduced in this section.

The silicon ring modulator is based on a silicon ring resonator, one of the most fundamental building blocks in silicon photonics [54]. Fig. 2.4 shows the structure and picture of a silicon all-pass ring resonator, which consists of a straight bus waveguide and a ring waveguide. The relationship between the output and the incident optical fields can be expressed as [54]

$$\frac{E_{\text{Pass}}}{E_{\text{Input}}} = e^{j(\pi+\phi)} \frac{a - re^{-j\phi}}{1 - rae^{j\phi}} \quad (2)$$

$\phi=\beta L$ is the single-pass phase shift, which is determined by both the propagation constant β and the round-trip length L . The propagation constant β equals $2\pi n_{eff}/\lambda$, where n_{eff} is the effective index of the waveguide and λ is the wavelength of the input optical signal. $L=2\pi R$ and R is the radius of the ring waveguide. $a=\exp(-\alpha L)^{1/2}$ is the single-pass amplitude transmission, which relates to the attenuation coefficient α . r , as shown in Fig. 2.4(a), is the self-coupling coefficient. From (2), we can obtain the intensity transmission

$$T_n = \frac{I_{pass}}{I_{input}} = \frac{a^2 - 2ra \cos \phi + r^2}{1 - 2ra \cos \phi + (ra)^2} \quad (3)$$

Using (3), and $a=0.85$, $R=7.5 \mu\text{m}$, $n_{eff}=3$, the transmission of the all-pass ring resonator with different r values is calculated and presented in Fig. 2.5. The spectrum shows periodical notches, which means that most of the light will be cycled in the ring waveguide if the wavelength of the input optical signal equals to the notch wavelength shown. Some key parameters that determine the quality of the ring resonator can also be derived. For example, the full width at half maximum (FWHM) of the resonance spectrum is the width of the transmission notch when the transmission intensity is half of the maximum transmission intensity, which is given by

$$\text{FWHM} = \frac{(1-ra)\lambda_{res}^2}{\pi n_g L \sqrt{ra}} \quad (4)$$

The free spectral range (FSR) is the wavelength range between two adjacent notches, which is expressed as

$$\text{FSR} = \frac{\lambda^2}{n_g L} \quad (5)$$

and the extinction ratio is the ratio between the maximum and the minimum intensities, which can be written as

$$ER = \frac{T_t}{R_{\min}} = \frac{(r+a)^2}{(1+ra)^2} \bigg/ \frac{(r-a)^2}{(1-ra)^2} \quad (6)$$

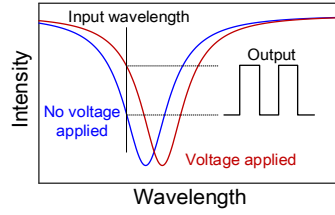


Fig. 2.6. Principle of silicon ring modulator.

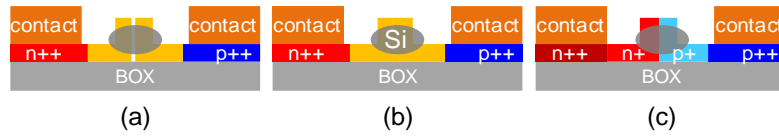


Fig. 2.7. Cross section of different silicon ring modulator structures based on different mechanisms for manipulation of the free carrier concentrations. (a) carrier accumulation, (b) carrier injection and (c) carrier depletion.

where n_g is the group index and λ_{RES} is the resonant wavelength.

As can be seen from Fig. 2.5, when $r=a$ (critical coupling condition), the highest extinct ratio can be obtained, as compared with the $r < a$ (overcoupling) and $r > a$ (undercoupling) conditions. As a result, to ensure a high extinction ratio for a ring modulator, the ring resonator is usually designed to work at the critical coupling state. Besides, since the output optical power is related to the wavelength of the input signal and the transmission response of the ring resonator, if the frequency response is shifted when an electrical voltage is applied (as shown in Fig. 2.6), the power of the output optical signal will be changed accordingly, thus, electro-optic modulation is realized. This is the most basic principle of the silicon ring modulator.

The wavelength shift can be introduced by modulating the refractive index of the waveguide. Since silicon does not exhibit any electro-optic (Pockels) effect, the plasma dispersion effect is the most used mechanism to realize this kind of refractive index modulation. The plasma dispersion effect manipulates the carrier density in the ring [55], and in turn changes the

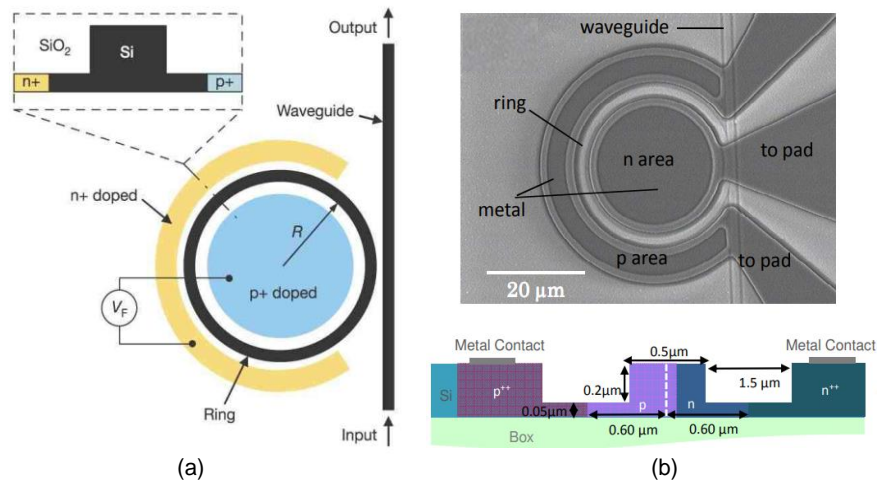


Fig. 2.8. Different silicon ring modulators. Silicon ring modulator based (a) forward-biased [57] and (b) inverse-biased PIN junction [58].

refractive index (and the absorption) of the silicon waveguide. As can be seen from Fig. 2.7, three basic structures can be used to realize carrier manipulation, which are carrier accumulation, carrier injection and carrier depletion, respectively. For a silicon ring modulator based on carrier accumulation [56], an oxide slot is usually inserted in the middle of the silicon waveguide, forming a capacitor structure where free carriers can accumulate. Due to the changing carrier density, the refractive index is modified, and modulation is realized due to the shift of the resonant wavelength. Based on carrier accumulation, the bandwidth and modulation efficiency can be high, but the extinction ratio is relatively low. The first silicon ring modulator based on carrier injection was reported in 2005 [57], as shown in Fig. 2.8(a). The ring waveguide is doped as a PIN junction, and then a forward-bias voltage is applied to the PIN junction. In this way, the majority of carriers will be forced to the core, and strongly influence the refractive index. Carrier injection-based ring modulators exhibit high extinction ratio, high modulation efficiency and low insertion loss. However, the bandwidth of this kind of ring modulator is usually low, due to the low recombination time of the carriers in the core (\sim ns). Finally, carrier depletion is the most widely employed mechanism for the fabrication of silicon ring modulators thanks to its high modulation bandwidth (40 GHz or higher) [58]. As can be seen from

Tab. 2.1 Comparison of silicon ring modulators and LiNbO₃ MZM

	Stru.	BW	ER	Mod. Eff.	IL	WL Sen.	Foot -print	COMS Comp.
Carrier accumulation	Si Ring	High (+)	Small (-)	High (+)	High (-)	High (-)	Small (+)	Y (+)
Carrier injection	Si Ring	Low (-)	Large (+)	Low (-)	Low (+)	High (-)	Small (+)	Y (+)
Carrier depletion	Si Ring	High (+)	Small (-)	High (+)	High (-)	High (-)	Small (+)	Y (+)
Pockels effect	LiNbO ₃ MZI	High (+)	Large (+)	Low (-)	High (-)	Low (+)	Large (-)	N (-)

(Stru. Structure; BW: bandwidth; ER: extinction ratio; Mod. Eff.: modulation efficiency; IL: insertion loss; WL Sen.: wavelength sensitivity; COMS Comp. COMS compatibility.)

Fig. 2.8(b), in this case the core is lightly doped to form a p-n diode. When the device is driven by a revised bias voltage, the carriers will be depleted, changing the refractive index. Table 2.1 shows the comparison of the different silicon ring modulators and the LiNbO₃ MZM. As can be seen, the silicon ring modulator is CMOS compatible and has a smaller footprint, higher modulator efficiency. Furthermore, this kind of silicon ring modulator can achieve ultra-high bandwidth since it is not limited by the recombination time. Therefore, it is the technique used to fabricate the silicon ring modulator presented in this thesis.

2.3 Full-duplex radio-over-fiber system with local single sideband modulation and remote carrier reuse

Fig. 2.9(a) shows a microscopic image of the integrated silicon ring modulator (together with two vertical grating couplers for coupling light to and from the chip). The radius of the ring resonator is about 7.5 μm and it was fabricated in imec's iSIPP25G platform. Fig. 2.9(b) shows the measured normalized static transmission response of the ring modulator. As can be seen, the ring modulator has resonances around 1542.16, 1554.96 and 1567.94 nm, respectively, with an FSR of about 12.8 nm and an extinction ratio of

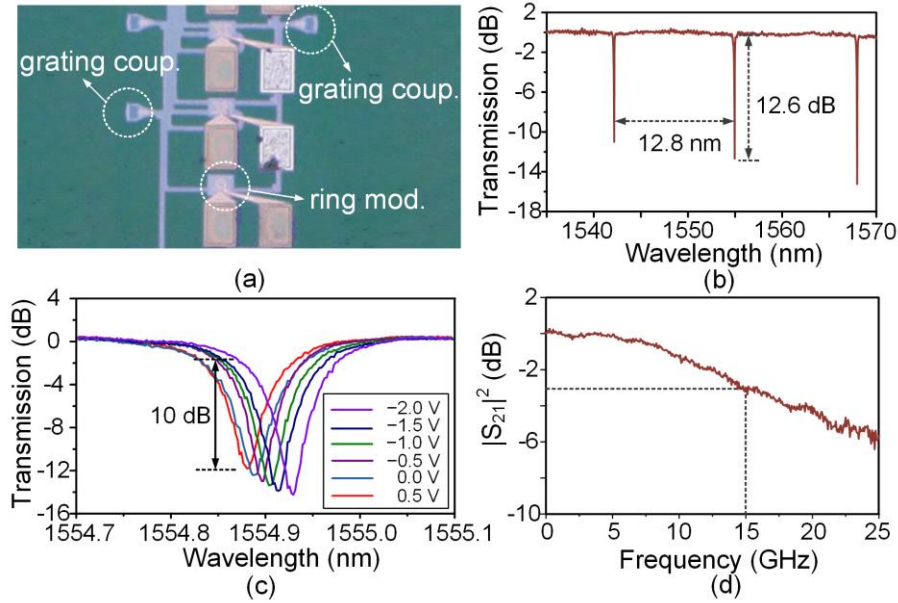


Fig. 2.9. Ring modulator and characterization. (a) Microscopic image of the ring modulator, (b) transmission response of the ring modulator, (c) resonant wavelength shift versus bias increasing from -2 to 0.5 V, and (d) normalized $|S_{21}|^2$ frequency response of the ring modulator.

about 12.6 dB (@ 1554.96 nm). To measure the DC properties of the modulator, the bias voltage applied to the ring modulator is changed from -2 to 0.5 V, and the measured result is shown in Fig. 2.9(c). The resonant wavelength shifts as the change of the bias voltage, and the extinction ratio is about 10 dB for a 2.5 Vpp voltage swing. Small signal characterization is also carried out by using an electrical vector network analyzer (EVNA, Agilent N5247A), with the result presented in Fig. 2.9(d). The electro-optic modulation bandwidth of the ring modulator, as can be seen, is 15 GHz at -1 V bias.

Based on the integrated silicon ring modulator, a full-duplex RoF system is proposed, as shown in Fig. 2.10. In the CO, a coherent dual- λ laser source is used. Here, in our experiment, a CS-DSB-modulated signal serves as the dual- λ laser source. To do so, a tunable optical carrier (Santec TSL-510) with a power of 10 dBm is firstly sent to a commercially-available 10 -GHz MZM. When a single-tone RF signal with a frequency of $f_b/2$ is applied to the MZM and the DC voltage is adjusted to bias the MZM at the null transmission point,

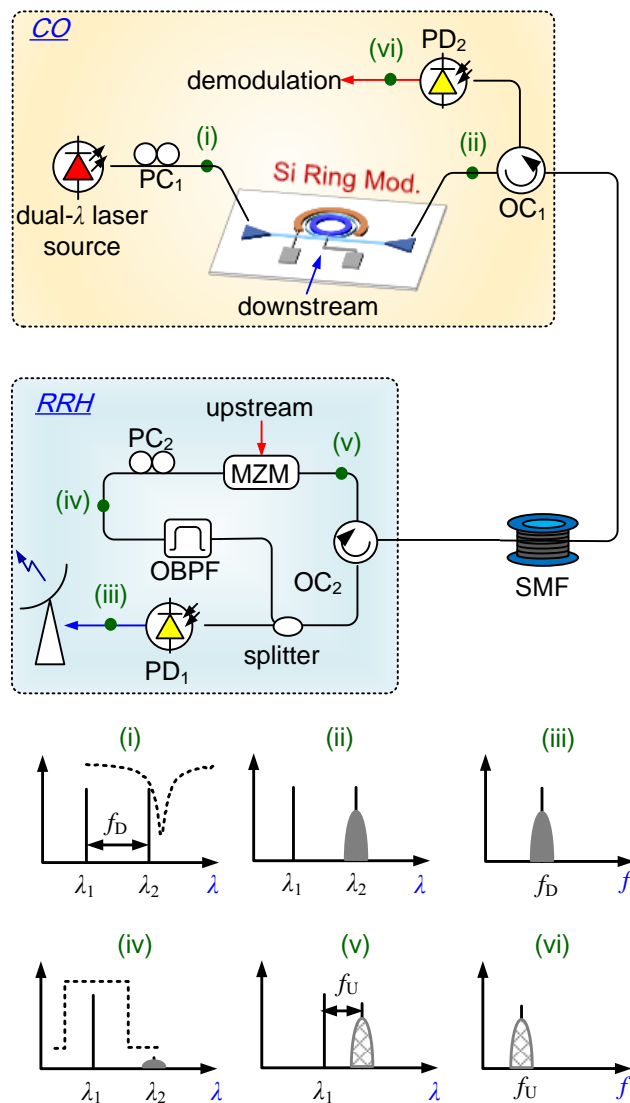


Fig. 2.10. Schematic diagram of the proposed full-duplex RoF system based on an integrated silicon ring modulator. (i) (vi): illustrations of the optical spectra at different points of the system.

a dual- λ laser source with a wavelength spacing of f_D is obtained, which is illustrated in Fig. 2.10(i). Then, the dual- λ laser source is sent to the ring modulator through a polarization controller (PC, PC_1). When properly setting the dual- λ laser source according to the response obtained in Fig. 2.9(d), one

of the carriers of the dual- λ laser source will align to the resonant wavelength of the ring modulator. Thus, only one of the optical carriers will be modulated by the intermediate frequency (IF) downstream data applied to the ring modulator, while the other one remains unmodulated. In this way an SSB-modulated optical downstream signal is generated, as shown in Fig. 2.10(ii). After passing through an optical circulator (OC, OC₁), the SSB-modulated optical downstream signal is transmitted to the RRH via a single-mode fiber (SMF).

In the RRH, the incoming optical downstream signal goes through another OC (OC₂) and is split into two portions. One portion is directly sent to a photodetector (PD, PD₁), from which an RF signal with a carrier frequency f_D is obtained, as can be seen from Fig. 2.10(iii). To realize the full-duplex communication, the unmodulated optical carrier in the other portion of the optical downstream signal is extracted by an optical bandpass filter (OBPF, Santec OTF350) and modulated by a 10-GHz MZM via a second PC (PC₂), shown as Fig. 2.10(iv). It should be noted that this MZM can also be replaced by a silicon ring modulator to reduce the cost of the RRH further. Fig. 2.10(v) shows the upstream signal after being modulated with the upstream data at a carrier frequency of f_U . The optical upstream signal is transmitted back to the CO, after passing through OC₂, SMF, and OC₁, respectively. In the CO, the optical upstream signal is detected by another PD (PD₂) resulting in the electrical upstream signal shown in Fig. 2.10(vi).

The downstream and upstream data are generated by a four-channel arbitrary waveform generator (Keysight M9052A). The electrical spectra are observed by an electrical spectrum analyzer (Agilent N9010A), and the data are demodulated by a real-time oscilloscope (Keysight DSA-Z 634A).

In our experiment, the wavelength spacing, i.e., f_D , of the dual- λ laser source is set to be 20 GHz. For the downstream link, a 1-GHz IF signal carrying 250-Mbaud 16QAM data (i.e., 1-Gb/s data rate) is applied to the ring modulator. Fig. 2.11(a) shows the electrical spectrum measured at the output of PD₁. As can be seen from the electrical spectrum, due to the frequency beating between the unmodulated and the modulated optical carriers of the dual- λ laser source, the 1-GHz IF signal is upconverted to the 21 GHz band.

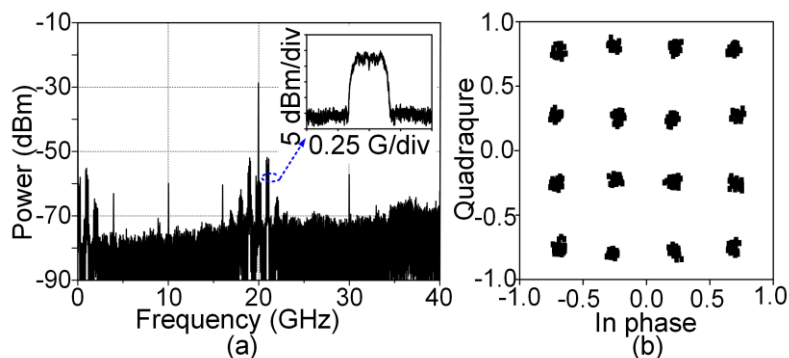


Fig. 2.11 Downstream RF signal obtained in the RRH. (a) Electrical spectrum and (b) the corresponding constellation diagram of the demodulated 16-QAM data. Inset in (a): zoom-in view of the electrical spectrum of the signal around 21 GHz.

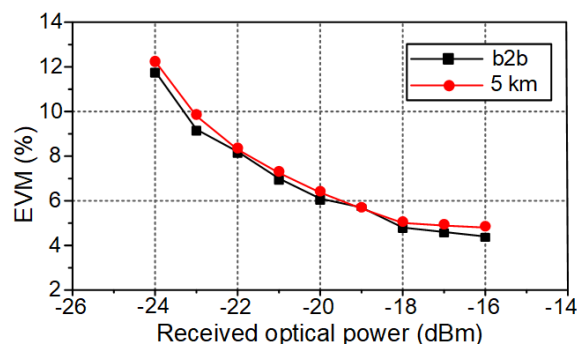


Fig. 2.12 Measured EVM versus received optical power for back-to-back (b2b) and 5-km downstream link.

The inset of Fig. 2.11(a) shows a zoom-in of the spectrum. The corresponding constellation diagram of the demodulated 16QAM data is shown in Fig. 2.11(b), and the measured error vector magnitude (EVM) evaluated by 1000 symbols is 4.3%. Fig. 2.12 shows the measured EVM versus the received optical power for the back-to-back (b2b) signal and for a 5-km downstream link. As can be seen, for a received optical power of -18 dBm, the EVM is lower than 5%. Furthermore, owing to the SSB modulation of the downstream link, the fiber transmission link introduces a negligible deterioration in the EVM. It should also be noted that, due to the limited

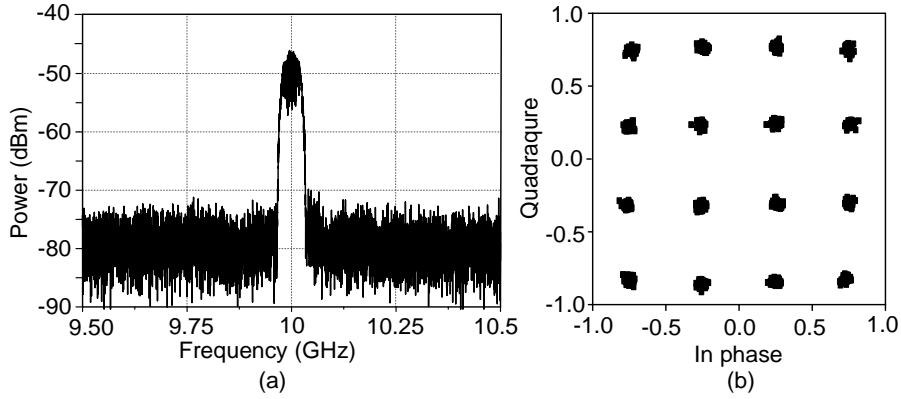


Fig. 2.13 Upstream RF signal obtained in the CO. (a) Electrical spectrum and (b) the corresponding constellation diagram of the demodulated 16-QAM data. Inset in (a): zoom-in view of the electrical spectrum of the signal around 10 GHz.

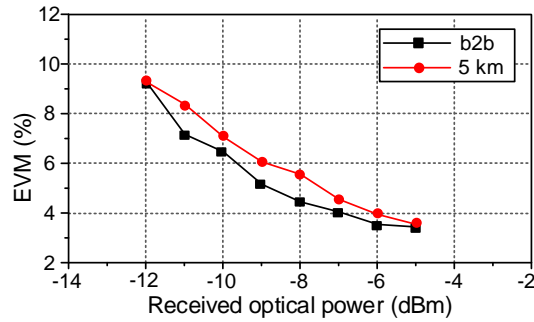


Fig. 2.14 Measured EVM versus received optical power for back-to-back (b2b) and 5-km upstream link.

facilities in our lab, the fiber length is restricted to be 5 km in our experiment. However, we believe that the fiber length can be further increased thanks to the SSB modulation.

For the upstream link, the unmodulated optical carrier in the optical downstream signal is selected by the OBPF in the RRH and modulated by a 10-GHz RF signal carrying 50-Mbaud 16QAM data. The electrical spectrum obtained at the output of PD₂ is shown in Fig. 2.13(a). Fig. 2.13(b) shows the corresponding constellation diagram with an EVM evaluated by 1000 symbols of 3.5%. Fig. 2.14 shows the measured relationship between the EVM and the received optical power for the upstream link. As can be seen, when

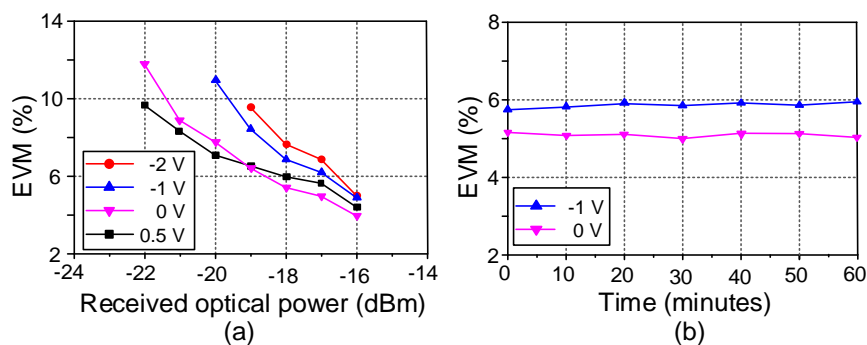


Fig. 2.15 Bias independence and stability. (a) Measured EVM versus the received optical power of the downstream link at different bias voltages of the ring modulator and (b) EVM variations of the downstream link in a period of one hour when the bias of the ring modulator is 0 and -1 V, respectively.

the received optical power is larger than -7 dBm, the EVM is lower than 5 %.

The modulation performance of the silicon ring modulator is related to the DC bias, so the sensitivity of the EVM to the bias voltage applied to the silicon ring modulator is investigated. The EVM versus the received optical power of the downstream link at different bias voltages is depicted in Fig. 2.15(a). As can be seen, the transmission performance is dependent on the bias voltages applied to the ring modulator, so bias control is necessary to reduce this influence. The stability of the proposed RoF system is also evaluated. It is well known that the response of the ring modulator is highly sensitive to temperature, so we only study the stability when the temperature is kept fixed (25 °C in our experiment, which is realized by a commercially-available temperature controller). Fig. 2.15 (b) shows the EVM variations of the downstream signal in the laboratory environment within one hour when the bias voltage is set as 0 and -1 V, respectively. Only very small changes can be observed, showing excellent stability of the proposed system. As can be seen from Fig. 2.11 and Fig. 2.14, the sensitivity of the downstream link is much better than that of the upstream link. This is because an optical amplifier is used in the downstream link before sending the downstream optical light to the PD and the received optical power in Fig. 2.12 is the optical power before

the optical amplifier.

It is worth noting that silicon MZM devices are also available, so the MZM used for the dual- λ laser source generation can be integrated with the ring modulator into a single chip to make the system cheaper and more compact. It should also be noted that many other schemes can be used to produce the dual- λ laser source, as mentioned in Section 2.1, such as a dual-mode optical laser, an integrated heterodyne distributed feedback (DFB) laser, or two optical tones selected from a frequency comb. By adjusting the spacing of the dual- λ laser source, the RF carrier can be easily increased to higher frequency band (e.g., 60 GHz or THz band). In addition, limited by the analysis bandwidth of the signal analyzer, 250-MBaud 16-QAM data is demonstrated in the proposed system. In addition, as the bandwidth of the currently used silicon ring modulator is 15 GHz but it is now possible to increase it to >40 GHz if imec's newest iSIPP50G platform is used, the data-rate of the downstream link can be significantly improved.

2.4 Conclusion

In this chapter, a full-duplex RoF system based on a silicon ring modulator is proposed. The principle of the silicon ring modulator, including the structure and the electro-optic modulation effect, is firstly introduced. Then, since the optical carrier can only be modulated when it is located at one of the slopes of the ring resonator resonance, a dual-wavelength optical carrier is used in the proposed RoF system to realize local SSB modulation to combat the power fading introduced by fiber dispersion. More importantly, since one of the optical carriers of the dual-wavelength optical carrier is unmodulated, it can be reused as the optical carrier for the upstream link in the RHH in order to avoid the need for an additional laser source. This approach was experimentally verified. The static and dynamic response of the silicon ring modulator was characterized, and a full-duplex RoF system for a 20-GHz band SSB-modulated downstream link and a 10-GHz upstream link were realized. An EVM < 5% for both the 21-GHz downstream and 10-GHz upstream links was achieved in a proof-of-concept experiment. In future work, we seek to enhance the linearity of the ring modulator and the

transmission performances in terms of data rate, transmission range and carrier frequency band of the RoF system.

Reference

- [1] Z. Tang, J. Zhang, S. Pan, G. Roelkens, D. Van Thourhout, "ring-modulator-based RoF system with local SSB modulation and remote carrier reuse," *Electronics Letters*, vol. 55, no. 20, pp. 1101-1104, 2019.
- [2] Cisco Inc., "Cisco Visual Networking Index: Forecast and Trends, 2017–2022 White Paper," Feb. 2019.
- [3] Qualcomm, "Spectrum For 4G and 5G," online source, website: <https://www.qualcomm.com/media/documents/files/spectrum-for-4g-and-5g.pdf>
- [4] D. Psychoudakis, H. Zhou, B. Biglarbegan, T. Henige, and F. Aryanfar, "Mobile Station Radio Frequency Unit for 5G Communications At 28GHz," in *2016 IEEE MTT-S International Microwave Symposium (IMS)*, pp. 1-3, 2016.
- [5] Y. Ghasempour, C. R. da Silva, C. Cordeiro, and E. W. Knightly, "IEEE 802.11 ay: Next-generation 60 GHz Communication for 100 Gb/s Wi-Fi," *IEEE Communications Magazine*, vol. 55, no. 12, pp. 186-192, 2017.
- [6] R. C. Daniels and R. W. Heath, "60 GHz Wireless Communications: Emerging Requirements and Design Recommendations," *IEEE Vehicular Technology Magazine*, vol. 2, no. 3, pp. 41-50, 2007.
- [7] P. Liu, M. Di Renzo, and A. Springer, "Line-of-Sight Spatial Modulation for Indoor mmWave Communication at 60 GHz," *IEEE Transactions on Wireless Communications*, vol. 15, no. 11, pp. 7373-7389, 2016.
- [8] M. K. Haider and E. W. Knightly, "Mobility Resilience and Overhead Constrained Adaptation in Directional 60 GHz WLANs: Protocol Design and System Implementation," in *Proceedings of the 17th ACM International Symposium on Mobile Ad Hoc Networking and Computing*, pp. 61-70, 2016.
- [9] T. Nagatsuma, G. Ducournau, and C. C. Renaud, "Advances in Terahertz Communications Accelerated by Photonics," *Nature Photonics*, vol. 10, no. 6, p. 371, 2016.
- [10] H. Elayan, O. Amin, R. M. Shubair, and M.-S. Alouini, "Terahertz Communication: The Opportunities of Wireless Technology Beyond 5G,"

- in *2018 International Conference on Advanced Communication Technologies and Networking (CommNet)*, pp. 1-5, 2018.
- [11] D. Wake, A. Nkansah, and N. J. Gomes, "Radio over Fiber Link Design for Next Generation Wireless Systems," *Journal of Lightwave Technology*, vol. 28, no. 16, pp. 2456-2464, 2010.
- [12] N. J. Gomes, M. Morant, A. Alphones, B. Cabon, J. E. Mitchell, C. Lethien, M. Csörnyei, A. Stöhr, and S. Iezekiel, "Radio-over-Fiber Transport for the Support of Wireless Broadband Services," *Journal of Optical Networking*, vol. 8, no. 2, pp. 156-178, 2009.
- [13] D. Novak, R. B. Waterhouse, A. Nirmalathas, C. Lim, P. A. Gamage, T. R. Clark, M. L. Dennis, and J. A. Nanzer, "Radio-over-Fiber Technologies for Emerging Wireless Systems," *IEEE Journal of Quantum Electronics*, vol. 52, no. 1, pp. 1-11, 2015.
- [14] C. Lim, Y. Tian, C. Ranaweera, T. A. Nirmalathas, E. Wong, and K.-L. Lee, "Evolution of Radio-over-Fiber Technology," *Journal of Lightwave Technology*, vol. 37, no. 6, pp. 1647-1656, 2019.
- [15] M. Weiß, M. Huchard, A. Stohr, B. Charbonnier, S. Fedderwitz, and D. S. Jager, "60-GHz Photonic Millimeter-Wave Link for Short- to Medium-Range Wireless Transmission Up to 12.5 Gb/s," *Journal of Lightwave Technology* vol. 26, no. 15, pp. 2424-2429, 2008.
- [16] J. O'reilly, P. Lane, R. Heidemann, and R. Hofstetter, "Optical Generation of Very Narrow Linewidth Millimetre Wave Signals," *Electronics Letters*, vol. 28, pp. 2309-2311, 1992.
- [17] J. Yu, Z. Jia, T. Wang, and G. K. Chang, "Centralized Lightwave Radio-Over-Fiber System with Photonic Frequency Quadrupling for High-Frequency Millimeter-Wave Generation," *IEEE Photonics Technology Letters*, vol. 19, no. 19, pp. 1499-1501, 2007.
- [18] H. Chi and J. Yao, "Frequency Quadrupling and Upconversion in a Radio Over Fiber Link," *Journal of Lightwave Technology*, vol. 26, no. 15, pp. 2706-2711, 2008.
- [19] P.-T. Shih, C.-T. Lin, W.-J. Jiang, H.-S. Huang, J. Chen, A. Ng'oma, M. Sauer, and S. Chi, "Transmission of 20-Gb/s OFDM Signals Occupying 7-GHz License-Free Band at 60 GHz Using a RoF System Employing Frequency Sextupling Optical Up-Conversion," *Optics Express*, vol. 18, no. 12, pp. 12748-12755, 2010.

-
- [20] S. Pan and J. Yao, "Tunable Subterahertz Wave Generation Based on Photonic Frequency Sextupling Using A Polarization Modulator and A Wavelength-Fixed Notch Filter," *IEEE Transactions on Microwave Theory and Techniques*, vol. 58, no. 7, pp. 1967-1975, 2010.
- [21] C. Lim, D. Novak, and G. Smith, "Implementation of an Upstream Path in A Millimeter-Wave Fiber-Wireless System," in *Proc. Int. Conf. Opt. Fiber Commun.*, pp. 16-17, 1998.
- [22] D. Novak, Z. Ahmed, R. B. Waterhouse, and R. S. Tucker, "Signal Generation Using Pulsed Semiconductor Lasers for Application In Millimeterwave Wireless Links," *IEEE Transaction on Microwave Theory and Techniques*, vol. 43, pp. 2257-2262, 1995.
- [23] Z. Z. Tang, F. Z. Zhang, and S. L. Pan, "60-GHz RoF System for Dispersion-Free Transmission of HD and Multi-Band 16QAM," *IEEE Photonics Technology Letters*, vol. 30, no. 14, pp. 1305-1308, 2018.
- [24] J. H. Seo, Y. K. Seo and W. Y. Choi, "1.244-Gb/s Data Distribution in 60-GHz Remote Optical Frequency Up-Conversion Systems," *IEEE Photonics Technology Letters*, vol. 18, no. 12, pp. 1389-1391, 2006.
- [25] H. J. Song, and J. I. Song, "Simultaneous All-Optical Frequency Downconversion Technique Utilizing an SOA-MZI for WDM Radio Over Fiber (RoF) Applications," *Journal of Lightwave Technology*, vol. 24, no. 8, pp. 3028-3034, 2006.
- [26] S. Fu, W. D. Zhong, P. Shum, Y. J. Wen and M. Tang, "Simultaneous Multichannel Photonic Up-Conversion Based on Nonlinear Polarization Rotation of an SOA for Radio-Over-Fiber Systems," *IEEE Photonics Technology Letters*, vol. 21, no. 9, pp. 563-565, 2009.
- [27] H. J. Kim and J. I. Song, "All-Optical Frequency Downconversion Technique Utilizing A Four-Wave Mixing Effect in a Single Semiconductor Optical Amplifier for Wavelength Division Multiplexing Radio-Over-Fiber Applications," *Optics Express*, vol. 20, no. 7, pp. 8047-8054, 2012.
- [28] Z. Z. Tang, Y. F. Li, J. P. Yao, and S. L. Pan, "Photonics-Based Microwave Frequency Mixing: Methodology and Applications," *Laser & Photonics Reviews*, accepted.
- [29] D. Marpaung, "High Dynamic Range Analog Photonic Links Design and Implementation," *PhD thesis*, University of Twente, 2009

- [30] N. Li and J. Yao, "High Dynamic Range and Wavelength-Reused Bidirectional Radio-Over-Fiber Link," *Optics Letters*, vol. 44, no. 6, pp. 1331-1334, 2019.
- [31] Y. Li, L. Xu, S. Jin, J. Rodriguez, T. Sun, and P. Herczfeld, "Wideband OPLL Photonic Integrated Circuit Enabling Ultrahigh Dynamic Range PM RF/Photonic Link," *Optica*, vol. 6, no. 8, pp. 1078-1083, 2019.
- [32] C. T. Lin, A. Ng'oma, W. Y. Lee, C. C. Wei, C. Y. Wang, T.-H. Lu, J. Chen, W.-J. Jiang, and C.-H. Ho, "2× 2 MIMO Radio-over-Fiber System at 60 GHz Employing Frequency Domain Equalization," *Optics Express*, vol. 20, no. 1, pp. 562-567, 2012.
- [33] J. Zhang, J. Yu, N. Chi, Z. Dong, X. Li, and G.-K. Chang, "Multichannel 120-Gb/s Data Transmission Over 2×MIMO Fiber-Wireless Link at W-Band," *IEEE Photonics Technology Letters*, vol. 25, no. 8, pp. 780-783, 2013.
- [34] D. Wake, A. Nkansah, N. J. Gomes, C. Lethien, C. Sion, and J.-P. Vilcot, "Optically Powered Remote Units for Radio-Over-Fiber Systems," *Journal of Lightwave Technology*, vol. 26, no. 15, pp. 2484-2491, 2008.
- [35] G. S. Gordon, M. J. Crisp, R. V. Pentty, T. D. Wilkinson, and I. H. White, "Feasibility Demonstration of A Mode-Division Multiplexed MIMO-Enabled Radio-over-Fiber Distributed Antenna System," *Journal of Lightwave Technology*, vol. 32, no. 20, pp. 3521-3528, 2014.
- [36] S. J. Savory, G. Gavioli, R. I. Killey, and P. Bayvel, "Electronic Compensation of Chromatic Dispersion Using a Digital Coherent Receiver," *Optics Express*, vol. 15, no. 5, pp. 2120-2126, 2007.
- [37] J. Capmany, B. Ortega, A. Martinez, D. Pastor, M. Popov, P. Fonjallaz, "Multiwavelength Single Sideband Modulation for WDM Radio-Over-Fiber Systems Using A Fiber Grating Array Tandem Device," *IEEE Photonics Technology Letters*, vol. 17, no. 2, pp. 471-473, 2005.
- [38] Z. Tang, S. Pan, and J. Yao, "A High Resolution Optical Vector Network Analyzer based on A Wideband and Wavelength-Tunable Optical Single-Sideband Modulator," *Optics Express*, vol. 20, no. 6, pp. 6555-6560, 2012.
- [39] G. H. Smith, D. Novak, and Z. Ahmed, "Technique for Optical SSB Generation to Overcome Dispersion Penalties in Fibre-Radio Systems," *Electronics Letters*, vol. 33, no. 1, pp. 74-75, 1997.

-
- [40] J. Sun, L. Yu, and Y. Zhong, "A Single Sideband Radio-over-Fiber System with Improved Dynamic Range Incorporating a Dual-Electrode Dual-Parallel Mach–Zehnder Modulator," *Optics Communications*, vol. 336, pp. 315-318, 2015.
- [41] Y. Zhang, F. Zhang, and S. Pan, "Optical Single Sideband Polarization Modulation for Radio-Over-Fiber System and Microwave Photonic Signal Processing," *Photonics Research*, vol. 2, no. 4, pp. B80-B85, 2014.
- [42] Y. Y. Won, H. S. Kim, Y. H. Son, et al., "Full Colorless WDM-Radio over Fiber Access Network Supporting Simultaneous Transmission of Millimeter-Wave Band and Baseband Gigabit Signals by Sideband Routing," *Journal of Lightwave Technology*, vol. 28, no. 16, pp. 2213–2218, 2010.
- [43] X. Li, J. J. Yu, Y. M. Xu et al., "60-Gbps W-band 64QAM RoF system with T-Spaced DD-LMS Equalization," in *Proc. Opt. Fiber Commun. Conf. Exhib. (OFC)*, pp. 1-3, Mar. 2017.
- [44] Y. Y. Won, H. C. Kwon, and S. K. Han, "1.25-Gb/s wavelength-division multiplexed single-wavelength colorless radio-on-fiber systems using reflective semiconductor optical amplifier," *Journal of Lightwave Technology*, vol. 25, no. 11, pp. 3472-3478, 2007.
- [45] Y.-T. Hsueh, M.-F. Huang, S.-H. Fan, and G.-K. Chang, "A novel Lightwave Centralized Bidirectional Hybrid Access Network: Seamless Integration of RoF with WDM-OFDM-PON," *IEEE Photonics Technology Letters*, vol. 23, no. 15, pp. 1085-1087, 2011.
- [46] H.-C. Ji, H. Kim, and Y. C. Chung, "Full-Duplex Radio-Over-Fiber System Using Phase-Modulated Downlink and Intensity-Modulated Uplink," *IEEE Photonics Technology Letters*, vol. 21, no.1, pp. 9-11, 2009.
- [47] T. Shao and J. P. Yao, "Wavelength Reuse in a Bidirectional UWB over Fiber System," *Optics Express*, vol. 21, no.10, pp. 11921-11927, May. 2013
- [48] Z. Tang and S. Pan, "A Full-Duplex Radio-over-Fiber Link based on A Dual-Polarization Mach–Zehnder Modulator," *IEEE Photonics Technology Letters*, vol. 28, no. 8, pp. 852-855, 2016.
- [49] K. Van Gasse et al., "Analog Radio-Over-Fiber Transceivers Based on III–V-on-Silicon Photonics," *IEEE Photonics Technology Letters*, vol. 30, no. 21, pp. 1818-1821, Nov. 2018.

- [50] J. Nanni, Z. G. Tegegne, C. Algani, G. Tartarini, and J. Polleux, "Use of SiGe Photo-Transistor in RoF Links based on VCSEL and Standard Single Mode Fiber for Low Cost LTE Applications," in *Proc. 2018 International Topical Meeting on Microwave Photonics (MWP)*, pp. 1-4, 2018.
- [51] F. Vacondio, M. Mirshafiei, J. Basak, A. Liu, L. Liao, M. Paniccia, and L. A. Rusch, "A Silicon Modulator Enabling RF Over Fiber for 802.11 OFDM Signals," *IEEE Journal of Selected Topics in Quantum Electronics*, vol. 16, no. 1, pp. 141-148, 2010.
- [52] K. Van Gasse, J. Verbist, H. Li, G. Torfs, J. Bauwelinck, and G. Roelkens, "Silicon Photonics Radio-over-Fiber Transmitter Using GeSi EAMs for Frequency Up-Conversion," *IEEE Photonics Technology Letters*, vol. 31, no. 2, pp. 181-184, Jan. 2019.
- [53] B. A. Khawaja, and M. J. Cryan, "Wireless Hybrid Mode Locked Lasers for Next Generation Radio-Over-Fiber Systems", vol. 28, no. 16, pp. 2268-2276, 2010.
- [54] W. Bogaerts, P. De Heyn, T. Van Vaerenbergh, K. De Vos, S. Kumar Selvaraja, T. Claes, P. Dumon, P. Bienstman, D. Van Thourhout, and R. Baets, "Silicon microring resonators," *Laser & Photonics Reviews*, vol. 6, no. 1, pp. 47-73, 2012.
- [55] G. T. Reed, G. Mashanovich, F. Y. Gardes, and D. Thomson, "Silicon Optical Modulators," *Nature Photonics*, vol. 4, no. 8, p. 518, 2010.
- [56] A. Abraham, O. Dubray, S. Olivier, D. Marrls-Morini, S. Menezo, and L. Vivien, "Low-Voltage And Low-Loss Silicon Modulator Based On Carrier Accumulation Using A Vertical Slot Waveguide," in *2015 IEEE 12th International Conference on Group IV Photonics (GFP)*, pp. 118-119, 2015.
- [57] Q. Xu, B. Schmidt, S. Pradhan, and M. Lipson, "Micrometre-Scale Silicon Electro-Optic Modulator," *Nature*, vol. 435, no. 7040, p. 325, 2005.
- [58] P. Dong et al., "Low V-pp, Ultralow-Energy, Compact, High-Speed Silicon Electro-Optic Modulator," *Optics Express*, vol. 17, no. 25, pp. 22484-22490, 2009.

Chapter 3

RoF system based on III-V-on-silicon transceiver

IN this chapter, we present a full-duplex radio-over-fiber system based on a III-V-on-silicon transceiver, which contains a C-band silicon ring modulator and an O-band III-V photodetector. The C-band silicon ring modulator is fabricated in the imec iSiPP25G platform, and is used for the modulation of the downstream signal. The O-band III-V photodetector is integrated on the chip by transfer printing and is employed for the detection of the upstream signal. Since the O-band photodetector is “transparent” for the C-band downstream signal, it can be placed directly on top of grating coupler without influencing the downstream link, and thereby a bidirectional wavelength-multiplexed radio-over-fiber system with a single fiber link is enabled. The state-of-the-art of III-V-on-silicon integration is briefly introduced and the basic principle of the transfer printing technology will be presented. The proposed radio-over-fiber system and the experimental results are also given. The material presented in this chapter has in part been published in [1, 2].

3.1 Introduction

As stated in Chapter 1, silicon is regarded as one of the most promising materials for the integration of optical devices, since it is compatible with the mature CMOS technology. However, since silicon is an indirect bandgap material, no laser source and optical amplifier can be directly integrated in silicon. In order to realize light generation and optical amplification, other materials, typically the III-V materials, should be used. Besides, some kinds

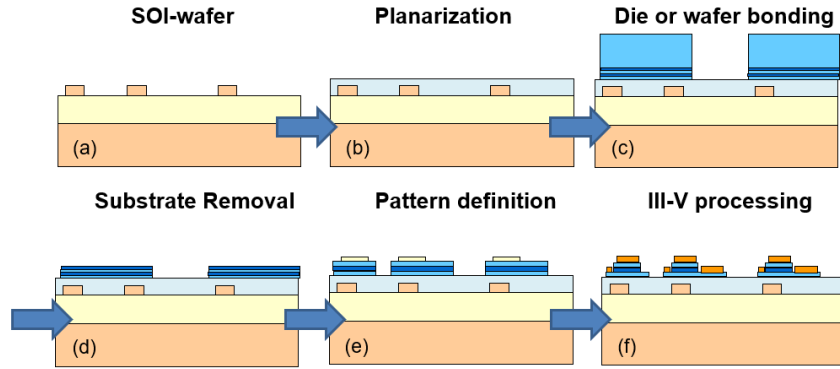


Fig. 3.1. Processing flow of wafer bonding.

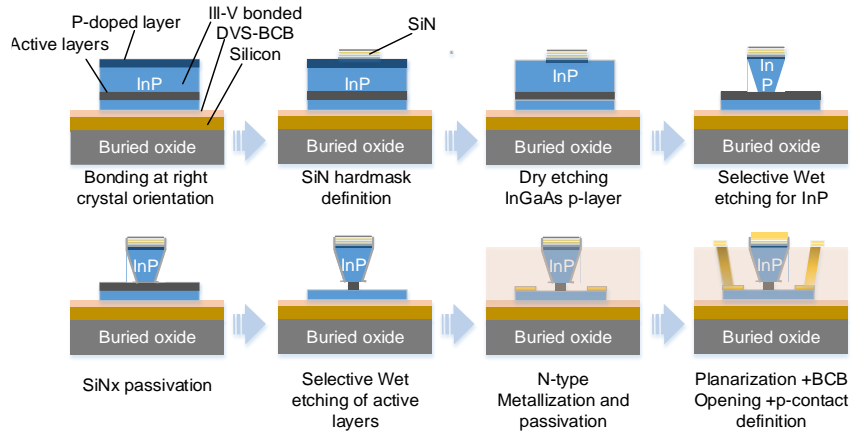


Fig. 3.2. Typical processing flow of III-V devices after wafer bonding.

of modulators and PDs can obtain much better performances when using III-V materials, although they can also be integrated by silicon photonics technology. Therefore, III-V-on-silicon integration [3-6] is of importance and attracts significant interests recently.

Three main techniques can be employed to realize III-V-on-silicon integration: wafer bonding, direct epitaxy and transfer printing. Wafer-bonding is at this moment the most mature technique. Fig. 3.1 shows the typical processing flow of wafer bonding. As can be seen, silicon structures, such as optical waveguides, optical filters, modulators and other passive/active elements, are pre-processed on a silicon wafer. Then the pre-

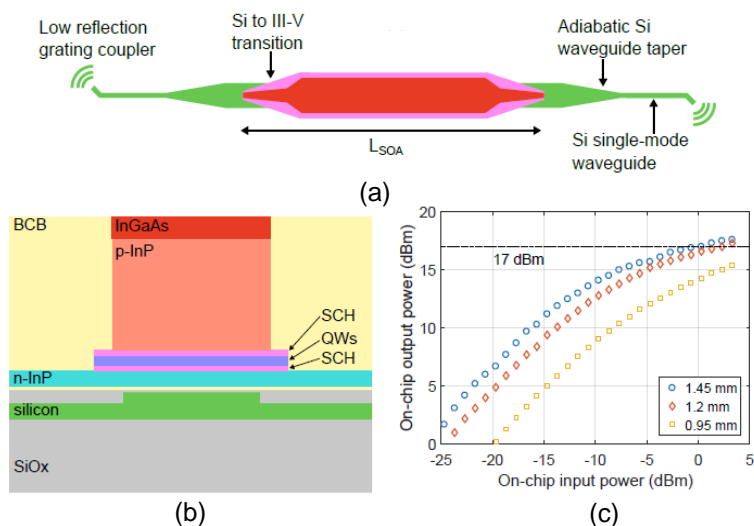


Fig. 3.3. Semiconductor optical amplifier based on wafer-bonding. (a) top view, (b) cross section and (c) gain measurement results (figure from [8]).

defined silicon photonic wafer is planarized by chemical mechanical polishing for the processing afterwards. III-V dies, which contain gain layers and a sacrificial etch “top” layer, are flipped with the optically active layers downwards. Then, the III-V dies are bonded on top of the silicon waveguides. For the fabrication of the III-V layer, the substrate of the III-V dies is removed. So far, a hybrid wafer consisting of silicon structures in the bottom and III-V layers on the top is obtained. In the next step, the pattern for the III-V elements are defined, and finally, III-V processing based on lithography process are followed to fabricate the desired III-V devices, which is shown in Fig. 3.2.

Various III-V-on-silicon integrated devices have been demonstrated by wafer-bonding. In [7], a SOA with an 18-dB small signal gain and 10-dBm saturate optical output power was proposed. Fig. 3.3 shows another III-V-on-silicon SOA [8]. A SOA with 1.45 mm long length was designed as shown in Fig. 3.3(a). The cross section of the layers is shown in Fig. 3.3(b). The measured unsaturated gain was 27 dB and the on-chip output power was 17.5 dBm, at a current density of 4.9 kA/cm² and a power consumption of 540 mW. When the III-V SOAs are combined with etched silicon gratings, III-V-on-silicon distributed feedback (DFB) or distributed Bragg reflector (DBR) lasers

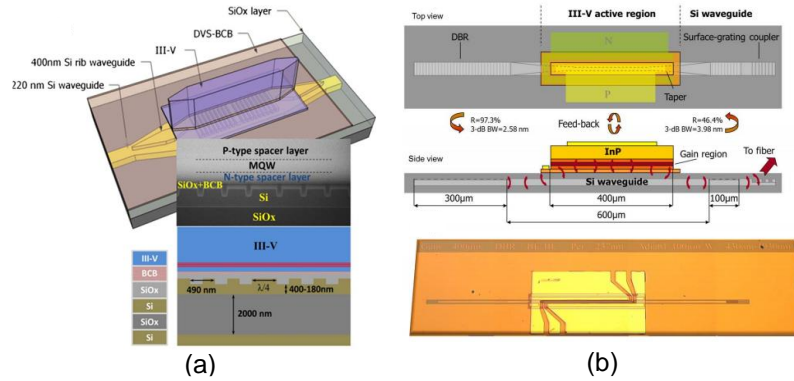


Fig. 3.4. III-V-on-silicon laser. (a) DFB laser [14], (b) DBR laser [15].

can be realized. For instance, as shown in Fig. 3.4 (a), a $1.55 \mu\text{m}$ III-V-on-silicon DFB laser with 14 mW output power and 50 dB sidemode suppression ratio was reported in [9]. In [10], a DBR single-mode laser with more than 50 dB sidemode suppression ratio and more than 7 GHz small signal modulation bandwidth was demonstrated. Besides, when deploying double ring resonators or AWGs for mode selection, a tunable or multi-wavelength laser can also be achieved. Other III-V-on-silicon wafer-bonded lasers were reported in [11-15].

Direct epitaxy, which grows III-V layers directly on silicon, is an alternative technology for III-V-on-silicon integration. Compared with wafer bonding, epitaxy is more compatible with the currently scalable and high-volume fabrication provided by CMOS foundries. The biggest challenge associated with direct epitaxy is the mismatch in lattice constant between silicon and the grown III-V layers. To reduce this effect, a thick buffer layer can be added, which, however, requires a long growth time and is not suitable for the fabrication of other devices [16]. By introducing quantum dot layers into buffer zone, the thickness of the buffer layer can be reduced [17, 18], but a quite complicate process should be used, which will significantly increase the cost. To overcome this problem, another approach is invented by imec, which is shown in Fig. 3.5 [19, 20]. Firstly, a ridged silicon wafer covered with a high-quality silicon oxide layer is defined (Fig. 3.5(a)). Then, chemical-based wet etching is employed to etch the ridged waveguide to create V-shaped grooves (Fig. 3.5(b)). In the next step, an InP layer is grown and completely

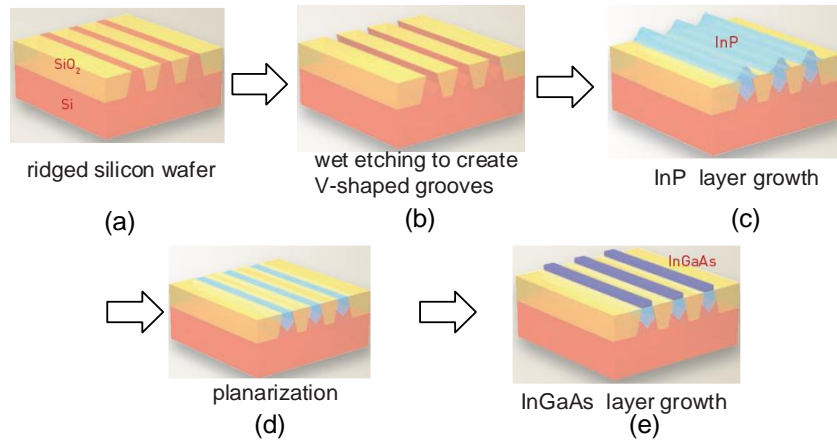


Fig. 3.5. Typical process for III-V-on-silicon integration by direct epitaxy.

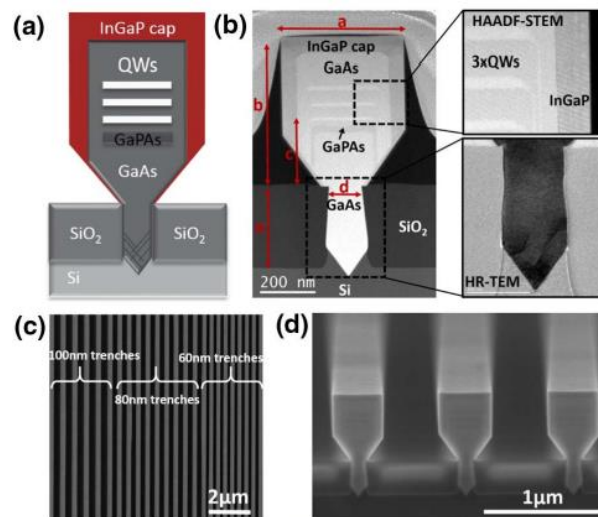


Fig. 3.6. An example of III-V-on-silicon laser based on direct epitaxy (figure from [21]). (a) layer stack, (b) STEM image, (c) top view and (d) zoom view of the nano-ridges.

fills in the grooved trenches, as shown in Fig. 3.5(c). The wafer is planarized by polishing in preparation for the further processing (Fig. 3.5(d)). Finally, an InGaAs layer is grown, presented in Fig. 3.5(e). The V-shaped grooves and the optimised nucleation process allow to confine all defects near the silicon-InP interface, with no defects found in the bulk of the material. Fig. 3.6 shows an example of a laser fabricated using this technique [21]. In this work,

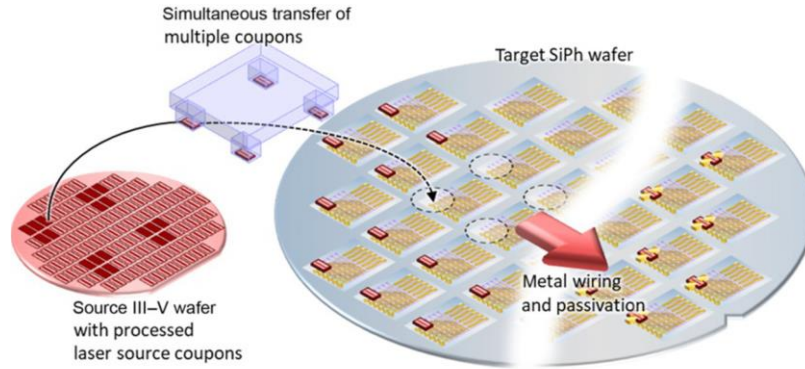


Fig. 3.7. Illustration of the transfer printing concept [35].

GaAs/InGaAs nano-ridge structures were used, and a single-mode laser with 37 mW threshold power and >28 dB sidemode suppression ratio was obtained. Other III-V-on-silicon devices based on direct epitaxy can be found in [22-25].

Transfer printing is a novel integration method, which was invented by Roger [26]. The concept for transfer printing is shown in Fig. 3.7 [27]. This technology involves the following main processes, which are the pre-fabrication of III-V coupons in a source III-V wafer, releasing the coupons from the source wafer, parallel transfer of these coupons to the target silicon wafer via an elastomeric stamp and removing the stamp for the later process (optional). Since transfer printing is the main technology we employed for the III-V-on-silicon transceiver fabrication, we will give a detailed introduction in the next section.

3.2 Transfer printing technology

Transfer printing, as can be seen from its name, is a technique that transfers one thing from one place to another thing at another place. In III-V-on-silicon integration, it is used to transfer a pre-designed III-V coupon, which is fabricated on a III-V source wafer, to a silicon photonic wafer.

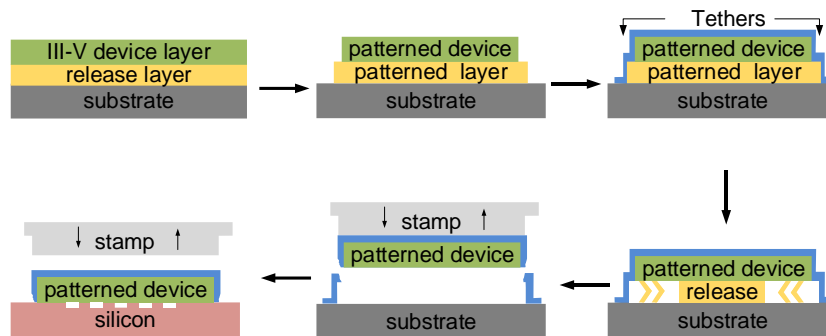


Fig. 3.8. Schematic flow of the transfer printing process.

Fig. 3.8 shows the typical process flow for transfer printing. In the first step, a III-V source wafer, with a release layer inserted between the substrate and the III-V device layer, is prepared. Then the layer is patterned to fabricate the III-V devices that need to be transfer printed to a silicon photonic wafer. A tether is covered onto the III-V device, which is used for the devices lifting afterwards. Before transfer printing, the release layer is released by under etching. A polydimethylsiloxane (PDMS) stamp is used to pick up the pre-fabricated III-V devices and finally, the III-V device is transfer-printed to a silicon photonic wafer to realize III-V-on-silicon integration.

Compared with the wafer-bonding and direct epitaxy approaches, transfer printing method has the following advantages [28]:

1) The expensive III-V materials can be effectively used in this technology, since the III-V coupons and the silicon photonic circuits can be independently fabricated. Besides, since space for full bond pads is not required to be on the device, the III-V coupons can be densely placed on the source wafer, which can reduce the fabrication cost as well.

2) Transfer printing technology is compatible for the source and target wafers. Although this thesis is mainly focused on III-V-on-silicon integration, multiple source materials, such as SiGe, graphene, colloidal quantum dot films, *etc.* can also be transfer printed to SOI or other target wafers. As a result, lasers, amplifiers, modulators, detectors, and electronic components can be transferred, which provides a lot of freedom to the customers.

3) Since the III-V coupons are fabricated independently, the process can be optimized and their quality can be evaluated before transfer printing, which

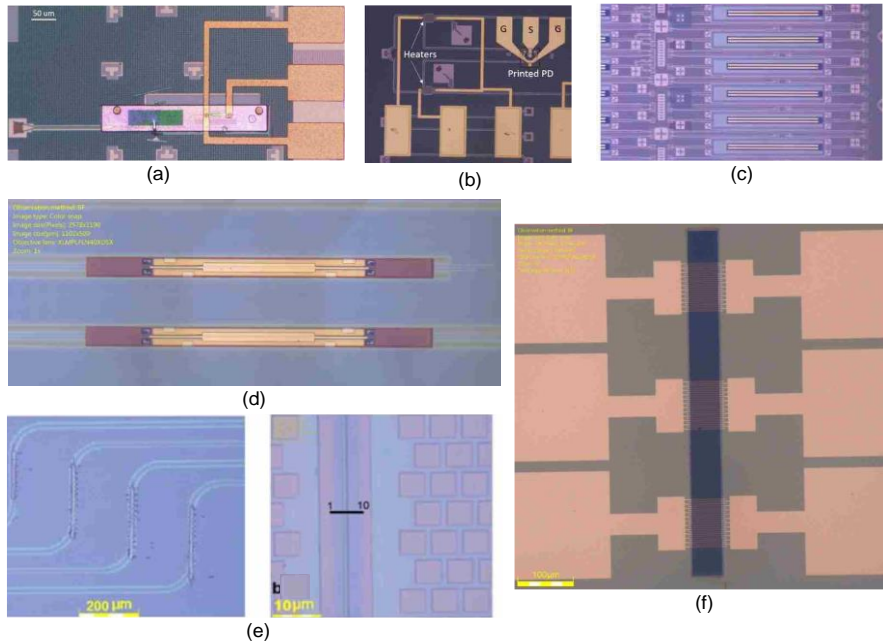


Fig. 3.9. Example of devices based on transfer printing. (a) Ge PD (figure from [29]), (b) InGaAs PD (figure from [30]), (c) FP laser (figure from [31]), (d) SOA (figure from [35]), (e) graphene (figure from [36]) and (f) colloidal quantum dot film (figure from [37]).

can ensure good performances of the circuits and improve the yield.

Thanks to these advantages, plenty of III-V-on-silicon devices are designed and achieved by transfer printing in the literature. Fig. 3.9 shows some examples. Fig. 3.9(a) shows the figure of a transfer printed Ge-on-silicon PD with a 3-dB bandwidth of 14 GHz, which supports 40 Gbps signal transmission [29]. Fig. 3.9 (b) depicts a III-V-on-silicon PD, in which four InGaAs PDs are transfer printed to a polarization-diversity receiver to realize parallel photodetection. The total data rate is 4×25 Gb/s [30]. In addition to PDs, lasers are also transfer printed. In Fig. 3.9(c), an InP-based etched facet Fabry-Perot laser is transfer printed to a silicon substrate, which enables effective heat sinking [31]. Other lasers, such as AlGaInAs/InP etched facet lasers [32], DFB lasers [33] and wideband light emitting diodes (LED) [34], have also been realized by transfer printing. Besides, in [35], transfer printing was employed to realize III-V-on-silicon SOAs with a gain of 17 dB, as shown

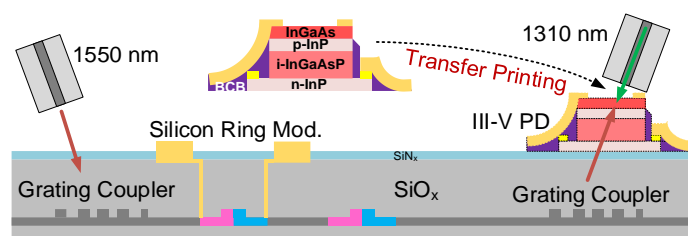


Fig. 3.10. Cross-section of the transfer-printed III-V-on-silicon transceiver.

in Fig. 3.9(d). Fig. 3.9(e) shows a transfer printed graphene circuit [36], in which a micron-size graphene film is transfer printed on Si_3N_4 waveguides. In Fig. 3.9(f), Al_2O_3 -capped short-wave-infrared PbS quantum dot photoconductor films were transfer printed to realize large-scale integrated PD arrays working at $2.1 \mu\text{m}$ wavelength with a responsivity of 25 A/W [37].

3.3 Full-duplex RoF system based on transfer-printed III-V-on-silicon transceiver

Based on transfer printing, a III-V-on-silicon transceiver was designed and fabricated by J. Zhang from our group [38]. The structure of the integrated transceiver is shown in Fig. 3.10. As can be seen from the cross section, the silicon part consists of two vertical grating couplers for coupling in and out of the light. The single-ended coupling loss is 4 dB, which can be further reduced to be lower than 1 dB with other designs [39]. A silicon C-band ring modulator is integrated between the two grating couplers to realize electrical-to-optical conversion. Although the ring modulator used in this Chapter also comes from the PDK of iSIPP25G, it will have slightly different responses due to the fabrication tolerance. As a result, the static and dynamic responses of the ring modulator are measured again. Firstly, the static transmission response of the ring modulator when the DC bias is 0 V is measured and presented in Fig. 3.11 (a). We used a tunable laser source (Santec TSL-510) and a high-sensitive optical power meter (Agilent 8613A). The resonant wavelengths of the ring modulator are 1539.24, 1552.04 and 1565.04 nm, so the FSR of the ring modulator is ~ 12.7 nm. The ring modulator used in this

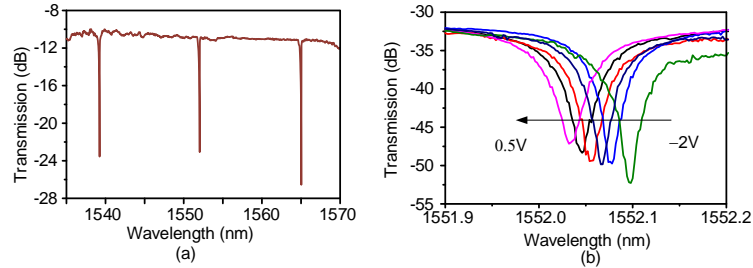


Fig. 3.11. Static characterization of the ring modulator. (a) transmission response of the ring modulator, (b) zoom-in profile around 1552 nm when the DC bias is increased from -2V to 0.5 V with a step of 0.5 V

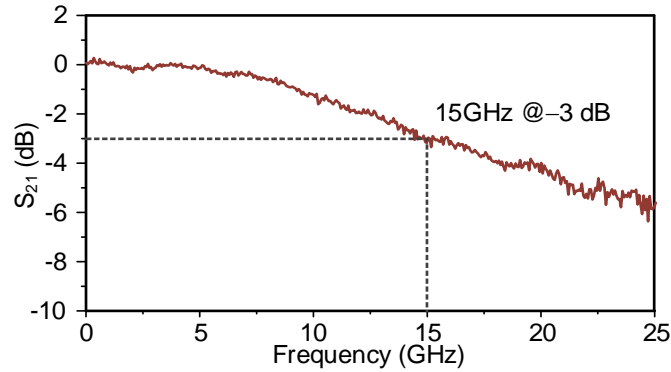


Fig. 3.12. Electro-optic modulation bandwidth of the ring modulator with -1 V DC bias.

chapter is identical with that in Chapter 2. Fig. 3.11 (b) shows the zoomed-in transmission response around 1552 nm when the DC bias voltage is adjusted from -2 V to 0.5 V with a step of 0.5 V. The resonant wavelength is shifted when the DC bias is changed, and the measured extinction ratio is 13 dB for a 2.5 Vpp voltage swing. In the next step, the dynamic characterization is carried out using a 67 GHz EVNA (Agilent N5247A). The measured electro-optic modulation response with -1 V DC bias is shown in Fig. 3.12 and shows a 3-dB bandwidth of 15 GHz.

In addition, an O-band III-V PD is transfer printed on top of one of the grating couplers, as shown in Fig. 3.10. Table 3.1 gives the layer stack of the O-band III-V PD fabricated on the source wafer. According to the introduction in Section 3.2, the PD is first fabricated on the source wafer. The

Table 3.1. Layer stack for the O-band III-V PD.

Layer	Material	Doping (cm ³)	Function	Thickness (nm)
10	InP	n.i.d	cap-layer	100
9	InGaAs	>1×10 ¹⁹	p-contact	100
8	InGaAs	1×10 ¹⁹	p-contact	200
7	InP	5×10 ¹⁷	p-cladding	300
6	InGaAsP	n.i.d	absorption	1000
5	InP	1×10 ¹⁸	n-contact	240
4	InP	n.i.d	etch stop	60
3	InGaAs	n.i.d	release	1000
2	InP	n.i.d	buffer	150
1	InP	n-type	substrate	

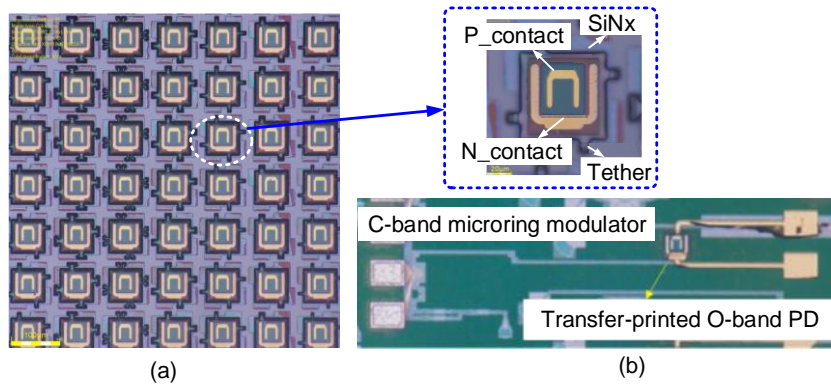


Fig. 3.13. III-V PD and transfer printed transceiver. Picture of (a) III-V PD with tether and (b) III-V-on-silicon transceiver.

detailed process flow for the fabrication of the O-band III-V PD can be found in [38] and the picture of the fabricated PDs is shown in Fig. 3.13(a). When the III-V PD is ready for transfer printing, the PD is encapsulated by a 2.5- μm thick photoresist layer with narrow tethers, as shown as the zoom-in inset in Fig. 3.13. Meanwhile, an aqueous FeCl_3 solution at 5 °C is employed to etch the release layer (1 μm thick InGaAs) to undercut the pre-fabricated PDs. Finally, a PDMS stamp is used to pick-up and print the III-V PD to the SOI wafer by an X-Celeprint $\mu\text{TP-100}$ tool. The picture of the III-V-on-silicon transceiver after transfer printing is shown in Fig. 3.13 (b).

The responsivity of the transfer printed III-V PD is first measured. The red line in Fig. 3.14(a) shows the responsivity for the O-band input optical signal

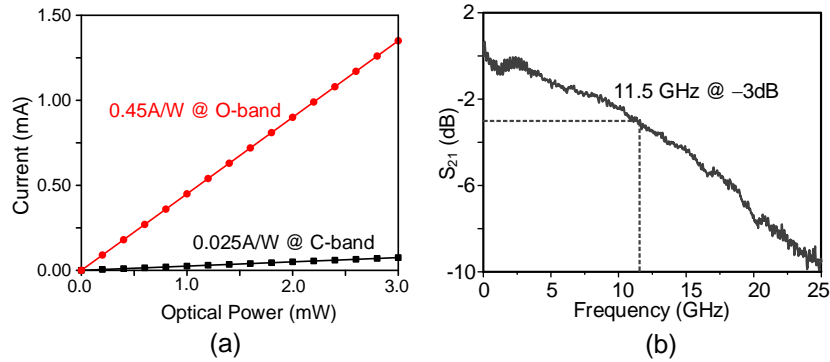


Fig. 3.14. Performances of the transfer printed III-V PD. (a) responsivities for C- and O-band input optical signals and (b) frequency response of the PD with -3 V bias.

when the DC bias applied to the PD is -3 V. As can be seen, a linear relationship between the photocurrent and the input optical power can be observed, with a responsivity of 0.45 A/W. As explained above PD is placed on top of the input grating coupler, which means that the C-band signal will also be applied to the PD. To avoid interference between the O-band and C-band signals, the PD is expected to have a low responsivity for the C-band input optical signal. The black line in Fig. 3.14(a) shows the measured responsivity of the O-band PD for the C-band input signal. The measured responsivity at C-band is only 0.025 A/W, which is 4-orders of magnitude lower. Thanks to the transparency of the PD to the C-band signal, it can be directly placed on top of the grating coupler, which can reduce the footprint and also enable bidirectional transmission of both C- and O-band signals in a single fiber without using optical circulators. The frequency response of the PD is also measured by an EVNA, with the results shown in Fig. 3.14(b). With a -3 V DC bias applied to the PD, the measured 3-dB bandwidth is 11.5 GHz.

Since the transceiver is composed of a C-band silicon ring modulator and an O-band III-V PD, a bidirectional wavelength-multiplexed full-duplex RoF is enabled, which is shown in Fig. 3.15. In the CO, a continuous wave (CW) light with a power of 12 -dBm is produced by a C-band tunable laser source (Santec TSL-510) and coupled into the C-band silicon ring modulator via a PC. According to the principle of the ring modulator in Chapter 2, the wavelength of the optical carrier is adjusted to be closed to one of the resonant

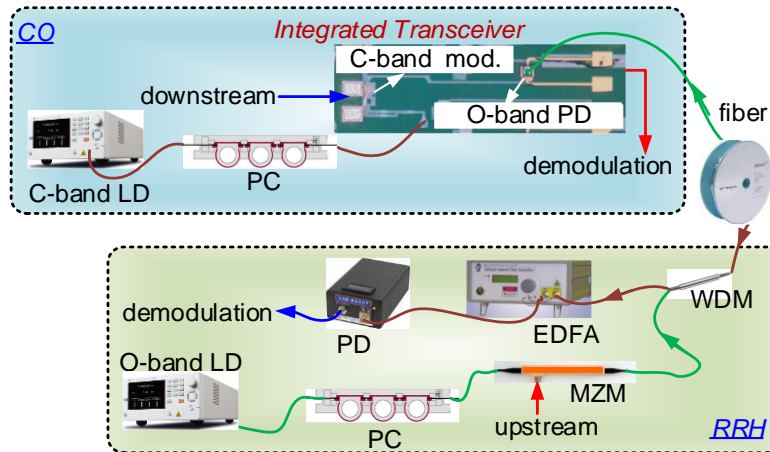


Fig. 3.15. Structure of the full-duplex RoF system based on the integrated III-V-on-silicon transceiver.

wavelengths of the ring modulation, i.e., 1552.128 nm in our experiment, to ensure sufficient electro-optic modulation efficiency.

For the downstream link, the RF signal applied to the silicon ring modulator is a 10-GHz RF signal carrying 50- and 250-Mbaud 16QAM data (i.e., 0.2 and 1 Gb/s), which is generated by an electrical arbitrary waveform generator (Keysight M9052A). To bias the ring modulator, a DC source (Keithley 2401) is used to produce a -0.7 V bias voltage and applied to ring modulator through a DC bias tee. The optical signal that carries the downstream data is then coupled out via another grating coupler and passed through the transfer-printed O-band PD on top of it. After a 5-km single-mode fiber link, the downstream optical signal is transmitted to a RRH. In the RRH, the downstream signal is boosted by an erbium-doped fiber amplifier (EDFA) to compensate the fiber transmission loss and the coupling loss and launched to a PD with a bandwidth of 20 GHz and a responsivity of ~ 0.7 A/W (Discovery Semiconductor Inc.). The electrical signal at the output of the PD is sent to an electrical spectrum analyzer with a bandwidth of 13.6 GHz to measure the electrical spectrum and a real-time oscilloscope (Keysight DSA-Z 634A) with a bandwidth of 63 GHz to observe the waveform and to realize QAM demodulation, respectively.

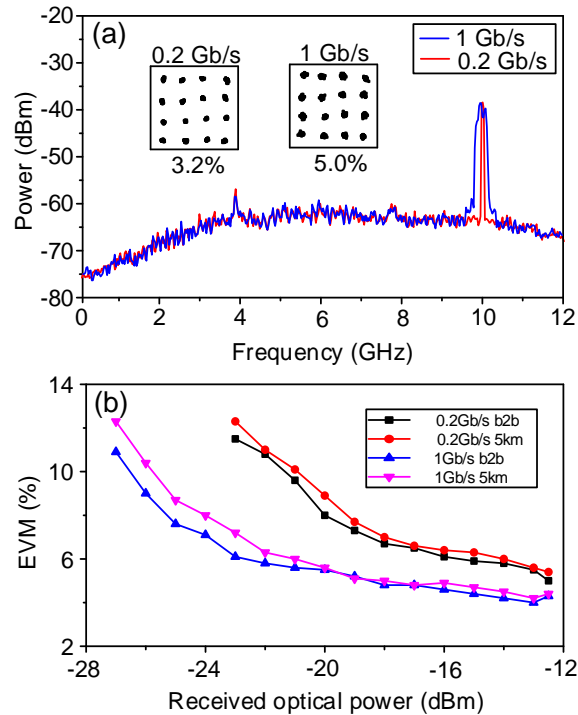


Fig. 3.16. Measured transmission performance of the downstream link. (a) Electrical spectra of the 0.2- and 1-Gb/s downstream signals and (b) EVM versus received optical power for back-to-back (b2b) and 5-km downstream link. Inset: Constellation diagrams of the demodulated 0.2- and 1-Gb/s 16QAM data.

For the upstream link, another CW light with a wavelength of 1356 nm and a power of 5-dBm is generated by an O-band tunable laser source (Santec TSL-510) and sent to a commercially-available O-band MZM via another PC. The upstream signal, 50- and 250-Mbaud 16QAM data with a carrier frequency of 8 GHz, is generated by another channel of the AWG. The modulated O-band upstream optical signal is duplexed with the C-band downstream signal by a wavelength division multiplexer and transmitted back to the CO through the same 5-km optical fiber without using optical circulators. In the CO, the upstream signal is converted to photocurrent by the transfer-printed O-band III-V PD. An RF GS probe and an electrical bias tee are used to apply DC bias to the PD and to guide the detected electrical signal from the chip to the electrical spectrum analyzer and another channel

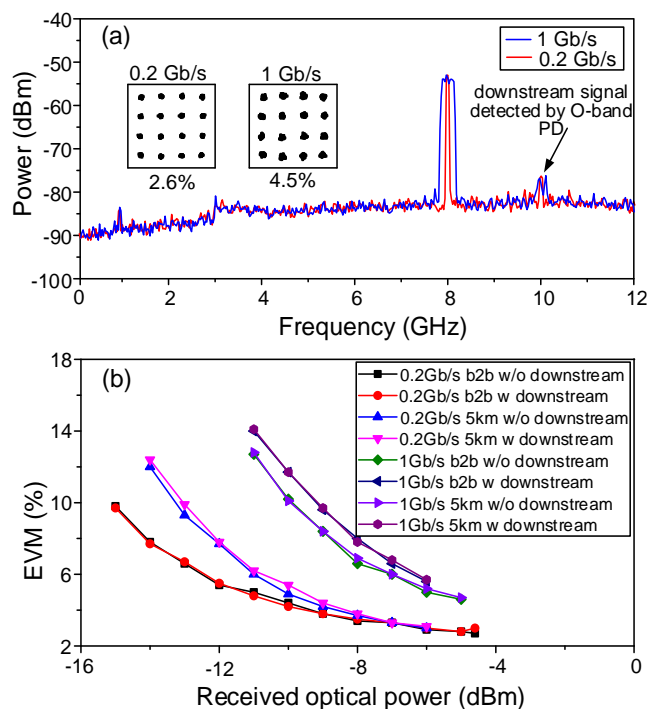


Fig. 3.17. Measured transmission performance of the upstream link. (a) Electrical spectra of the 0.2- and 1-Gb/s upstream signals and (b) EVM versus received optical power for b2b and 5-km upstream link with the downstream link switched on or off. Inset: Constellation diagrams of the demodulated 16QAM data.

of the real-time oscilloscope for the electrical spectrum measurement and QAM data demodulation, respectively.

Fig. 3.16(a) shows the measured electrical spectra of the 10-GHz band 0.2- and 1-Gb/s 16QAM downstream signals at the output of the PD in the RRH, when the optical power applied to the PD is about 0.5 dBm. The corresponding constellation diagrams are also shown as insets in Fig. 3.16(a), and have an EVM of 3.2 % and 5%, respectively. Fig. 3.16(b) shows the measured relationship between the EVM and the received optical power for the downstream link. As can be seen, when the received optical power is >-22 dBm, the EVM is $<6\%$, for the transmission of the 0.2-Gb/s 16QAM data. When the downstream signal is a 1-Gb/s 16QAM data, the EVM is $<6\%$ if the received optical power is >-15 dBm. In addition, the impact of the 5-km fiber

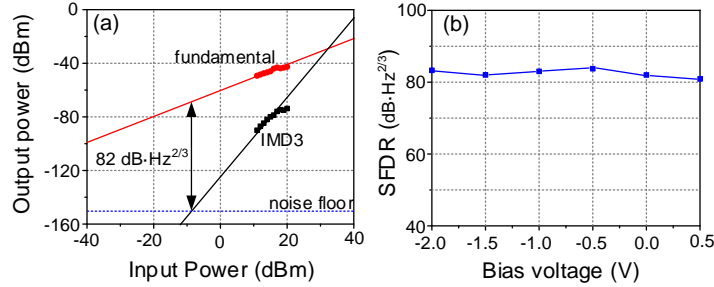


Fig. 3.18. Spurious free dynamic range (SFDR) of the RoF system. (a) SFDR of the 10-GHz downstream link when the bias voltage of the ring modulator is 1 V, and (b) the SFDR versus the bias voltages of the ring modulator.

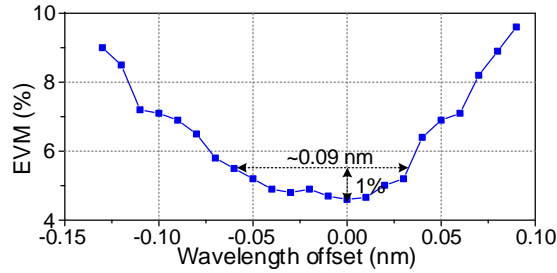


Fig. 3.19. Measured EVM versus the wavelength offset.

link on the downstream transmission is limited due to its low fiber transmission loss in the C-band and also the low fiber dispersion distortion for the X-band RF signal transmission.

Similarly, Fig. 3.17(a) shows the measured spectra of the 8-GHz band, 0.2- and 1-Gb/s 16QAM upstream signal, when -4.6 dBm optical power is applied to the transfer-printed O-band PD in the CO. The corresponding constellation diagrams, with EVMs of 2.6% and 4.5%, are presented as the insets. In Fig. 3.17(b), the measured EVM as a function of the received optical power for the upstream link is depicted. As can be seen, when the data-rate of the upstream signal is 0.2 Gb/s, the EVM, after 5-km fiber transmission, is lower than 6%, if the received optical power is higher than -11 dBm. When the data-rate of the upstream signal is increased to 1-Gb/s, an EVM of $<6\%$ is obtained when the received optical power is >-6 dBm. As compared with the back-to-back (b2b) transmission, the 5-km fiber transmission link introduces a slight deterioration in the EVM, which may result from the relatively higher fiber transmission loss in the O-band. Besides, to check the crosstalk between the

C-band downstream and O-band upstream signal in the O-band PD, the EVMs with and without downstream signal transmission are also compared and no obvious change is observed according to the results in Fig. 3.17(b).

As one of the most important parameters of the analog applications, the SFDR should be measured. Fig. 3.18(a) shows the SFDR of the 10-GHz downstream link when the bias voltage of the ring modulator is -1 V. With a measured noise floor of -150 dBm, the SFDR is about 82 dB·Hz^{2/3}. Fig. 3.18(b) presents the SFDR with different bias voltages of the ring modulator. The measured SFDR is within $81\sim 84$ dB·Hz^{2/3} when the bias voltage is tuning from 0.5 to -2 V. The SFDR of the ring-modulator-based system is relatively lower than that of the system based on LiNbO₃ MZM, which is typically larger than 100 dB·Hz^{2/3}. Therefore, in order to compete with the LiNbO₃-MZM based system, the SFDR of the silicon ring modulator should be improved. Some techniques can be used, such as a ring-loaded MZI [40]. Since the MZI has a sinusoidal response with a negative third-order derivative and the ring modulator has a positive third-order derivative, the entire third-order distortions can be eliminated when properly adjusting the coupling efficiency between the MZI and the ring modulator, which leads to an improvement of the SFDR. In addition, to investigate the transmission performance dependence on the wavelength of the optical carrier, EVM of the 0.2-Gb/s 16QAM data versus the optical carrier wavelength offset is measured and shown in Fig. 3.19. As can be seen, the EVM is increased by 1% when the wavelength drift is from -0.06 to 0.03 nm. As a result, to ensure the best transmission performance, feedback loop for the wavelength tracking and locking is desired [41].

Since the 3-dB bandwidths of the ring modulator and the transfer-printed PD are 15 and 11.5 GHz respectively, the proposed full-duplex RoF link is designed to work in the X-band. Again, if the ring modulator would be realized in imec's newest iSIPP50G platform and a modified design is employed for the PD, the bandwidth of the transceiver can be largely increased, enabling millimeter-wave RoF systems. Furthermore, transfer printing has the advantage of parallel device pick-up and print, so multichannel transceivers would be possible [47], which can further increase the capacity, if wavelength division multiplexing technology is also employed. The laser and PC are still off chip due to the lack of a laser source

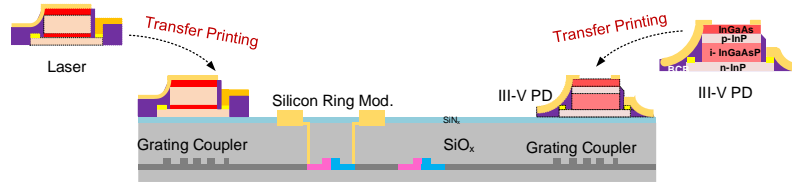


Fig. 3.20. Illustration of a full-integrated transceiver with transfer-printed LD and PD.

on silicon materials. Fortunately, this issue can be solved by using transfer printing technology as well [33], so a fully-integrated transceiver consisting of a transfer-printed LD, a silicon modulator and a transfer-printed PD, as schematically shown in Fig. 3.20, is expectable in the near future. It is well known that the RRH is more cost sensitive than the CO, since a lot of RRHs will be used in the future RoF systems to provide sufficient service coverage. Although the III-V-on-silicon transceiver is applied in the CO in this thesis, it can also be shifted to the RRH. In this way, the downstream link will be operated at 1310 nm and the downstream data be detected by the transfer-printed O-band PD, while the upstream link can be worked at 1550 nm, and the upstream data could be modulated by the compact and low cost C-band ring modulator.

3.4 Conclusion

In this chapter, a full-duplex RoF system based on a III-V-on-silicon transceiver is introduced. The possible techniques for III-V-on-silicon integration are firstly summarized. Then, the principle of transfer printing is introduced. Based on this technology, a III-V-on-silicon transceiver, which consists of a C-band silicon ring modulator and an O-band III-V PD, were fabricated. The performances of the C-band ring modulator and the transfer printed O-band PD were independently characterized. A wavelength-division-multiplexed full-duplex RoF is thereby established, in which the C-band silicon ring modulator is used for the electro-optic modulation of the downstream link and the O-band III-V PD is employed for the photodetection of the upstream link. Results show that an EVM of less than 6% is achieved

for the transmission of X-band 16-QAM downstream and upstream signals with 1-Gbps data rate through a 5-km RoF link. Future work may be focused on the linearity improvement of the silicon ring modulation and the transfer printing of laser source.

Reference

- [1] Z. Tang, J. Zhang, S. Pan, G. Roelkens, D. Van Thourhout, "RoF System based on a III-V-on-Silicon Transceiver with a Transfer-Printed PD," *IEEE Photonics Technology Letters*, vol. 31, no. 13, pp.1045-1048, 2019.
- [2] Z. Tang, J. Zhang, S. Pan, G. Roelkens, D. Van Thourhout, "Full-duplex Analog Radio-Over-Fiber System Based on an Integrated Transceiver With a Silicon Microring Modulator and a Transfer-Printed III-V Photodetector," in *European Conference on Integrated Optics (ECIO 2019)*, Belgium, pp. T.B2.2, 2019.
- [3] D. Van Thourhout, Z. Wang, G. Roelkens, "III-V-on-silicon integration," *Optics & Photonics News* (invited), p.34-39 (2017).
- [4] G. Roelkens, A. Abassi, P. Cardile, U. Dave, A. De Groote, Y. De Koninck, S. Dhoore, X. Fu, A. Gassenq, and N. Hattasan, "III-V-on-Silicon Photonic Devices for Optical Communication And Sensing," *Photonics*, vol. 2, no. 3, pp. 969, 2015.
- [5] L. Sanchez, F. Fournel, B. Montmayeul, L. Bally, B. Szlag, and L. Adelmini, "Collective Die Direct Bonding for Photonic on Silicon," *ECS Transactions*, vol. 86, no. 5, pp. 223-231, 2018.
- [6] X. Luo, Y. Cheng, J. Song, T.-Y. Liow, Q. J. Wang, and M. Yu, "Wafer-Scale Dies-Transfer Bonding Technology for Hybrid III/V-on-Silicon Photonic Integrated Circuit Application," *IEEE Journal of Selected Topics in Quantum Electronics*, vol. 22, no. 6, pp. 443-454, 2016.
- [7] S. Keyvaninia, G. Roelkens, D. Van Thourhout, M. Lamponi, F. Lelarge, J.-M. Fedeli, S. Messaoudene, E. Geluk, and B. Smalbrugge, "A highly efficient electrically pumped optical amplifier integrated on a SOI waveguide circuit," in *The 9th IEEE International Conference on Group IV Photonics (GFP)*, 2012, pp. 222-224.

- [8] K. Van Gasse, R. Wang, G. Roelkens, "27 dB gain III-V-on-silicon Semiconductor Optical Amplifier with > 50 mW Output Power," *Optics Express*, vol. 27, no. 1, pp.293-302, 2019.
- [9] S. Keyvaninia, S. Verstuyft, L. Van Landschoot, F. Lelarge, G.-H. Duan, S. Messaoudene, J. Fedeli, T. De Vries, B. Smalbrugge, and E. Geluk, "Heterogeneously Integrated III-V/Silicon Distributed Feedback Lasers," *Optics Letters*, vol. 38, no. 24, pp. 5434-5437, 2013.
- [10] G.-H. Duan, C. Jany, A. Le Liepvre, A. Accard, M. Lamponi, D. Make, P. Kaspar, G. Levaufre, N. Girard, and F. Lelarge, "Hybrid III-V on Silicon Lasers for Photonic Integrated Circuits on Silicon," *IEEE Journal of Selected Topics in Quantum Electronics*, vol. 20, no. 4, pp. 158-170, 2014.
- [11] T. Komljenovic, S. Srinivasan, E. Norberg, M. Davenport, G. Fish, and J. E. Bowers, "Widely Tunable Narrow-Linewidth Monolithically Integrated External-Cavity Semiconductor Lasers," *IEEE Journal of Selected Topics in Quantum Electronics*, vol. 21, no. 6, pp. 214-222, 2015.
- [12] A. Le Liepvre, C. Jany, A. Accard, M. Lamponi, F. Poingt, D. Make, F. Lelarge, J.-M. Fedeli, S. Messaoudene, and D. Bordel, "Widely wavelength Tunable Hybrid III-V/Silicon Laser with 45 nm Tuning Range Fabricated Using a Wafer Bonding Technique," in *IEEE the 9th International Conference on Group IV Photonics (GFP)*, pp. 54-56, 2012.
- [13] A. Le Liepvre, A. Accard, F. Poingt, C. Jany, M. Lamponi, D. Make, F. Lelarge, J.-M. Fedeli, S. Messaoudene, and D. Bordel, "Wavelength Selectable Hybrid III-V/Si Laser Fabricated by Wafer Bonding," *IEEE Photonics Technology Letters*, vol. 25, no. 16, pp. 1582-1585, 2013.
- [14] S. Stankovic, R. Jones, M. N. Sysak, J. M. Heck, G. Roelkens, and D. Van Thourhout, "Hybrid III-V/Si Distributed-Feedback Laser Based on Adhesive Bonding," *IEEE Photonics Technology Letters*, vol. 24, no. 23, pp. 2155-2158, 2012.
- [15] H. Park, A. W. Fang, S. Kodama, and J. E. Bowers, "Hybrid Silicon Evanescent Laser Fabricated with A Silicon Waveguide and III-V Offset Quantum Wells," *Optics Express*, vol. 13, no. 23, pp. 9460-9464, 2005.
- [16] M. E. Groenert, C. W. Leitz, A. J. Pitera, V. Yang, H. Lee, R. J. Ram, and E. A. Fitzgerald, "Monolithic Integration of Room-Temperature cw GaAs/AlGaAs Lasers on Si Substrates via Relaxed Graded GeSi Buffer Layers," *Journal of Applied Physics*, vol. 93, no. 1, pp. 362-367, 2003.

-
- [17] Y. Wan, Q. Li, A. Y. Liu, A. C. Gossard, J. E. Bowers, E. L. Hu, and K. M. Lau, "Optically Pumped 1.3 μm Room-Temperature InAs Quantum-Dot Micro-Disk Lasers Directly Grown on (001) Silicon," *Optics Letters*, vol. 41, no. 7, pp. 1664-1667, 2016.
- [18] S. Chen, W. Li, J. Wu, Q. Jiang, M. Tang, S. Shutts, S. N. Elliott, A. Sobiesierski, A. J. Seeds, and I. Ross, "Electrically Pumped Continuous-Wave III-V Quantum Dot Lasers on Silicon," *Nature Photonics*, vol. 10, no. 5, p. 307, 2016.
- [19] Z. Wang, B. Tian, M. Pantouvaki, W. Guo, P. Absil, J. Van Campenhout, C. Merckling, and D. Van Thourhout, "Room-Temperature InP Distributed Feedback Laser Array Directly Grown on Silicon," *Nature Photonics*, vol. 9, no. 12, pp. 837, 2015.
- [20] B. Tian, Z. Wang, M. Pantouvaki, P. Absil, J. Van Campenhout, C. Merckling, and D. Van Thourhout, "Room Temperature O-band DFB Laser Array Directly Grown on (001) Silicon," *Nano Letters*, vol. 17, no. 1, pp. 559-564, 2016.
- [21] Y. Shi, Z. Wang, J. Van Campenhout, M. Pantouvaki, W. Guo, B. Kunert, and D. Van Thourhout, "Optical Pumped InGaAs/GaAs Nano-Ridge Laser Epitaxially Grown on a Standard 300-mm Si Wafer," *Optica*, vol. 4, no. 12, pp. 1468-1473, 2017.
- [22] L. Megalini, B. Bonef, B. C. Cabinian, H. Zhao, A. Taylor, J. S. Speck, J. E. Bowers, and J. Klamkin, "1550-nm InGaAsP Multi-Quantum-Well Structures Selectively Grown on V-Groove-Patterned SOI Substrates," *Applied Physics Letters*, vol. 111, no. 3, p. 032105, 2017.
- [23] S. Zhu, B. Shi, and K. M. Lau, "Electrically Pumped 1.5 μm InP-based Quantum Dot Microring Lasers Directly Grown on (001) Si," *Optics Letters*, vol. 44, no. 18, pp. 4566-4569, 2019.
- [24] Y. Han, W. K. Ng, Y. Xue, K. S. Wong, and K. M. Lau, "Room Temperature III-V Nanolasers with Distributed Bragg Reflectors Epitaxially Grown on (001) Silicon-on-Insulators," *Photonics Research*, vol. 7, no. 9, pp. 1081-1086, 2019.
- [25] Y. Wan, J. Norman, Q. Li, M. J. Kennedy, D. Liang, C. Zhang, D. Huang, Z. Zhang, A. Y. Liu, A. Torres, D. Jung, A. C. Gossard, E. L. Hu, K. M. Lau, and J. E. Bowers, "1.3 μm Submilliwatt Threshold Quantum Dot Micro-Lasers on Si," *Optica*, vol. 4, no. 8, pp. 940-944, 2017.

- [26] X. Feng, M. A. Meitl, A. M. Bowen, Y. Huang, R. G. Nuzzo, and J. A. Rogers, "Competing Fracture in Kinetically Controlled Transfer Printing," *Langmuir*, vol. 23, no. 25, pp. 12555-12560, 2007.
- [27] Corbett, R. Loi, J. O'Callaghan, G. Roelkens, "Transfer Printing for Silicon Photonics," *Semiconductors and Semimetals*, 99, pp.43-70, 2018.
- [28] C. A. Bower, E. Menard, and P. E. Garrou, "Transfer printing: An approach for massively parallel assembly of microscale devices," in *58th Electronic Components and Technology Conference*, pp. 1105-1109, 2008.
- [29] G. Muliuk, N. Ye, J. Zhang, A. Abbasi, D. Van Thourhout, G. Roelkens, "Transfer Print Integration of 40 Gbps Germanium Photodiodes onto Silicon Photonic ICs," *European Conference on Optical Communication*, Sweden, pp. PDP.C.4, 2017.
- [30] G. Muliuk, K. Van Gasse, J. Van Kerrebrouck, A. J. Trindade, B. Corbett, D. Van Thourhout, G. Roelkens, "4x25Gbit/s Polarisation Diversity Silicon Photonics Receiver with Transfer Printed III-V Photodiodes," *IEEE Photonics Technology Letters*, vol. 31, no. 4, pp.287-290, 2019.
- [31] J. Juvert, T. Cassese, S. Uvin, A. De Groote, B. Snyder, L. Bogaerts, G. Jamieson, J. Van Campenhout, G. Roelkens, D. Van Thourhout, "Integration of Etched Facet, Electrically Pumped, C-Band Fabry-Perot Lasers on A Silicon Photonic Integrated Circuit By Transfer Printing," *Optics Express*, vol. 26, no. 17, pp. 21443, 2018.
- [32] R. Loi, J. O'Callaghan, B. Roycroft, C. Robert, A. Fecioru, A. J. Trindade, A. Gocalinska, E. Pelucchi, C. A. Bower, and B. Corbett, "Transfer Printing of AlGaInAs/InP Etched Facet Lasers to Si Substrates," *IEEE Photonics Journal*, vol. 8, no. 6, pp. 1-10, 2016.
- [33] J. Zhang, B. Haq, J. O'Callaghan, A. Gocalinska, E. Pelucchi, A.J. Trindade, B. Corbett, G. Morthier, G. Roelkens, "Transfer-Printing-Based Integration of a III-V-on-Silicon Distributed Feedback Laser," *Optics Express*, vol. 26, no. 7, pp.8821-8830, 2018.
- [34] A. De Groote et al., "Transfer-Printing-Based Integration of Single-Mode Waveguide-Coupled III-V-On-Silicon Broadband Light Emitters," *Optics Express*, vol. 24, no. 13, pp. 13754-13762, 2016.
- [35] B. Haq, S. Kumari, J. Zhang, K. Van Gasse, G. Roelkens, A. Gocalinsk, E. Pelucch, B. Corbett, "Micro-transfer-printed III-V-on-Silicon C-band SOAs with 17 dB Gain," in *IEEE Photonics Conference 2019*, 2019.

-
- [36] L. Abdollahi Shiramin, A. Bazin, S. Verstuyft, S. Lycke, P. Vandenabeele, G. Roelkens, D. Van Thourhout, "Transfer Printing of Micron-Size Graphene for Photonic Integrated Circuits and Devices," *ECS Journal of Solid State Science and Technology*, vol. 6, no. 7, pp.435-439, 2017.
- [37] N. Mahmoud, W. Walravens, J. Kuhs, C. Detavernier, Z. Hens, G. Roelkens, "Micro-Transfer-Printing of Al₂O₃-Capped Short-Wave-Infrared PbS Quantum Dot Photoconductors," *ACS Applied Nano Materials*, vol. 2, no. 1, pp.299-306, 2019.
- [38] J. Zhang, A. De Groote, A. Abbasi, R. Loi, J. O'Callaghan, B. Corbett, A. Jose Trindade, C. A. Bower, G. Roelkens, "A Silicon Photonics Fiber-To-The-Home Transceiver Array based on Transfer-Printing-Based Integration of III-V Photodetectors," *Optics Express*, vol. 25, no. 13, pp.14290-14299, 2017.
- [39] R. Marchetti, C. Lacava, A. Khokhar, X. Chen, I. Cristiani, D. J. Richardson, G. T. Reed, P. Petropoulos, and P. Minzioni, "High-Efficiency Grating-Couplers: Demonstration of A New Design Strategy," *Scientific Reports*, vol. 7, no. 1, p. 16670, 2017.
- [40] A. Hosseinzadeh and C. T. Middlebrook, "Highly Linear Dual Ring Resonator Modulator for Wide Bandwidth Microwave Photonic Links," *Optics Express*, vol. 24, no. 24, pp. 27268-27279, 2016.
- [41] S. Agarwal, M. Ingels, M. Pantouvaki, M. Steyaert, P. Absil, J. Van Campenhout, "Wavelength Locking of a Si Ring Modulator Using an Integrated Drop-Port OMA Monitoring Circuit," *IEEE Journal of Solid-State Circuits*, vol. 51, no. 10, pp. 2328-2344, 2016.

Chapter 4

Microwave Doppler frequency shift measurement based on coherent receiver

IN *this chapter, we propose a silicon integrated coherent receiver, which consists of an optical 90-degree hybrid and a pair of balanced photodetectors. The optical 90-degree hybrid is realized by a 2×4 multimode interference coupler, which has a small footprint and does not need additional thermal tuners. The balanced photodetector is implemented by a pair of germanium-silicon photodetectors working at photocurrent subtraction mode. Based on the proposed coherent receiver, a photonic-based Doppler frequency shift measurement system is demonstrated. The doppler frequency shift value can be obtained by measuring the frequency of the downconverted intermediate frequency signal, and more importantly, the direction of the Doppler frequency shift (which is used to determine the moving direction of the targets) can also be identified by comparing the phase difference between the quadrature outputs of the proposed coherent receiver. The state-of-the-art of photonic Doppler frequency shift measurement methods is briefly reviewed. The performance of the integrated coherent receiver and the proposed Doppler frequency shift measurement system will be presented. The material presented in this chapter has in part been published in [1].*

4.1 Introduction

The Doppler effect, a well-known effect named after Austrian scientist Christen Doppler, is denoted as the frequency change between the observed frequency and the emitted frequency, when the observer is moving relative

to the source of the waves. It is widely used in a lot of different applications, such as robotics to aid the movement of robots to avoid obstacles in a complex environment [2], Doppler radars to measure the velocities of moving vehicles [3-5] or the human gestures for human-machine interaction [6, 7], Doppler ultrasonography for medical imaging [8], Doppler velocimeters to measure the velocities in a fluid flow [9], and satellite communications to dynamically monitor and compensate the Doppler frequency change due to earth curvature [10] and so on. To explain the principle of the Doppler effect, let's take the Doppler radar as an example. In a Doppler radar system, if the emitter frequency is f_t , and the observed frequency is f_r , they have a following relationship

$$f_r = f_t \left(\frac{1+v/c}{1-v/c} \right) \quad (1)$$

where c is the speed of light, v is the velocity of the target. Then (1) simplifies to

$$f_r = f_t \left(\frac{c+v}{c-v} \right) \quad (2)$$

The beat frequency between the emitter frequency f_t and the observed frequency f_r is denoted as f_d , and is called the Doppler frequency shift (DFS). From (2), the DFS can be express as

$$f_d = f_r - f_t = 2v \frac{f_t}{(c-v)} \quad (3)$$

Since for most radar application systems, the target velocity $v \ll c$ (the light speed), $c-v$ can be approximated as c , therefore we can obtain

$$f_d \approx 2v \frac{f_t}{c} \quad (4)$$

The DFS is positive when the target is moving towards the radar and it is negative when the target is moving away from the radar. The target velocity can also be derived from (4) as

$$v \approx \frac{c}{2f_t} |f_d| \quad (5)$$

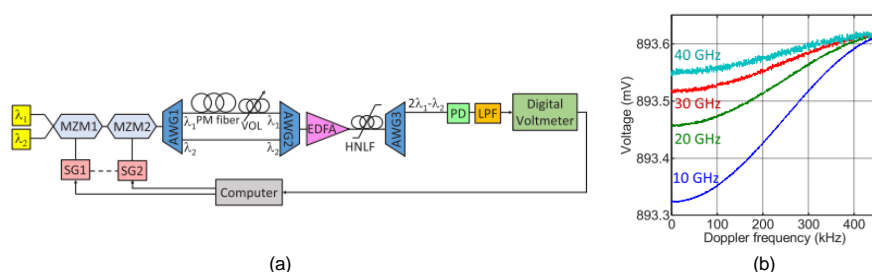


Fig. 4.1. Photonic DFS measurement system based on FWM in HNLf (figure from [13]). (a) schematic diagram and (b) typical results at different carrier frequencies.

As can be easily seen from (5), to obtain the full information (i.e., velocity and direction) of a moving target, both the DFS value and the DFS direction, should be precisely measured.

Conventionally, a DFS measurement is based on pure electronic technologies. However, different systems may be operated at different frequency bands, ranging from several MHz to even the THz band and a DFS measurement system with broad bandwidth is hard to realize by electronic methods due to the electrical bottleneck of limited bandwidth. To solve this problem, a photonics-based DFS measurement technology is considered as one of the most promising solutions, due to its advantages of wide bandwidth, light weight, low transmission loss and immunity to EMI (can support multiband and multichannel measurement) [11, 12]. Several photonics-based approaches are used to perform a DFS measurement. For example, in [13, 14], a DFS measurement system based on the nonlinear FWM effect in a highly nonlinear fiber (HNLf) was realized, as shown in Fig. 4.1 (a). Two optical carriers with wavelengths of λ_1 and λ_2 are combined and sent to two cascaded MZMs (MZM1 and MZM2), which are respectively modulated by a transmitted signal with an angular frequency of Ω and an echo signal with an angular frequency of $\Omega + \Omega_d$ (Ω_d is the DFS that should be measured). After cascaded modulation, the optical signal is separated by an AWG. The λ_1 signal is delayed by τ by using a length of polarization maintaining fiber (PMF) and an optical variable delay line (OVDL). Then, the two optical signals are recombined by another AWG and sent to a length of HNLf after optical amplification by an EDFA. Due to the FWM effect, two

new optical components located at the wavelengths of $2\lambda_1-\lambda_2$ and $2\lambda_2-\lambda_1$ are generated. One of the newly generated components ($2\lambda_1-\lambda_2$ for example) is selected by an optical filter (AWG3) and applied to a PD. Finally, a low pass filter (LPF) is connected after the PD and a digital voltmeter is used to obtain the DC component, which is given by

$$V_{\text{DC}} \propto 1 - 8\alpha^4 \cos 2\Omega\tau - 8\alpha^4 \cos \Omega_d\tau \quad (6)$$

where α is the modulation index, which is related to the amplitude of the RF signal and the half-wave voltage of the MZMs. As can be seen from (6), the obtained DC component is a function of both the angular frequency of the transmitted signal Ω and the DFS Ω_d . The transmitted frequency is known, since it is generated by the radar itself, so the only unknown value in (6) is the DFS. Thus, by measuring the DC component output from the system, the DFS can be measured. This method has the advantage of wide bandwidth. Fig. 4.1(b) shows the typical results, in which the measured DC voltages for a DFS ranging from 0 to 456 kHz at different carrier frequencies are presented. However, this method relies on the nonlinear effect, which leads to a poor measurement accuracy. Moreover, as can be seen from (6), the relationship between the measured DC voltage and the DFS is a *cos-liked* nonlinear relationship, which means that this measurement system has an unambiguous range of half a period of the cosine function, and different DFS ranges have different sensitivities and accuracies.

According to the aforementioned principle, the DFS is the frequency difference between the transmitted signal and the echo signal. Frequency mixers are widely known as efficient devices for obtaining the frequency difference between the two input signals, so another photonic DFS measurement scheme is based on microwave photonic mixing. The most common photonic DFS measurement system based on a microwave photonic mixer is shown in Fig. 4.2 [15]. An optical carrier with an angular frequency of ω_c is sent to an MZM (MZM1), which is modulated by a transmitted signal with an angular frequency of Ω . If MZM1 is biased at the quadrature transmission point (QTP), the output of MZM1 is given by

$$E = \frac{\sqrt{P_{\text{in}}}}{2} \exp(j\omega_c t) \left[\exp\left(j\beta_1 \cos \Omega t + j\frac{\pi}{2}\right) + \exp(-j\beta_1 \cos \Omega t) \right] \quad (7)$$

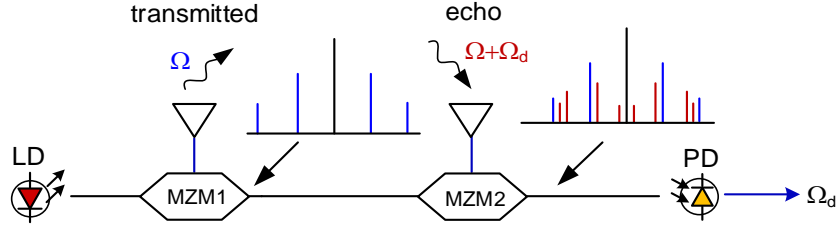


Fig. 4.2. Photonic DFS measurement system based on a microwave photonic mixer by using cascaded MZMs.

where P_{in} is the optical power of the optical carrier, β is the modulation index of the transmitted signal. By using Bessel function expanding, (7) can be rewritten as

$$E = \frac{\sqrt{P_{in}}}{2} \exp(j\omega_c t) \cdot \sum_{n=-\infty}^{\infty} \left[j^{n+1} J_n(\beta_1) \exp(jn\Omega t) + j^n J_n(\beta_1) \exp(-jn\Omega t) \right] \quad (8)$$

where $J(\cdot)$ is the Bessel function of the first kind. Then the optical signal is modulated by an echo signal through another MZM (MZM2). If the angular frequency of the echo signal is $\Omega + \Omega_d$, the output signal is given by

$$E = \frac{\sqrt{P_{in}}}{2} \exp(j\omega_c t) \cdot \sum_{n=-\infty}^{\infty} \sum_{m=-\infty}^{\infty} \left\{ \begin{aligned} & j^{n+1} J_n(\beta_1) J_m(\beta_2) \exp[j(n\Omega + m\Omega + m\Omega_d)t] \\ & + j^n J_n(\beta_1) J_m(\beta_2) \exp[-j(n\Omega + m\Omega + m\Omega_d)t] \end{aligned} \right\} \quad (9)$$

As can be seen from (9), due to the nonlinearity of the electro-optic modulation, a lot of optical sidebands are generated in the optical domain. If only the 1st-order sidebands are taken into consideration (this is reasonable due to the small signal modulation) and the optical signal after cascaded modulation is sent to a PD to perform photodetection, a downconverted IF signal with a frequency equals to the frequency difference between the transmitted signal and the echo signal can be obtained, which can be expressed as

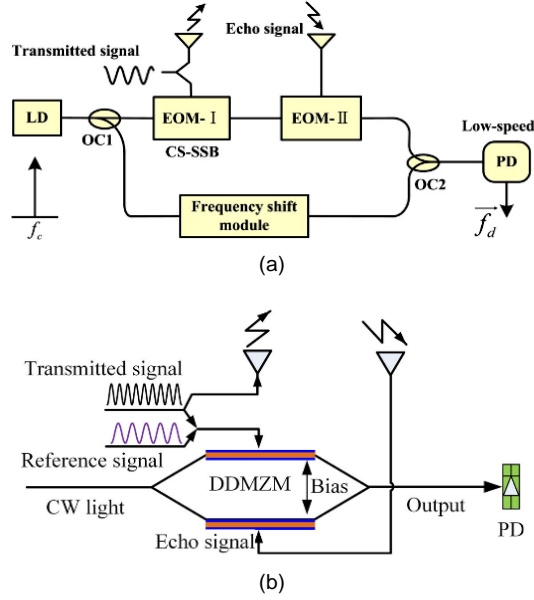


Fig. 4.3. Photonic DFS measurement system with direction identification. (a) based on frequency shift module (figure from [17]), (b) additional reference RF signal (figure from [18]). LD, laser diode; OC, optical coupler; EOM, electro-optic modulator; PD, photodetector; DMZM, dual-drive Mach-Zehnder modulator.

$$i \propto J_1(\beta_1) J_1(\beta_2) \cos \Omega_d t \quad (10)$$

Therefore, the DFS information can be obtained by measuring the frequency of the downconverted IF signal. Since the frequency of the IF signal can be measured by an electrical spectrum analyser with high resolution, this kind of DFS measurement system usually has a high resolution and a high accuracy. Based on a similar method, an improved DFS estimation system with an improved measurement resolution was proposed in [16].

However, given the square-law detection of the PD, no matter if the method based on FWM mixing [13, 14] or the approach based on the microwave photonic mixer [16] is used, only the magnitude of the DFS is obtained and the direction of the DFS cannot be identified. To solve this problem, some solutions have been reported. For instance, in [17], a frequency shift module realized by an acousto-optic modulator (AOM) was

used, which is shown in Fig. 4.3(a). In this system, an optical carrier is split into two branches. In the upper branch, the optical carrier is modulated by the transmitted signal by using carrier-suppressed single sideband (CS-SSB) modulation, thus an 1st-order sideband is generated, which can be described by

$$E = \frac{\sqrt{2}}{2} \sqrt{P_{\text{in}}} J_1(\beta_1) \exp[j(\omega_c + \Omega)t] \quad (11)$$

Then the optical sideband is remodulated by an echo signal, and the output signal can be written as

$$E = \frac{\sqrt{2}}{2} \sqrt{P_{\text{in}}} \left\{ jJ_1(\beta_1) J_1(\beta_2) \exp[j(\omega_c - \Omega_d)t] \right. \\ \left. + J_1(\beta_1) J_0(\beta_2) \exp[j(\omega_c + \Omega)t] + jJ_1(\beta_1) J_1(\beta_2) \exp[j(2\omega_c + \Omega_d)t] \right\} \quad (12)$$

In the lower branch, an AOM is inserted to realize an optical frequency shift with an amount of Ω_s , so the frequency-shifted optical carrier in the lower branch can be expressed as

$$E = \frac{\sqrt{2}}{2} \sqrt{P_{\text{in}}} J_1(\beta_1) \exp[j(\omega_c + \Omega_s)t] \quad (13)$$

The optical signals in the two branches are combined and sent to a PD. Due to the frequency beating between the optical sidebands and the frequency-shifted optical carrier, the output photocurrent is given by

$$i \propto \cos \Delta\Omega t = \begin{cases} \cos(\Omega_s - \Omega_d)t, & \Omega_d > 0 \\ \cos(\Omega_s + \Omega_d)t, & \Omega_d < 0 \end{cases} \quad (14)$$

As can be seen from (14), by adding a frequency-shift module, different DFS directions will generate IF signals with different frequencies, thus both the DFS value and direction can be obtained.

Similarly, in [18] a reference RF signal is used to identify the direction of the DFS. The system architecture is shown in Fig. 4.3(b). A reference RF signal

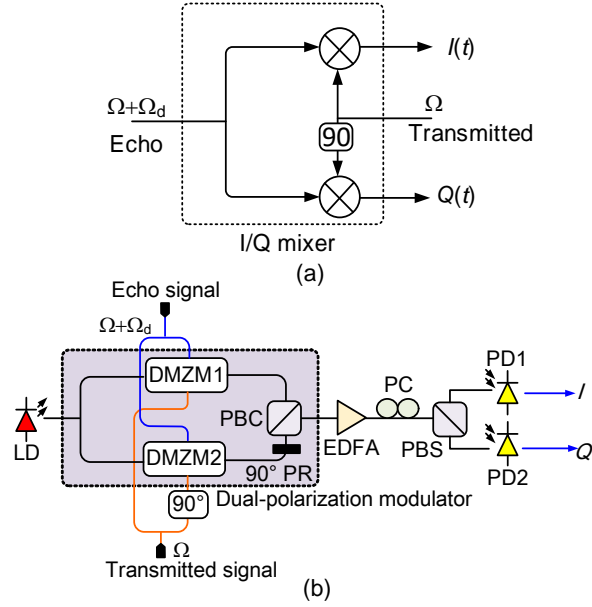


Fig. 4.4. DFS measurement system with direction identification based on a photonic I/Q mixer. (a) equivalent electrical structure and (b) an example of photonic DFS measurement system based on dual-polarization modulator.

with an angular frequency of Ω_r is combined with the transmitted signal and send to one of the RF ports of a DMZM. Then optical components with frequencies of ω_c , $(\omega_c \pm \Omega)$ and $(\omega_c \pm \Omega_r)$ are generated. It should be noted that the higher-order (≥ 2) sidebands are not considered under the small signal modulation. In the other arm of the DMZM, the optical carrier is modulated by an echo signal, so optical components with frequencies of ω_c and $(\omega_c \pm \Omega_d)$ are produced. The output signal of the DMZM is directly applied to the PD to realize photodetection, then the obtained electrical signal can be written as

$$i \propto \cos \Omega_d t + \cos(\Omega_r - \Omega)t + \cos(\Omega_r - \Omega - \Omega_d)t \quad (15)$$

As can be seen, by adding a reference RF signal, two extra IF signals with frequencies of $(\Omega_r - \Omega)$ and $(\Omega_r - \Omega - \Omega_d)$ are generated, in addition to the desired DFS signal (Ω_d). More importantly, if the DFS is positive, the component $(\Omega_r - \Omega)$ has a higher frequency than that of $(\Omega_r - \Omega - \Omega_d)$, while if the DFS is negative, the component $(\Omega_r - \Omega)$ has a lower frequency than that of $(\Omega_r - \Omega - \Omega_d)$.

Therefore, by comparing the frequencies of the beat signals, the direction of the DFS can be distinguished.

Another powerful solution is based on photonic I/Q frequency mixing [19-22]. The equivalent electrical structure of this kind of DFS measurement method is shown in Fig. 4.4(a). Using an I/Q mixer, the echo signal is split into two parts and mixed with a pair of quadrature shifted transmitted signals, as can be seen from Fig. 4.4(a), thus a pair of IF signals with quadrature phase difference can be produced, which are given by

$$\begin{aligned} I(t) &\propto \cos(\Omega + \Omega_d)t \cdot \cos \Omega t = \frac{\cos \Omega_d t + \cos(2\Omega + \Omega_d)t}{2} \\ Q(t) &\propto \cos(\Omega + \Omega_d)t \cdot \sin \Omega t = \frac{-\sin \Omega_d t + \sin(2\Omega + \Omega_d)t}{2} \end{aligned} \quad (16)$$

If an LPF is connected to each of the output ports, a pair of DFS signals can be obtained

$$\begin{cases} I_{\text{DFS}}(t) = \frac{\cos \Omega_d t}{2} \\ Q_{\text{DFS}}(t) = -\frac{\sin \Omega_d t}{2} \end{cases} \quad (17)$$

As can be seen from (17), the DFS value can be easily estimated by measuring the frequency of the IF signal, and more important, the directional information can be acquired by comparing the phases of the two quadrature IF signals. Specifically, if the DFS is positive, the quadrature IF signal ($Q_{\text{DFS}}(t)$) is advanced by $\pi/2$ with respect to the in-phase IF signal ($I_{\text{DFS}}(t)$). In contrast, if $Q_{\text{DFS}}(t)$ is delayed by $\pi/2$ with respect to $I_{\text{DFS}}(t)$, the direction of the DFS is negative, which means that the target is moving away from the observer.

Based on this idea, different photonic I/Q mixers were proposed to realize photonic DFS measurements with direction identification. For instance, in [19], a dual-polarization modulator is used, which is presented in Fig. 4.4(b). A transmitted signal is split into two quadrature portions by a 90-degree electrical hybrid coupler, and an echo signal is divided into two paths by an electrical power divider. One part of the transmitted signal and one part of the echo signal are sent to a sub-DMZM of the dual-polarization modulator,

and the other parts of the transmitted and echo signals are applied to the other sub-DMZM. After polarization demultiplexing, the two orthogonal optical signals are sent to two PDs. Since each sub-DMZM functions as a microwave photonic mixer along the two orthogonal polarization directions, the DFS value can be obtained by measuring the frequency of the IF signal obtained from either polarization direction. More importantly, as a pair of quadrature transmitted signals is applied to the two sub-DMZMs, the obtained IF signals along the two polarization directions are in quadrature, thereby the direction of the DFS can be derived as well.

The photonic I/Q mixer in [19], however, is realized by an electrical 90-degree hybrid, with which it is hard to achieve precise 90-degree microwave phase difference over a wide bandwidth. So, a more attractive method is to use a microwave photonic phase shifter instead of the electrical 90-degree hybrid. In [20], a microwave photonic phase shifter is deployed, in which a DPMZM is used to convert the transmitted and echo signals to the optical domain through the two child-MZMs inside of the DPMZM. An AWG is then used to separate the positive and negative 1st-order sidebands. Next a DC-bias voltage is applied to the farther-MZM of the DPMZM to introduce a 45-degree optical phase difference between the two output branches of the AWG. After photodetection, a 90-degree microwave phase difference exists between the two IF signals, thus photonic I/Q mixing is achieved. In [21], a microwave photonic phase shifter based on a PolM is used. A phase modulator (PM) and a PolM are used to imprint the transmitted signal and echo signal respectively. An OBPF is employed to select the +1st-order sidebands to generate an optical SSB-modulated signal. Then the optical SSB-modulated signal is split to two paths. Each path is sent to a PD after a polarizer, which is used to extract the optical signal along the polarization direction that has an angle of α to one of the principal axes of the PolM [23]. By adjusting the two polarizers in the two paths to change the angle of α , a 90-degree microwave phase difference can also be introduced to the downconverted IF signals, and then a photonic I/Q mixer for photonic DFS measurement is realized.

A photonic I/Q mixer can also be implemented by using a 90-degree optical hybrid. 90-degree optical hybrids are originally invited to realize demodulations in coherent optical communication systems [24]. The

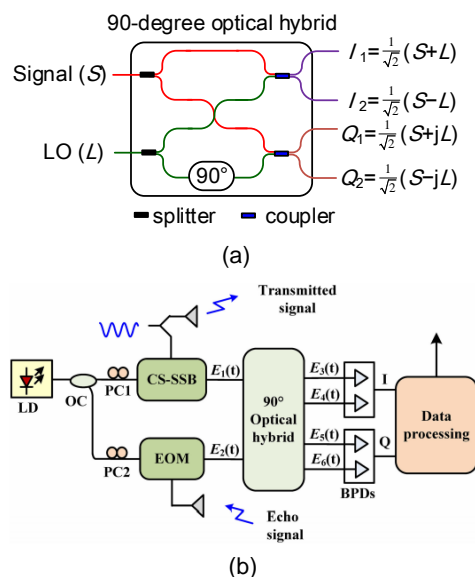


Fig. 4.5. DFS measurement system with direction identification based on a I/Q mixer by using a 90-degree optical hybrid. (a) structure of the 90-degree optical hybrid, and (b) photonic DFS measurement system (figure from [22]).

structure of the 90-degree optical hybrid is shown in Fig. 4.5(a). It is a six-port device, which consists of two 1x2 optical splitters, two 2x2 optical couplers and a 90-degree optical phase shifter. An optical signal, denoted as the *signal* light (S) and another optical signal, denoted as the *LO* light (L) are sent to the 90-degree optical hybrid via the different input ports. In the optical hybrid, the *signal* light and the *LO* light are split into two equal branches by the 1x2 optical splitters. In one branch of the *LO* light, a 90-degree optical phase shifter is inserted to introduce a 90-degree optical phase difference. Then the two *signal* lights and the two *LO* lights are combined with each other through the 2x2 optical couplers. If we assume that the optical splitters, optical couplers and the optical phase shifter are ideal devices, the transmission matrix of this 90-degree optical hybrid is given by

$$[J] = \begin{bmatrix} \frac{1}{\sqrt{2}} & \frac{1}{\sqrt{2}} \\ \frac{1}{\sqrt{2}} & -\frac{1}{\sqrt{2}} \\ \frac{1}{\sqrt{2}} & j\frac{1}{\sqrt{2}} \\ \frac{1}{\sqrt{2}} & -j\frac{1}{\sqrt{2}} \end{bmatrix} \quad (18)$$

so, the four output signals can be expressed as

$$[J] \begin{bmatrix} S \\ L \end{bmatrix} = \begin{bmatrix} \frac{1}{\sqrt{2}} & \frac{1}{\sqrt{2}} \\ \frac{1}{\sqrt{2}} & -\frac{1}{\sqrt{2}} \\ \frac{1}{\sqrt{2}} & j\frac{1}{\sqrt{2}} \\ \frac{1}{\sqrt{2}} & -j\frac{1}{\sqrt{2}} \end{bmatrix} \begin{bmatrix} S \\ L \end{bmatrix} = \frac{1}{\sqrt{2}} \begin{bmatrix} S+L \\ S-L \\ S+jL \\ S-jL \end{bmatrix} \quad (19)$$

If the *signal* light and *LO* light are expressed as

$$\begin{bmatrix} S \\ L \end{bmatrix} = \begin{bmatrix} \exp j(\omega_s t + \phi_s(t)) \\ \exp j(\omega_L t + \phi_L(t)) \end{bmatrix} \quad (20)$$

where ω_s and ω_L are angular frequencies of the *signal* light and the *LO* light, and $\phi_s(t)$ and $\phi_L(t)$ are the corresponding optical phases. When substituting (20) into (19), the four output signals can be written as

$$\begin{bmatrix} I_1 \\ I_2 \\ Q_1 \\ Q_2 \end{bmatrix} = \frac{1}{\sqrt{2}} \begin{bmatrix} \exp j(\omega_s t + \phi_s(t)) + \exp j(\omega_L t + \phi_L(t)) \\ \exp j(\omega_s t + \phi_s(t)) - \exp j(\omega_L t + \phi_L(t)) \\ \exp j(\omega_s t + \phi_s(t)) + j \exp j(\omega_L t + \phi_L(t)) \\ \exp j(\omega_s t + \phi_s(t)) - j \exp j(\omega_L t + \phi_L(t)) \end{bmatrix} \quad (21)$$

If four PDs are connected to the four output ports of the 90-degree optical hybrid, four electrical signals with different microwave phases are generated, which can be expressed as

$$\begin{bmatrix} i_{I_1} \\ i_{I_2} \\ i_{Q_1} \\ i_{Q_2} \end{bmatrix} = \frac{1}{2} \begin{bmatrix} \cos[(\omega_s - \omega_L)t + \phi_s(t) - \phi_L(t)] \\ -\cos[(\omega_s - \omega_L)t + \phi_s(t) - \phi_L(t)] \\ \sin[(\omega_s - \omega_L)t + \phi_s(t) - \phi_L(t)] \\ -\sin[(\omega_s - \omega_L)t + \phi_s(t) - \phi_L(t)] \end{bmatrix} \quad (22)$$

According to the phase relationship between the four outputs of the 90-degree optical hybrid shown in (22), $(S+L)$ and $(S-L)$ are usually denoted as the in-phase outputs and $(S+jL)$ and $(S-jL)$ are usually denoted as the quadrature outputs. Since the in-phase outputs and the quadrature outputs have a 90-degree microwave phase difference, photonic I/Q mixing can be performed if the *signal* light and the *LO* light carry the transmitted signal and the echo signal, respectively, thereby a photonic DFS measurement with direction detection can be achieved.

Fig. 4.5(b) shows a photonic DFS measurement system based a 90-degree optical hybrid [22]. An optical carrier is split into two paths and modulated by the transmitted signal and the echo signal, respectively. An OBPF is inserted in each path the selected the positive 1st-order sidebands, which can be written as

$$\begin{bmatrix} S \\ L \end{bmatrix} = \begin{bmatrix} J_1(\beta_2) \exp j(\omega_c + \Omega + \Omega_d)t \\ J_1(\beta_1) \exp j(\omega_c + \Omega)t \end{bmatrix} \quad (23)$$

Taking an in-phase output (e.g., I_1) and a quadrature (e.g., Q_1) output into account, they can be expressed as

$$\begin{bmatrix} I_1 \\ Q_1 \end{bmatrix} = \begin{bmatrix} J_1(\beta_2) \exp j(\omega_c + \Omega + \Omega_d)t + J_1(\beta_1) \exp j(\omega_c + \Omega)t \\ J_1(\beta_2) \exp j(\omega_c + \Omega + \Omega_d)t + jJ_1(\beta_1) \exp j(\omega_c + \Omega)t \end{bmatrix} \quad (24)$$

According to (22), a pair of quadrature IF signals can be obtained

$$\begin{bmatrix} i_{I_1} \\ i_{Q_1} \end{bmatrix} = J_1(\beta_2)J_1(\beta_1) \begin{bmatrix} \cos \Omega_d t \\ \sin \Omega_d t \end{bmatrix} \quad (25)$$

Tab. 4.1. Comparison between 90-degree optical hybrid and the electrical quadrature hybrid coupler and microwave photonic phase shifter

Ref	Type	BW [Hz]	Amp. Im. [dB]	Pha. Im. [deg.]	Iso. [dB]
[25]	OH	191~192 T	± 0.5	± 2	>40
[26]	EH	1.7~36 G	± 0.7	± 12	>12
[27]	EH	10~40 G	± 0.7	± 10	>12
[23]	MPPS	11~43 G	pha. & amp. coupl. ± 0.5 dB		medium
[28]	MPPS	0~14 G	pha. & amp. coupl. ± 1.5 dB		medium
[29]	MPPS	0~18 G	pha. & amp. coupl. ± 3 dB		medium

(OH: optical hybrid; EH: electrical hybrid; MPP: microwave photonic phase shifter; BW: bandwidth; Amp. Imb.: amplitude imbalance; Pha. Imb.: phase imbalance; Iso: isolation; pha. & amp. coupl.: phase and amplitude coupling.)

As can be seen from (25), photonic I/Q mixing is realized and a DFS measurement with the capability of direction identification is enabled.

Obviously, in this method, the DFS measurement performance relies highly on the quality of the I/Q mixer, especially the amplitude and phase imbalances between the two quadrature outputs. That is to say, the photonic microwave I/Q mixer is expected to have a wide bandwidth and low amplitude and phase imbalances. Tab. 4.1 presents the comparison between the 90-degree optical hybrid and the electrical 90-degree hybrid coupler and the microwave photonic phase shifter. As can be seen from Tab. 4.1, the 90-degree optical hybrid, compared with the conventional electrical 90-degree hybrid coupler [19] and the microwave photonic phase shifter [20, 21], has the lowest phase and amplitude imbalances and a weaker amplitude and phase coupling. Therefore, in this thesis, the proposed DFS measurement system is also based on the microwave photonic mixer using a 90-degree optical hybrid.

4.2 Integrated coherent receiver

As can be seen from the principle presented in Section 4.1, the most important component used in the photonic I/Q mixer for the direction identification of

the DFS measurement is the 90-degree optical hybrid. In the following section, a brief introduction to the 90-degree optical hybrid is firstly given.

Back to 1990, to increase the capacity of the optical communication system, coherent communication technology was first investigated [30]. Different from the then dominant on/off-keying (OOK) modulation in conjunction with direct detection, which only modulates and detects the amplitude of the light, coherent communication can detect not only the amplitude but also the phase and polarization. Since more freedoms (i.e., optical phase and polarization) are used, coherent communication systems can support more data within the same optical bandwidth.

However, the advantages of coherent communication systems cannot be achieved without the following requirements: 1) optical frequency stabilization is required to stabilize the frequency difference between the transmitter and receiver; 2) frequency chirp and noise should be eliminated; 3) an optical “mixer” to combine the *signal* light from the transmitter and the *LO* light used in the receiver is needed. Unfortunately, since these requirements could not be fulfilled with technologies available in the early 1990s, and an alternative low-cost solution based on WDM and optical amplification (enabled by the invention of EDFAs) was adopted and commercialized, coherent optical communications did not break through at that time.

Fortunately, with the improvements in both hardware and software, coherent technologies are now feasible and playing a very important role in today’s communication systems. Stabilization of the frequency difference between the transmitter and the receiver, and elimination of the noise and the chirp can be realized by mature and now commercially-available digital signal processors and the function of optical “mixer” can be implemented by a six-port 90-degree optical hybrid.

Conventionally, several techniques are employed to fabricate this device, which is shown in Fig. 4.6. Firstly, according to the principle of 90-degree optical hybrids, the most straightforward way is to use optical splitter/combiners and an optical phase shifter. Fig. 4.6(a) shows an example based on all fiber-based devices. In this structure, two 50:50 fiber optical splitters, two 2×2 optical fiber combiners and a fiber based phase shifter are used. This fiber-based structure can also be implemented in silica-based

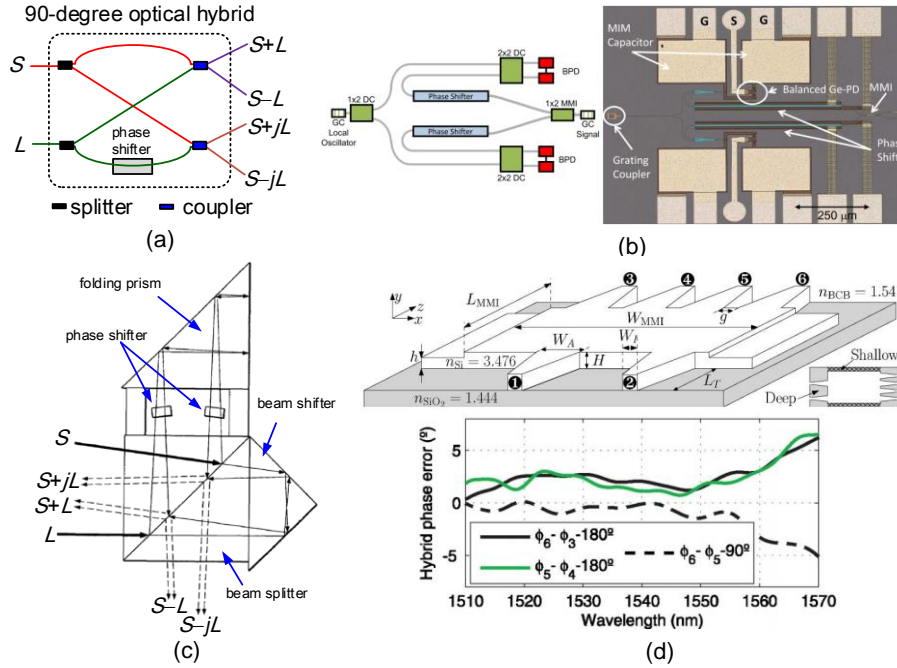


Fig. 4.6. Different types of 90-degree optical hybrid. (a) Fiber-based optical hybrid, (b) SOI-based optical hybrid (coupled with two balanced PDs) (figure from [34]), (c) free-space optical hybrid (figure from [37]), (d) MMI-based optical hybrid on SOI platform (from [44]).

planar lightwave circuits (PLC) [31, 32], LiNbO₃-based circuits [33], or SOI circuits (shown in Fig. 4.6(b)) [34, 35]. However, fiber-based 90-degree optical hybrids are bulky and sensitive to mechanical shock and vibration. Moreover, this kind of 90-degree optical hybrid, no matter if it is based on fiber devices or integrated devices, is sensitive to the temperature of the environment, which means that strict temperature control is necessary to maintain the precise optical path difference to ensure an exact optical phase difference between the four output ports of the optical hybrid [36], which increases the complexity for control of the system.

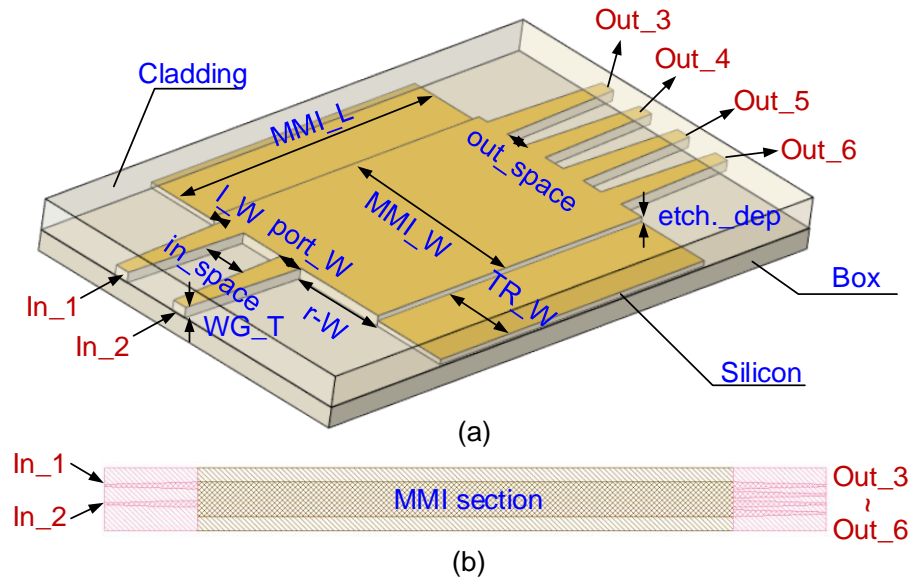


Fig. 4.7. The proposed 90-degree optical hybrid based on silicon MMI. (a) Layout and (b) GSD figure.

Tab. 4.2 Key parameters of the designed MMI-based optical hybrid

Parameter	Definition	Value (μm)
In_1	Input port 1	-
In_2	Input port 2	-
Out_3	Output port 3	-
Out_4	Output port 4	-
Out_5	Output port 5	-
Out_6	Output port 6	-
in_space	spacing between the input ports	2.5
port_W	width of the in/out waveguides	1.5
l_W	spacing between In_1 and the left edge	0.1
r_W	spacing between In_2 and the right edge	2.1
out_space	spacing between the output ports	0.5
etch_dep	etching depth	0.07
MMI_L	length of the MMI section	115.5
MMI_W	width of the MMI section	7.7
TR_W	width of the trenches	3
WG_T	thickness of the in/output waveguides	0.22

Another kind of 90-degree optical hybrid is based on a Michelson interferometer, realized by free-space bulk-optics devices [37] as shown in Fig. 4.6(c). As can be seen, it mainly consists of a 50:50 optical beam splitter, a folding prism, an optical beam shifter and two optical phase shifters (transparent slabs). The *signal* light and *LO* light are injected from two different angles and then respectively split into two paths through the 50:50 optical beam splitter. The right components are sent to the beam shifter and return to the center of the optical beam splitter. The upper components are transmitted to the folding prism after going through two different optical phase shifters. In the prism, the lights are reflected on the surface and return to the center of the optical beam splitter as well. Then the signal light and the LO light interfere with each other, and four output signals with specific optical phase differences are obtained. Free-space based 90-degree optical hybrids have low insertion loss and are not sensitive to temperature variation and mechanical shock since the *signal* light and the *LO* light share the same optical devices, therefore this is the main strategy for the current commercially-available 90-degree optical hybrid [25, 38]. But, this device has a relatively large size, and more importantly, cannot be integrated with other devices, such as electro-optic modulators or PDs, which is against the trend of photonic integration in order to reduce the cost of the communication systems.

To solve this problem, a third type of 90-degree optical hybrid attracted significant interest in recent years. The key feature of this type of optical hybrid is that it is based on a single device (e.g. an MMI), which is realized in a high-index-contrast platform. For instance, [39-41] present several 90-degree optical hybrids based on an InP platform, and due to the compatibility with the mature CMOS technology, SOI-based 90-degree optical hybrids are also reported in the literature [42-45]. E.g. Fig. 4.6(d), shows a six-port optical hybrid based on an MMI fabricated on the SOI platform [44]. *Signal* light and *LO* light are injected into this chip through port 1 and port 2. In the multimode section, the incoming two lights are expanded into multiple modes. After traveling with different propagation constants and different optical lengths, the input *signal* light and the *LO* light will interfere at the four output ports (port 3 to port 6) of the MMI. By precisely designing the size of the multimode section, a 90-degree optical phase difference can be

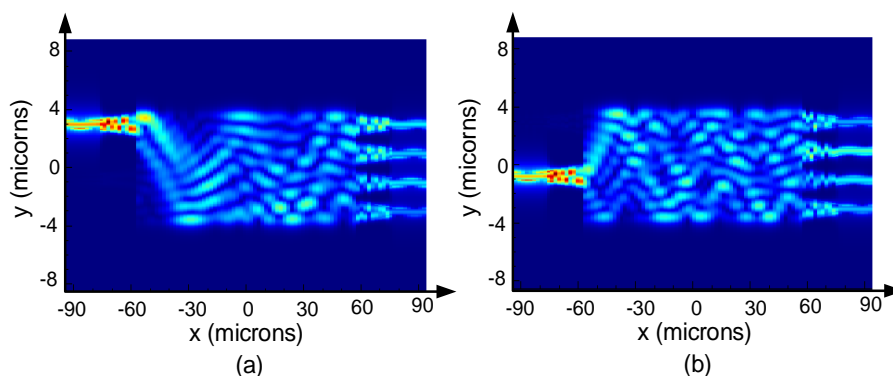


Fig. 4.8. Simulated mode distributions of the proposed MMI. Optical signal is injected from (a) In_port 1 and (b) In_port 2.

introduced, and thus a 90-degree optical hybrid is obtained. It can be easily seen that this kind of 90-degree optical hybrid is passive, which means that the fabrication cost will be relatively low. More importantly, no active control is required to stabilize the 90-degree optical phase difference, which reduces the complexity further.

In this thesis, an MMI-based silicon 90-degree optical hybrid proposed by J. Zhang from our group is employed [45]. It is fabricated in the IMEC iSIPP25G platform. The layout of the MMI-based 90-degree optical hybrid is shown in Fig. 4.7 (a) and the mask layout is presented in Fig. 4.7(b). As can be seen, the MMI is fabricated on a typical SOI wafer, with a 220 nm thick silicon core on a 2 micrometre SiO₂ box and SiO₂ cladding. The two waveguides for the two optical inputs (In₁ and In₂) and the four waveguides for the four optical outputs (Out₃, Out₄, Out₅ and Out₆) are fully-etched waveguides with a thickness of 220 nm (WG_T). They are tapered waveguides, with an initial waveguide width of 0.45 μm and a terminal waveguide width (port_W) of 1.5 μm . For the input site, the spacing between the input waveguides (in_{space}) is 2.5 μm and the width between In₁ and the left edge (l_W in Fig. 4.7(a)) is 0.1 μm , and the width between In₂ and the right edge (r_W) is 2.1 μm . For the output site, the four output waveguides are uniformly designed, with a port spacing (out_{space}) of 0.5 μm . For the MMI section, in order to reduce the phase error and amplitude imbalance between the output ports, a shallow-etched waveguide is used.

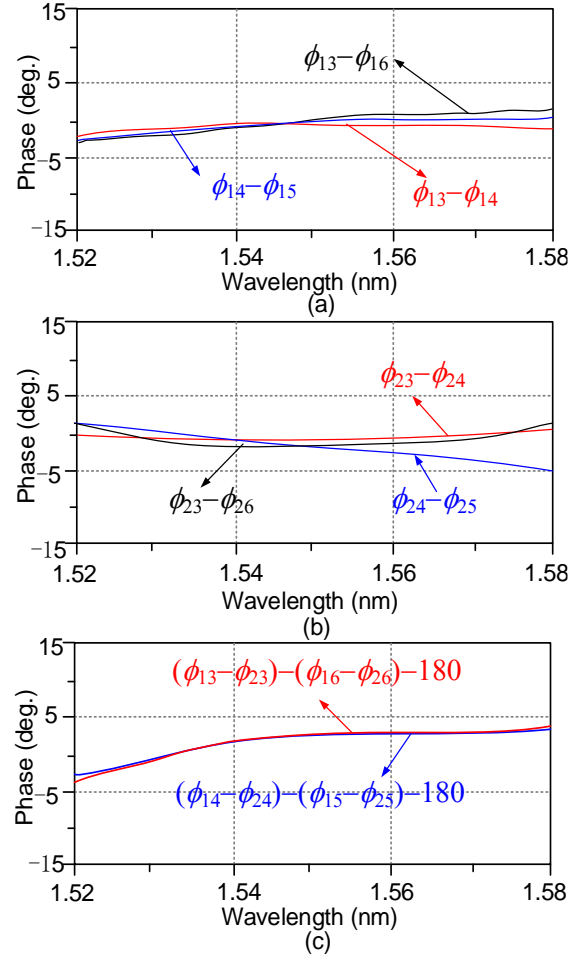


Fig. 4.9. Simulation of wavelength dependence of the proposed MMI. (a) Phase relationship between input port 1 and the four output ports and (b) phase relationship between input port 2 and the four output ports, (c) phase difference between output port 3 and output port 6 (red line) and phase difference between output port 4 and output port 5 (blue line).

The etching depth is $0.07 \mu\text{m}$. The length of this section MMI_L is $115.5 \mu\text{m}$, and the width of the MMI section (MMI_W) is $7.7 \mu\text{m}$. In addition, the width of the trenches (TR_W) is $3 \mu\text{m}$. The main parameters and the corresponding definitions and values are summarized in Table 4.2.

In the first step, I simulated the mode distribution of the MMI by FDTD, with results shown in Fig. 4.8. As can be seen, the input optical signals are distributed to the output ports. The optical phase relationship between the input and output ports of the MMI is the most important. Fig. 4.9 shows the simulated results of the optical phase relationship between the six ports of the proposed MMI as a function of the wavelength, in which ϕ_j represents the optical phase shift from input port In_ i and the output port Out_ j . Fig. 4.9(a) shows the results of $\phi_{13}-\phi_{14}$, $\phi_{13}-\phi_{16}$ and $\phi_{13}-\phi_{15}$. As can be seen, the phase difference is within ± 3 degree within the wavelength range of 1.52 to 1.58 μm (covering the entire C-band), which means that the optical signal injected from In_1 are nearly equally transmitted to the four output ports with nearly identical phase shift. Similar results can also be seen from Fig. 4.9(b), which shows the results of $\phi_{23}-\phi_{24}$, $\phi_{23}-\phi_{26}$ and $\phi_{23}-\phi_{25}$. The phase difference is lower than ± 3 degree as well. Furthermore, to demonstrate the phase difference between Out_3 and Out_6, $(\phi_{13}-\phi_{23})-(\phi_{16}-\phi_{26})-\pi$ is also simulated and given as the red line in Fig. 4.8(c). From 4.8(c), we can easily see that this phase difference is within ± 5 degree, showing that the optical phase difference between Out_3 and Out_6 is about 180 degree. Similarly, the optical phase difference between Out_4 and Out_5 (i.e., $(\phi_{14}-\phi_{24})-(\phi_{15}-\phi_{25})-\pi$) is also simulated and presented as the blue line in Fig. 4.9(c). Again, the phase difference is within ± 5 degree, which demonstrates again that Out_4 and Out_5 are out of phase.

Since the DFS value is obtained by measuring the frequency of the downconverted IF signal, the phase imbalance will have an ignorable impact on the DFS value (i.e., the velocity of the target) measurement. However, since the direction information is dependent on the phase information of the downconverted IF signal, the phase imbalance will influence the determination of the direction of the DFS. When considering a phase deviation of θ relative to 90 degree, the in-phase and quadrature outputs in Eq. (25) can be expressed as

$$\begin{bmatrix} i_I \\ i_Q \end{bmatrix} \propto \begin{bmatrix} \cos \Omega_d t \\ \sin (\Omega_d t + \theta) \end{bmatrix} = \begin{bmatrix} \cos \Omega_d t \\ \sin \Omega_d t \cos \theta - \cos \Omega_d t \sin \theta \end{bmatrix} \quad (26)$$

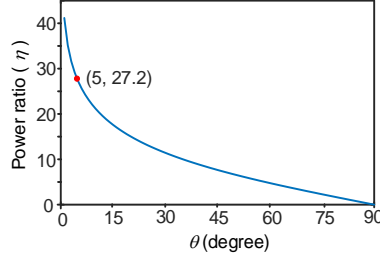


Fig. 4.10. Calculated power ratio between the positive and negative components of the complex signal versus the phase deviation θ .

Typically, in the digital signal processors of the real application systems, the in-phase and quadrature output signals are combined to form a complex signal, which is written as

$$\begin{aligned}
 i &= i_I + j i_Q & (27) \\
 &= \cos \Omega_d t + j (\sin \Omega_d t \cos \theta - \cos \Omega_d t \sin \theta) \\
 &= (1 + \sin \theta + \cos \theta) e^{j \Omega_d t} + (1 + \sin \theta - \cos \theta) e^{-j \Omega_d t}
 \end{aligned}$$

The phase comparison between the two IF signals can be made by comparing the power of the positive and negative frequency components. The power ratio is given by

$$\eta = 10 \log \left[\frac{(1 + \cos \theta)^2 + \sin^2 \theta}{(1 - \cos \theta)^2 + \sin^2 \theta} \right] \quad (28)$$

Fig. 4.10 shows the calculated relation between the power ratio and θ . Based on the simulated results in Fig. 4.9, we make θ equal to 5 degree, then the calculated power ratio is 27.2 dB, so the phase deviation introduced by the silicon coherent receiver has a little impact on the determination of DFS direction.

Since it is a passive component, no active tuning elements can be used to adjust the optical phase difference between the four output ports, the performance of the proposed optical hybrid is dependent on the fabrication quality of the MMI. Therefore, the fabrication tolerance of the MMI is analysed. Fig. 4.11 shows the optical phase different with different MMI lengths (MMI_L), MMI widths (MMI_W), etching depths (etch._dep) and

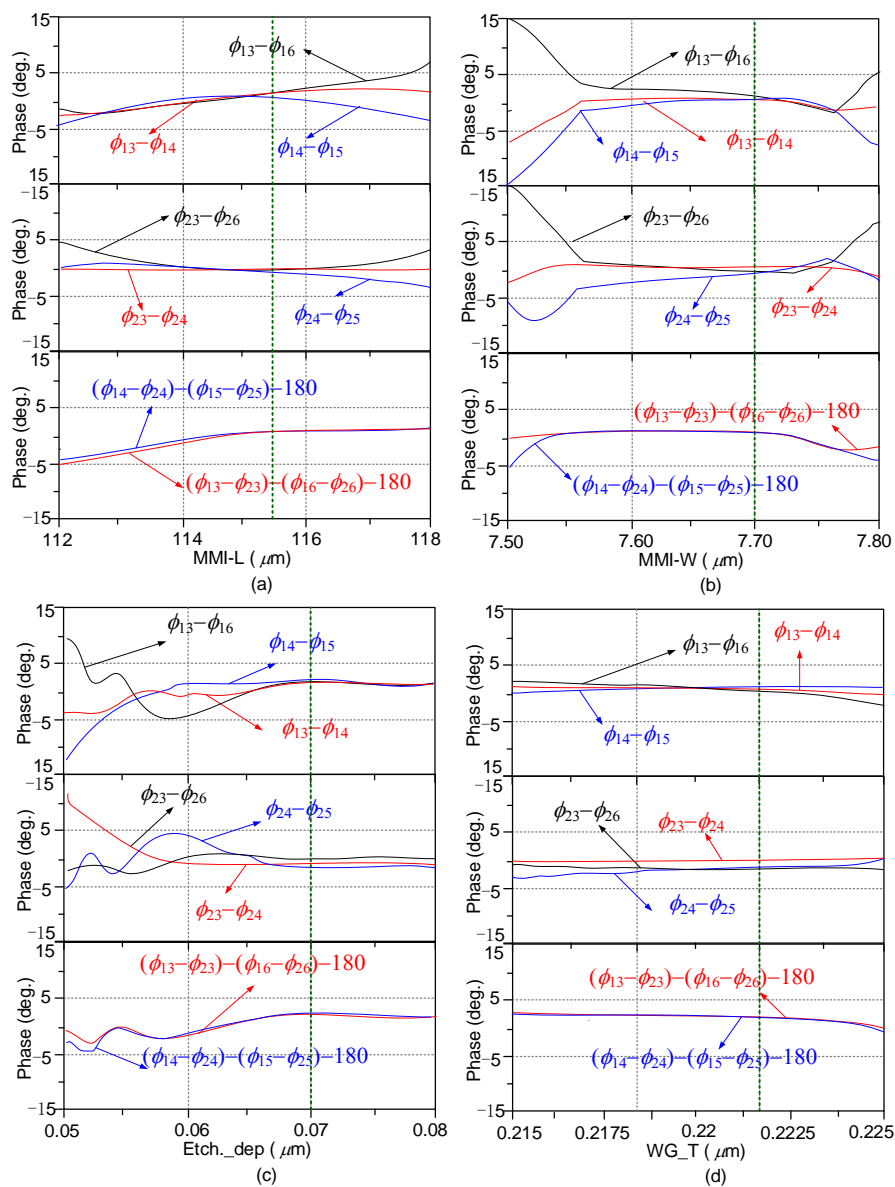


Fig. 4.11. Simulation of fabrication tolerance of the proposed MMI. Optical phase relationships as a function of (1) length of the MMI, (b) width of the MMI, (c) etching depth and (d) waveguide thickness. The wavelength of the injecting optical signal is 1550 nm. Green dashed line: the designed value.

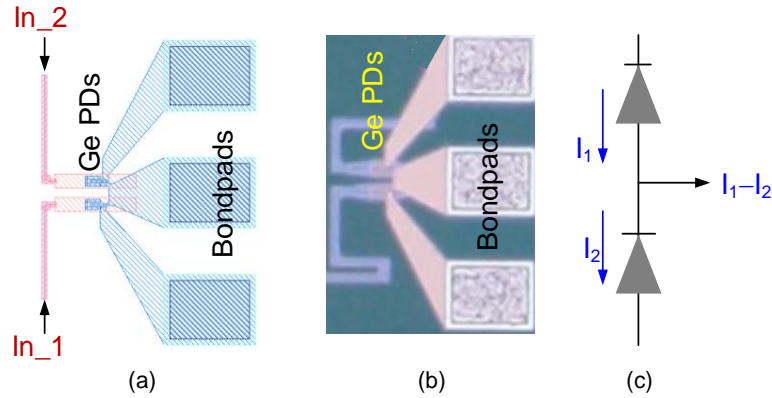


Fig. 4.12. Proposed BPD. (a) Layout, (b) picture and (c) electrical equivalent structure.

waveguide thickness (WG_T). The wavelength of the injected optical signal is $1.55 \mu\text{m}$ in the simulation. As can be seen from Fig. 4.10 (a), for a ± 10 nm variation of the MMI length, the optical phase error is lower than 5 degree. Fig. 4.11(b) shows that when the MMI width is within $7.7 \mu\text{m} \pm 10$ nm, the phase change is below 5 degree. Similarly, from the results presented in Fig. 4.11(c) and Fig. 4.11(d), we can see that for a ± 10 nm etching depth and ± 10 nm thickness fabrication tolerances, the optical phase error is still smaller than 5 degree. That is to say, although no active tuning is available on the proposed chip, the proposed 90-degree optical hybrid still presents good phase and amplitude imbalances, even if the fabrication tolerance is considered. More importantly, we can see from Fig. 4.9 that the phase imbalance is wavelength dependent. Therefore, the fabrication errors shown in Fig. 4.11 can be compensated by slightly shifting the wavelength of the optical carrier, when the integrated coherent receiver is applied into a photonic DFS measurement system.

According to the results shown in Fig. 4.9 and Fig. 4.11, Out_3 and Out_6 have a 180-degree optical phase difference, so balanced photodetection between these two output ports is reasonable. Similarly, another balanced photodetection can also be connected to Out_4 and Out_5, since these two ports are out-of-phase as well. In this thesis, the balanced photodetection is realized by direct photocurrent subtraction based on a pair of single-ended

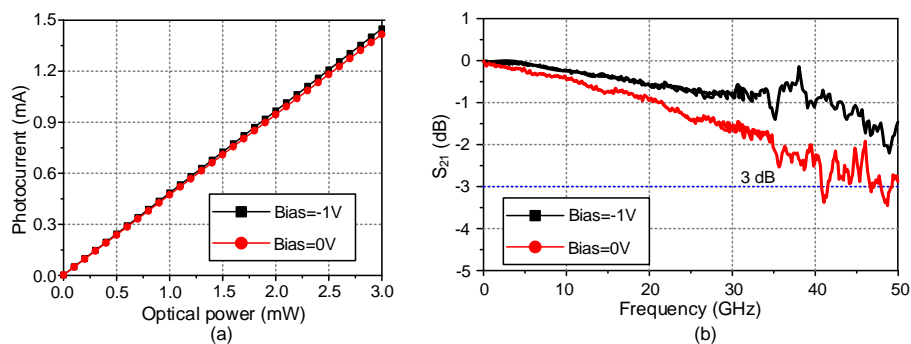


Fig. 4.13. Performances of the single-ended PD. (a) responsivities and (b) electrooptic modulation bandwidths with 0 V and -1 V bias voltage, respectively.

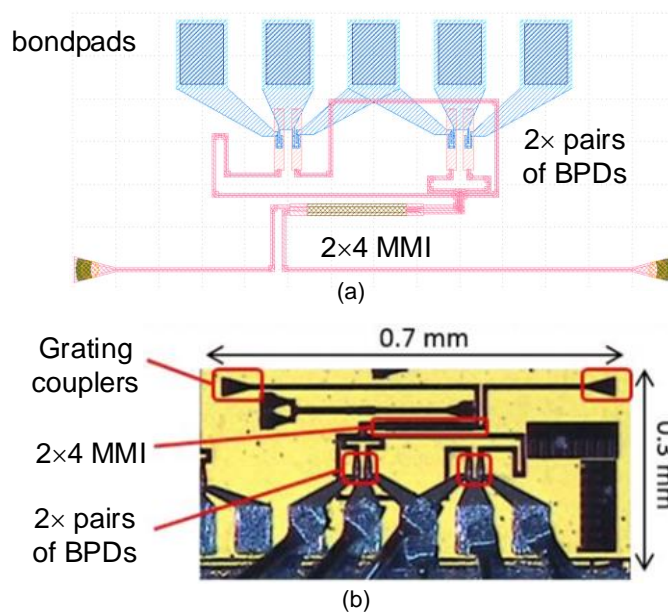


Fig. 4.14. The proposed silicon coherent receiver. (a) Layout and (b) microscope picture of the coherent receiver.

Ge PDs. Fig. 4.12 shows the layout and picture of the proposed BPD and the electrical equivalent structure. The single-ended PD comes from the PDK of the IMEC iSIPP25G platform. Firstly, the performance of the single-ended Ge PD is measured. Fig. 4.12(a) shows the measured responsivities of the Ge PD

Tab. 4.3. Comparison of state-of-the-art coherent receivers and the receiver used in this thesis

Ref	Date rate [Gbaud]	PDM	Integrated PDs	Footprint [mm ²]	Power consumption [mW/pol.]
This work	28	No	Yes	0.21 (0.3×0.7)	310
[48]	25	Yes	No	40(5×8)	NA
[49]	28	Yes	Yes	3.9(1.5×2.3)	900
[50]	28	Yes	Yes	4.76(1.4×3.4)	900
[51]	28	No	Yes	9.45(3.5×2.7)	514
[52]	25	No	Yes	3.0(2.0×1.5)	NA

when the bias voltages are 0 V and -1 V, respectively. The measured responsivity is about 0.47 A/W at 0 V bias and 0.48 A/W at -1 V bias. The measured dark current at -1 V bias is less than 15 nA. The electro-optic modulation response is also measured, and is depicted in Fig. 4.12 (b). Thanks to the low junction capacitance of the Ge PD, the measured 3-dB electro-optic bandwidth is larger than 50 GHz at -1 V bias, which is quite sufficient for most of the microwave systems.

Based on the single-ended Ge PD, a BPD is realized when the *ground* electrode of a single-ended PD and the *signal* electrode of another single-ended PD share the same bondpad, as shown in Fig. 4.13 (a) and 4.13(b). Through this kind of on-chip photocurrent subtraction, the number of the required bondpads can be reduced, so the footprint and cost of the device can thereby be reduced. Moreover, thanks to the uniformity of the Ge PD in this foundry platform [47], the performances of each PD are nearly identical, which ensures a high common mode rejection ratio (CMMR) of the BPD.

When the MMI-based 90-degree optical hybrid and two pair of BPDs are integrated on a single chip, an integrated coherent receiver is proposed, which is shown in Fig. 4.14. Fig. 4.14(a) shows the layout of the proposed coherent receiver. In Table 4.3, the comparison of the proposed and the state-of-the-art coherent receivers are provided. As can be seen, the coherent receiver used in this thesis has a low power consumption and small footprint. Two single-polarization grating couplers are used for coupling the two optical input signals to the chip. The single-end coupling loss of the grating coupler is measured to be 6.5 dB at a wavelength of 1.55 μm , and the 1-dB

bandwidth of the grating coupler is around 20 nm. A GSGSG RF probe is used to feed two DC bias voltages to the BPDs, and also lead the detected photocurrents out from the chip. It should be noted that, since additional waveguides are used to connect the MMI and the BPDs, to reduce the phase and amplitude imbalances between the output ports, the lengths of the waveguides should be identical.

4.3 Photonic Doppler frequency shift measurement based integrated coherent receiver

According to the principle in Section 4.1, by using the coherent optical receiver based on an MMI and BPDs described in Section 4.2, an ultra-compact DFS measurement system is proposed and demonstrated in this thesis. The schematic of the proposed DFS measurement system is shown in Fig. 4.15. A single-wavelength optical carrier is generated by a LD (Agilent N7714A) and split into two equal parts by a 50:50 optical splitter. Then the two optical signals are transmitted to two LiNbO₃ MZMs (MZM₁ and MZM₂) via two PCs (not shown in the figure). MZM₁ (Fujitsu FTM7938) has an analog RF bandwidth of 25 GHz with a half-wave voltage of 3.5 V. In the upper branch, a transmitted RF signal, generated by an analog signal generator (Keysight 8257D), is applied to the RF port of the MZM. Due to the electro-optic nonlinearity, several optical sidebands will be produced, and the even-order sidebands (together with the optical carrier) can be suppressed by adjusting the DC bias voltage to make the MZM bias at the minimum transmission point (MITP). Then, in order to avoid interference between the optical carriers from the two branches in the MMI-based 90-degree optical hybrid, an OBPF is inserted in this branch to select only one of the first-order sidebands (+1st-order sideband, for example). The OBPF (Yenista XTM-50) has a tunable center wavelength and a tunable bandwidth. The selected +1st-order sideband is amplified by an EDFA (Amonics Inc.) and coupled into the chip through In_1 port of the 90-degree optical hybrid as the *Signal* light. In the lower branch, MZM₂ (Fujitsu FTM7938) is driven by an echo signal, which is produced by another RF signal generator (Keysight N5183A). Also the DC bias voltage applied to MZM₂ is tuned to let it work at the MITP to remove the optical carrier and the even-order sidebands. The output signal of MZM₂

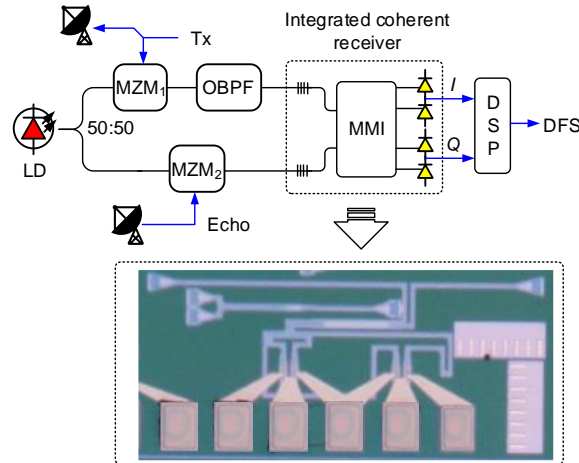


Fig. 4.15. Photonic DFS measurement system based on the integrated coherent receiver.

is coupled into the MMI through In₂ port via another grating coupler as the *Local* light, after being amplified by another EDFA (Amonics Inc.). In the integrated coherent receiver, the injection *Signal* light carrying the transmitted signal and the *Local* light carrying the echo information are optically mixed with each other in the MMI and output from the four outputs (i.e., Out₃ to Out₆). After the photodetection by the integrated BPDs, a pair of quadrature IF signals are generated. The output quadrature IF signals are sent to an electrical spectrum analyser (Keysight N9010A) to observe the electrical spectrum, and a 32 GHz, 80 GSa/s real time oscilloscope (Keysight DSO-X 92504A), which functions as an analog-to-digital converter (ADC) and a digital signal processor. The optical spectrum is observed by an optical spectrum analyser (YOKOGAWA AQ6370C) with a resolution of 0.02 nm.

Figure 4.16(a) shows the optical spectra measured from the upper branch. The wavelength of the optical carrier is 1541.24 nm and the optical power is 16 dBm. The frequency and power of the transmitted signal are 20 GHz and 10 dBm, respectively. The green and black lines represent the optical spectra before and after even-order sidebands suppression. As can be seen from the black line, by adjusting the DC bias applied to MZM₁, CS-DSB modulation with a carrier suppression ratio of 30 dB is achieved. The carrier suppression ratio is related to the extinction ratio of the MZM, which can be improved by

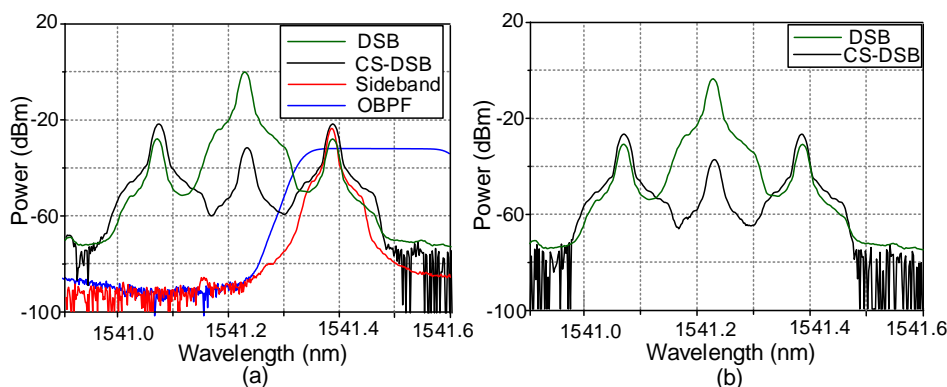


Fig. 4.16. Measured optical spectra of the proposed DFS system. Obtained from the (a) upper and (b) lower branch. DSB: double sideband; CS-DSB: carrier-suppressed double sideband; OBPF: optical bandpass filter.

employing an MZM with higher extinction ratio [48]. When the CS-DSB modulated optical signal goes through the OBPF with a frequency response shown as the blue line in Fig. 4.16(a), only the +1st-order sideband is selected, and the unwanted optical carrier and the -1st-order sideband are largely suppressed, as presented as the red line. Similar optical spectra are observed in the lower branch. In this branch, an echo signal with a frequency of 20.005 GHz (i.e., the DFS is +5 MHz). Due to the higher insertion loss of MZM₂, the optical power is slightly lower than that in the upper branch. It should be noted that, since the resolution of the optical spectrum analyser is 0.02 nm (~200 MHz), there is no significant wavelength difference between Fig. 4.16(a) and Fig. 4.16(b).

Fig. 4.17(a) shows the electrical spectrum obtained in this case. As can be seen, a 5-MHz IF signal is observed from the electrical spectrum, demonstrating that the DFS value is 5 MHz, which agrees well with the experimental setup. To identify the direction, the waveforms from the two BPDs are measured and presented in Fig. 4.17(b). Seen from the electrical waveforms, a pair of quadrature IF signals are obtained, showing a precise 90-degree optical phase difference between the output ports of the proposed MMI. Furthermore, the waveform obtained from the quadrature output ports is 90-degree advanced with respect to the waveform measured from the in-phase output ports, so the direction of the DFS is positive.

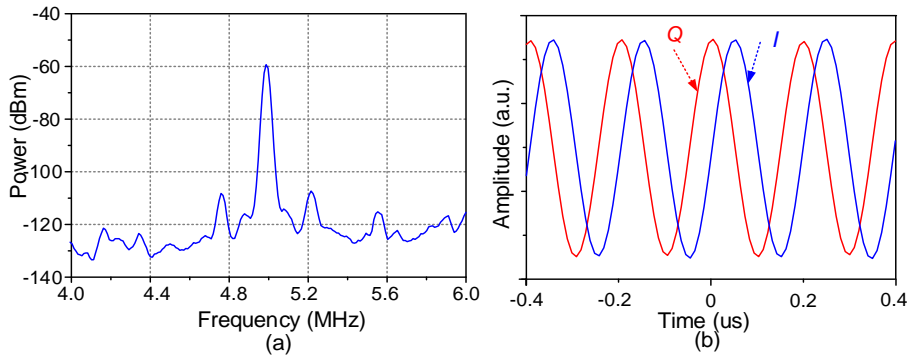


Fig. 4.17. Measured electrical spectrum and electrical waveform of the DFS when the transmitted frequency is 20 GHz and the echo frequency is 20.005 GHz. (a) electrical spectrum and (b) waveforms.

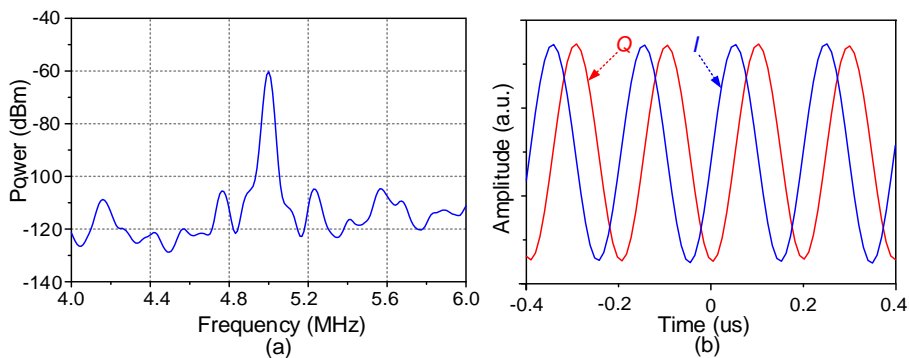


Fig. 4.18. Measured electrical spectrum and electrical waveform of the DFS when the transmitted frequency is 20 GHz and the echo frequency is 19.995 GHz. (a) electrical spectrum and (b) waveforms.

When the frequency of the echo signal is changed to be 19.995 GHz, the electrical spectrum of the IF signal is shown in Fig. 4.18(a). As can be seen, the frequency of the obtained IF signal is still 5 MHz. The corresponding electrical waveforms of the IF signals are presented in Fig. 4.18 (b). Under this condition, the two electrical waveforms are still quadrature. Furthermore, as compared with the waveforms shown in Fig. 4.17(b), the output signal from the quadrature output ports is delayed by 90 degree with respect to the IF signal from the in-phase output port, which means that the direction of the DFS is negative.

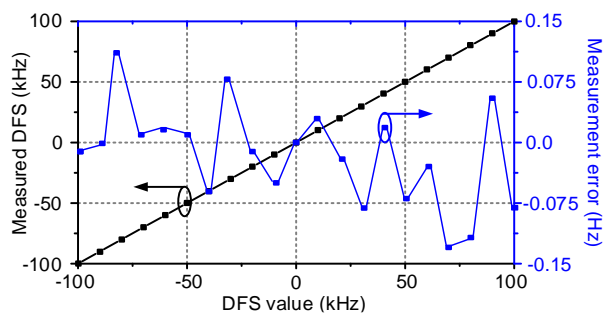


Fig. 4.19. Measured DFS and measurement error when the transmitted frequency is 20 GHz and the DFS is changed from -100 kHz to +100 kHz. Resolution bandwidth and video bandwidth of the electrical spectrum analyser are 1 Hz.

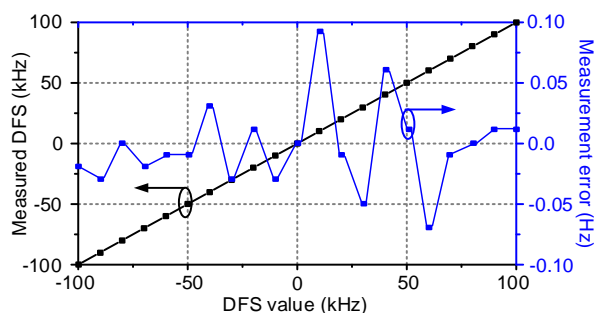


Fig. 4.20. Measured DFS and measurement error when the transmitted frequency is 10 GHz and the DFS is changed from -100 kHz to +100 kHz. Resolution bandwidth and video bandwidth of the electrical spectrum analyser are 1 Hz.

Then, the echo signal frequency is changed from 20 GHz–100 kHz to 20 GHz+100 kHz (i.e., the DFS is set to be –100 kHz to +100 kHz), with a step of 10 KHz. The DFS measured by the proposed coherent receiver and the measurement error are depicted in Fig. 4.19. When the resolution bandwidth (RBW) and the video bandwidth (VBW) of the electrical spectrum analyser is set to be 1 Hz, the measurement error is lower than ± 0.15 Hz.

The proposed DFS measurement system can be operated within a wide frequency range. Since the 90-degree optical hybrid and the BPDs in the proposed coherent receiver have wide bandwidth, the bandwidth of the proposed DFS measurement system is mainly determined by the other

Tab. 4.4. Performances comparison between the proposed and state-of-the-art DFS measurement systems

Ref	Bandwidth [GHz]	Error [Hz]	Direction identification	Integration
This work	10-40	0.15	Y	Y
[13]	0-40	1.61%	N	N
[14]	0-40	4.3%	N	N
[16]	10-30	5×10^{-10}	Y	N
[17]	10-20	60	Y	N
[18]	10-18	1	Y	N
[19]	10-18	5×10^{-6}	Y	N
[20]	10-39	5×10^{-6}	Y	N
[21]	5-40	12	Y	N
[22]	10-38	5.8	Y	N

electro-optic devices. Commercially-available MZMs can easily support electro-optic modulation up to 40 GHz or higher, so the upper limit of the operational frequency range of the proposed DFS measurement system, which is restricted by the bandwidth of the MZM, can be higher than 40 GHz. On the other hand, the lower limit is dependent on the roll-off factor of the optical filter. To eliminate the interference between the lower and upper branches, the optical carrier in one branch should be largely suppressed. In our experiment, the roll-off factor of the optical filter is 500 dB/nm. The optical carrier can be effectively suppressed when the transmitted frequency is larger than 10 GHz, so the lower limit is about 10 GHz. To demonstrate this property, a DFS measurement with the frequency of the transmitted signal changed to be 10 GHz is also carried out and shown in Fig. 4.20. As can be seen from Fig. 4.20, the measurement error is lower than ± 0.1 Hz, when the RBW and VBW are set to be 1 Hz as well.

4.4 Conclusion

In this chapter, a microwave DFS measurement system based on an integrated silicon optical coherent receiver is proposed and experimentally demonstrated. First, the principles of different photonic DFS measurement methods were summarized. Then, the proposed coherent receiver was

explained in detail. The main modules of the optical coherent receiver, i.e., the 90-degree optical hybrid and the BPD, were introduced and characterized. The 90-degree optical hybrid was realized by a six-port MMI and the BPD is achieved by on-chip subtraction of photocurrent by a pair of SiGe PDs. Finally, a photonic DFS measurement system based on the proposed optical coherent receiver was demonstrated. With the proposed DFS measurement system, a DFS measurement within the frequency range of 10~40 GHz with a measurement error of lower than ± 0.15 Hz were carried out. More importantly, thanks to the quadrature frequency mixing realized by the 90-degree optical hybrid, the direction of the DFS can also be acquired. As can be seen from the performances comparison between the proposed and the state-of-the-art photonic DFS measurement systems, shown in Tab. 4.4, the thesis presents a wideband, relatively low error, and more importantly, a silicon-photonics-based DFS measurement system. Future work may be focused on the co-integration with silicon modulators and other devices or the application of systems based on the photonic DFS measurement. For example, the silicon ring modulator used in Chapter 2 and Chapter 3 or SiGe electroabsorption modulators can be co-integrated with the silicon coherent receiver to increase the operating bandwidth to more than 50 GHz. In addition, an optical filter is required in one of the branches to suppress the optical carrier to avoid the interference between the two branches. Although an optical bandpass filter is used in the experiment, a band-stop optical filter is actually needed, so such kind of optical filter can be easily realized by a silicon all-pass ring resonator with high extinction ratio and narrow bandwidth.

Reference

- [1] Z. Tang, J. Zhang, Z. Q. He, S. Pan, G. Roelkens, D. Van Thourhout, "Photonic Doppler Frequency Shift Measurement Enabled by an Integrated Photonic Six-Port Receiver," *IEEE Transactions on Instrumentation and Measurement*, under preparation.
- [2] W. Kuang and A. S. Morris, "Using Short-Time Fourier transform and Wavelet Packet Filter Banks for Improved Frequency Measurement in A

- Doppler Robot Tracking System," *IEEE Transactions on Instrumentation and Measurement*, vol. 51, no. 3, pp. 440-444, 2002.
- [3] V. C. Chen, F. Li, S. Ho and H. Wechsler, "Micro-Doppler Effect in Radar: Phenomenon, Model, and Simulation Study," *IEEE Transactions on Aerospace and Electronic Systems*, vol. 42, no. 1, pp. 2-21, 2006.
- [4] Y. Zhao and Y. Su, "Cyclostationary Phase Analysis on Micro-Doppler Parameters for Radar-Based Small UAVs Detection," *IEEE Transactions on Instrumentation and Measurement*, vol. 67, no. 9, pp. 2048-2057, Sep. 2018.
- [5] F. Xiao, F. M. Ghannouchi, T. Yakabe, "Application of a Six-Port Wave-Correlator for a Very Low Velocity Measurement Using the Doppler Effect," *IEEE Transactions on Instrumentation and Measurement*, vol. 52, no. 2, pp. 297-301, Apr. 2003.
- [6] Z. T. Gu, et al., "Blind Separation of Doppler Human Gesture Signals Based on Continuous-Wave Radar Sensors," *IEEE Transactions on Instrumentation and Measurement*, vol. 68, no. 7, pp. 2659-2661, Jul. 2019.
- [7] T. Fan et al., "Wireless Hand Gesture Recognition Based on Continuous-Wave Doppler Radar Sensors," *IEEE Transaction on Microwave Theory and Techniques*, vol. 64, no. 11, pp. 4012-4020, Nov. 2016.
- [8] C.-M. Yu, J. E. Sanderson, T. H. Marwick, and J. K. Oh, "Tissue Doppler Imaging: A New Prognosticator for Cardiovascular Diseases," *Journal of the American College of Cardiology*, vol. 49, no. 19, pp. 1903-1914, 2007.
- [9] S. Shinohara, A. Mochizuki, H. Yoshida, and M. Sumi, "Laser Doppler Velocimeter Using the Self-Mixing Effect of a Semiconductor Laser Diode," *Applied Optics*, vol. 25, no. 9, pp. 1417-1419, 1986.
- [10] P. B. Hays, V. J. Abreu, M. E. Dobbs, D. A. Gell, H. J. Grassl, and W. R. Skinner, "The High - Resolution Doppler Imager on the Upper Atmosphere Research Satellite," *Journal of Geophysical Research: Atmospheres*, vol. 98, no. D6, pp. 10713-10723, 1993.
- [11] S. L. Pan, J. P. Yao, "Photonics-Based Broadband Microwave Measurement," *IEEE/OSA Journal of Lightwave Technology*, vol. 35, no. 16, pp. 3498-3513, 2017.
- [12] X. Zou, B. Lu, W. Pan, L. Yan, A. Stöhr, and J. Yao, "Photonics for Microwave Measurements," *Laser & Photonics Reviews*, vol. 10, no. 5, pp. 711-734, 2016.

-
- [13] H. Emami, M. Hajihashemi, and S. E. Alavi, "Standalone Microwave Photonics Doppler Shift Estimation System," *Journal of Lightwave Technology*, vol. 34, no. 15, pp. 3596-3602, 2016.
- [14] H. Emami, M. Hajihashemi, S. E. Alavi and M. Ghanbarisabagh, "Simultaneous Echo Power and Doppler Frequency Measurement System Based on Microwave Photonics Technology," *IEEE Transactions on Instrumentation and Measurement*, vol. 66, no. 3, pp. 508-513, Mar. 2017.
- [15] G. K. Gopalakrishnan, W. K. Burns, and C. H. Bulmer, "Microwave-Optical Mixing in LiNbO₃ Modulators," *IEEE Transactions on Microwave Theory and Techniques*, vol. 41, no. 12, pp. 2383-2391, 1993.
- [16] X. Zou, W. Li, B. Lu, W. Pan, L. Yan and L. Shao "Photonic Approach to Wide-Frequency-Range High-Resolution Microwave/Millimeter-Wave Doppler Frequency Shift Estimation," *IEEE Transaction on Microwave Theory and Techniques* vol. 63 no. 4 pp. 1421-1430, 2015.
- [17] B. Lu, W. Pan, X. Zou, X. Yan, L. Yan, and B. Luo, "Wideband Doppler Frequency Shift Measurement and Direction Ambiguity Resolution Using Optical Frequency Shift and Optical Heterodyning," *Optics Letters*, vol. 40, no. 10, pp. 2321-2324, 2015.
- [18] L. Xu, Y. Yu, H. Tang and X. Zhang, "A Simplified Photonic Approach to Measuring the Microwave Doppler Frequency Shift," *IEEE Photonics Technology Letters*, vol. 30, no. 3, pp. 246-249, 2018.
- [19] X. Li, A. Wen, W. Chen, Y. Gao, S. Xiang, H. Zhang, and X. Ma, "Photonic Doppler Frequency Shift Measurement Based on a Dual-Polarization Modulator," *Applied Optics*, vol. 56, no. 8, pp. 2084-2089, 2017.
- [20] W. Chen, A. Wen, X. Li, Y. Gao, Y. Wang, S. Xiang, H. He, and H. Zheng, "Wideband Doppler Frequency Shift Measurement and Direction Discrimination based on a DPMZM," *IEEE Photonics Journal*, vol. 9, no. 2, 2017.
- [21] F. Z. Zhang, J. Z. Shi, and S. L. Pan, "Photonics-Based Wideband Doppler Frequency Shift Measurement by In-Phase and Quadrature Detection," *Electronic Letters*, vol. 54, no. 11, pp. 708-710, 2018.
- [22] B. Lu, W. Pan, X. Zou, Y. Pan, X. Liu, L. Yan, and B. Luo, "Wideband Microwave Doppler Frequency Shift Measurement and Direction Discrimination Using Photonic I/Q Detection," *IEEE/OSA Journal of Lightwave Technology*, vol. 34, no. 20, pp. 4639-4645, Oct. 2016.

- [23] S. Pan and Y. Zhang, "Tunable and Wideband Microwave Photonic Phase Shifter Based on a Single-Sideband Polarization Modulator and a Polarizer," *Optics Letters*, vol. 37, no. 21, pp. 4483-4485, 2012.
- [24] R. B. Garreis, "90 degree optical hybrid for coherent receivers," in *Optical Space Communication II*, 1991, vol. 1522, pp. 210-219: International Society for Optics and Photonics.
- [25] Kylia. COH28. <http://kylia.com/kylia/?portfolio=90-hybrid-coh>.
- [26] Krytar. 90-degree hybrid coupler 3017360K[online]. <https://krytar.com/products/hybridcouplers/3-db-90-degree-hybrid-couplers/>.
- [27] Krytar. 90-degree hybrid coupler 310040K[online]. <https://krytar.com/products/hybrid-couplers/3-db-90-degree-hybrid-couplers/3100400K-90-deg-hybrid-coupler/>.
- [28] M. Pagani, D. Marpaung, D.-Y. Choi, S. J. Madden, B. Luther-Davies, and B. J. Eggleton, "Tunable wideband microwave photonic phase shifter using on-chip stimulated Brillouin scattering," *Optics Express*, vol. 22, no. 23, pp. 28810-28818, 2014.
- [29] A. Loayssa and F. J. Lahoz, "Broad-band RF photonic phase shifter based on stimulated Brillouin scattering and single-sideband modulation," *IEEE Photonics Technology Letters*, vol. 18, no. 1, pp. 208-210, 2005.
- [30] T. Okoshi, "Recent Advances in Coherent Optical Fiber Communication Systems," *Journal of Lightwave Technology*, vol. 5, no. 1, pp. 44-52, 1987.
- [31] Y. Sakamaki, H. Yamazaki, T. Mizuno, T. Goh, Y. Nasu, T. Hashimoto, S. Kamei, K. Hattori, and H. Takahashi, "One-chip integrated dual polarization optical hybrid using silica-based planar lightwave circuit technology," in *IEEE European Conference and Exhibition on Optical Communication*, pp. 1-2, 2009.
- [32] Y. Sakamaki, T. Kawai, T. Komukai, M. Fukutoku, T. Kataoka, T. Watanabe, and Y. Ishii, "Experimental Demonstration of Multi-Degree Colorless, Directionless, Contentionless ROADM for 127-Gbit/s PDM-QPSK Transmission System," *Optics Express*, vol. 19, no. 26, pp. B1-B11, 2011.
- [33] D. Hoffman, H. Heidrich, G. Wenke, R. Langenhorst, and E. Dietrich, "Integrated Optics Eight-Port 90° Hybrid on LiNbO₃," *Journal of Lightwave Technology*, vol. 7, no. 5, pp. 794-798, 1989.

-
- [34] S. Faralli, G. Meloni, F. Gambini, J. Klamkin, L. Potì, and G. Contestabile, "A Compact Silicon Coherent Receiver Without Waveguide Crossing," *IEEE Photonics Journal*, vol. 7, no. 4, pp. 1–6, 2015.
- [35] F. Gambini, G. Meloni, S. Faralli, G. Contestabile, L. Potì, and J. Klamkin, "Ultra-compact 56-Gb/s QPSK and 80-Gb/s 16-QAM Silicon Coherent Receiver Free of Waveguide Crossings," in *Proceedings of IEEE Conference on Group IV Photonics*, pp. 149–150, 2014.
- [36] M. Seimetz and C. M. Weinert, "Options, Feasibility and Availability of 2×4 90° Hybrids for Coherent Optical Systems," *Journal of Lightwave Technology*, vol. 24, no. 3, pp. 1317–1322, 2006.
- [37] Y. C. Heish, "Free-Space Optical Hybrid," United States Patent, Patent No. US7,573,641 B2.
- [38] Optoplex, 90-degree optical hybrid, http://www.optoplex.com/Optical_Hybrid.htm
- [39] E. C. M. Pennings, R. J. Deri, R. Bhat, T. R. Hayes, and N. C. Andreadakis, "Ultracompact, All-Passive Optical 90° Hybrid on InP Using Self-Imaging," *IEEE Photonics Technology Letters*, vol. 5, no. 6, pp. 701–703, 1993.
- [40] P. Runge, S. Schubert, A. Seeger, K. Janiak, J. Stephan, D. Trommer, P. Domburg, and M. L. Nielsen, "Monolithic InP Receiver Chip with a 90° Hybrid and 56 GHz Balanced Photodiodes," *Optics Express*, vol. 20, no. 26, pp. B250–B255, 2012.
- [41] C. Doerr, L. Zhang, P. Winzer, N. Weimann, V. Houtsma, T.-C. Hu, N. Sauer, L. Buhl, D. Neilson, and S. Chandrasekhar, "Monolithic InP Dual-Polarization and Dual-Quadrature Coherent Receiver," *IEEE Photonics Technology Letters*, vol. 23, no. 11, pp. 694–696, 2011.
- [42] K. Voigt, L. Zimmermann, G. Winzer, H. Tian, B. Tillack, and K. Petermann, "C-band Optical 90° Hybrids in Silicon Nanowaveguide Technology," *IEEE Photonics Technology Letters*, vol. 23, no. 23, pp. 1769–1771, 2011.
- [43] W. Yang, M. Yin, Y. Li, X. Wang, and Z. Wang, "Ultra-Compact Optical 90° Hybrid Based On A Wedge-Shaped 2×4 MMI Coupler and a 2×2 MMI Coupler in Silicon-on-Insulator," *Optics Express*, vol. 21, no. 23, pp. 28423–28431, 2013.

- [44] R. Halir, G. Roelkens, A. Ortega-Moñux, and J. G. Wangüemert-Pérez, "High-Performance 90° Hybrid based on a Silicon-on-Insulator Multimode Interference Coupler," *Optics Letters*, vol. 36, no. 2, pp. 178–180, 2011.
- [45] J. Zhang, J. Verbist, B. Moeneclaey, J. Van Weerdenburg, R. Van Uden, H. Chen, J. Van Campenhout, C. Okonkwo, X. Yin, and J. Bauwelinck, "Compact Low-Power-Consumption 28-Gbaud QPSK/16-QAM Integrated Silicon Photonic/Electronic Coherent Receiver," *IEEE Photonics Journal*, vol. 8, no. 1, pp. 1-10, 2016.
- [46] P. Absil et al., "Silicon photonic integrated circuits: A Manufacturing Platform for High Density, Low Power Optical I/O's," *Optics Express*, vol. 23, no. 7, pp. 9369–9378, 2015.
- [47] Y. Ogiso, Y. Tsuchiya, S. Shinada, S. Nakajima, T. Kawanishi, and H. Nakajima, "High Extinction-Ratio Integrated Mach-Zehnder Modulator with Active Y-Branch for Optical SSB Signal Generation," *IEEE Photonics Technology Letters*, vol. 22, no. 12, pp. 941-943, 2010.
- [48] M. Takahashi et al., "Compact 100-Gb/s DP-QPSK intradyne coherent receiver module employing Si waveguide," presented at the *Eur. Conf. Opt. Commun.*, Valencia, Spain, 2015, Paper Tu. 1.3.1.
- [49] P. Dong et al., "Monolithic silicon photonic integrated circuits for compact 100+Gb/s coherent optical receivers and transmitters," *IEEE J. Sel. Topics Quantum Electron.*, vol. 20, no. 4, Jul./Aug. 2014, Art. ID 6100108.
- [50] C. Doerr et al., "Packaged monolithic silicon 112 Gb/s coherent receiver," *IEEE Photon. Technol. Lett.*, vol. 23, no. 12, pp. 762–764, Jun. 2011.
- [51] G. Winzer et al., "Monolithic photonic-electronic QPSK receiver for 28 Gbaud," presented at the *Opt. Fiber Commun. Conf.*, Los Angeles, CA, USA, 2015, Paper M3C.4.
- [52] M. N. Sakib, M. S. Hai, and O. Liboiron-Ladouceur, "A silicon photonic integrated packaged coherent receiver frontend for soft-decision decoding," *J. Lightw. Technol.*, vol. 32, no. 24, pp. 4753–4758, Dec. 15, 2014.

Chapter 5

Conclusions and perspectives

5.1 Overview

THIS work aimed to realize MWP systems based on silicon building blocks. One of the main motivations is the application of a silicon ring modulator in RoF wireless communication systems. Firstly, a single ring modulator is employed to build a full-duplex RoF system with local SSB modulation and remote carrier reuse. This is based on the special property that the ring modulator can only perform strong electro-optic modulation when the wavelength of the injected optical carrier is around the resonant wavelength of the ring resonator. Thus, in our work, a dual-wavelength laser source, with one of the optical carriers aligned to the resonant wavelength, is used in the CO. When the dual-wavelength laser source goes through the ring modulator, the data applied to the ring modulator will only be imprinted to one of the optical carriers, and then a SSB-modulated downstream signal is obtained, which can combat the power fading introduced by the fiber dispersion. In the RRH, the unmodulated carrier in the SSB-modulated optical downstream signal is filtered out and reused as the optical carrier for the upstream link, which avoid the need of laser sources and the necessary drivers and temperature controllers in the RRH. Based on this idea, a 20-GHz downstream link and a 10-GHz upstream link are experimentally demonstrated. This work demonstrates the feasibility of using the ring modulator into an analog wireless communication system.

Then, an O-band III-V PD is co-integrated with the C-band silicon ring modulator to build a III-V-on-silicon transceiver to fulfil the task of both electro-optic modulation for the downstream link and photodetection for the upstream link by a single integrated chip. Transfer printing technology is

employed to realize the III-V-on-silicon integration. Since the PD is designed to have a cut-off wavelength of 1310 nm, it is directly placed on top of the grating coupler without influencing the C-band downstream data, which reduces the footprint and also enables bidirectional transmission of the C-band downstream and O-band upstream signals in a single fiber. Since the ring modulator has a bandwidth of 15 GHz at -1 V bias and the transfer-printed PD has a bandwidth of 11.5 GHz at -3 V bias, an X-band BiDi RoF system is demonstrated. This work shows the advantage of transfer printing for the III-V-on-silicon circuits integration, which presents a new solution for the integration of not only III-V-on-silicon transceiver but also other devices on other material platforms for the RoF systems of the future.

In addition to the ring modulator, an integrated silicon coherent receiver was also introduced for microwave photonic applications. The coherent receiver contains an MMI-based six-port 90-degree optical hybrid and a pair of SiGe BPDs. Based on the integrated silicon coherent receiver, a photonic DFS measurement system was proposed. In the DFS measurement system, an optical carrier is split into two paths and modulated by a transmitted signal and an echo signal, respectively. An optical filter is inserted in one path to select the $+1^{\text{st}}$ order sidebands. The optical signals from the two branches are sent to the 90-degree hybrid as the *signal* light and *LO* light, and then a pair of IF outputs with quadrature phase difference are obtained. By measuring the frequency of the IF signal, the DFS value is obtained. More importantly, by comparing the phase difference between the IF signals, the direction of the DFS can also be acquired. In our work, a DFS measurement system with an operational frequency range of 10-40 GHz and a measurement error of lower than ± 0.15 Hz is achieved.

5.2 Perspectives

As described in the Introduction, both the domain of MWP and silicon photonics are far richer in content than the work presented in this thesis, so a lot of things can be done in the future.

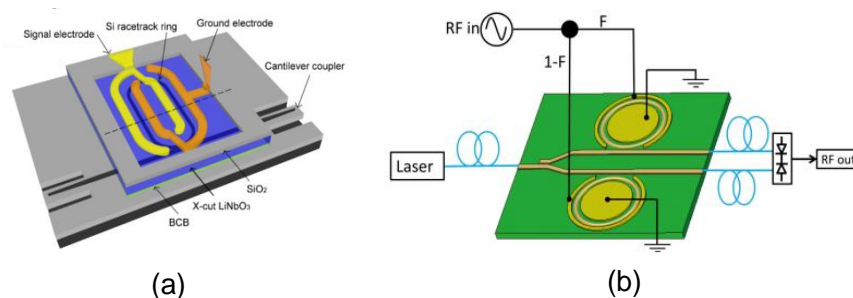


Fig. 5.1. Linearized ring modulator. (a) Si/LiNbO₃ modulator (figure from [2]) and (b) dual-ring modulator (figure from [3]).

In this thesis, we presented MWP systems based on a silicon ring modulator, which was originally developed for digital systems. However, in an analog system, the linearity of the system, typically characterized as the SFDR of the system, needs more attention. According to the measurement result shown in Chapter 3, the SFDR of a system based on a silicon ring modulator is not comparable with that based on a LiNbO₃ MZM. Therefore, future work can focus on the nonlinear distortion analysis [1] and linearity improvement [2-4] of the silicon ring modulator. Some solutions were previously reported. For example, in [2], a highly linear ring modulator based on hybrid integration of silicon and lithium niobite was proposed, as shown in Fig. 5.1(a). An *x*-cut LiNbO₃ thin film was bonded to a silicon ring modulator via BCB. The nonlinearity employed for the electro-optic modulation is based on the $\chi^{(2)}$ effect of LiNbO₃, rather than the plasma dispersion effect in the PN-doped silicon ring modulator, so the linearity can be increased. Ref. [3] gives another solution, with two ring modulators in an MZI, as presented in Fig. 5.1(b). Since the MZI has a sinusoidal response with a negative third-order derivative and the ring modulator has a positive third-order derivative, the entire third-order distortions can be eliminated when properly adjusting the coupling efficiency between the MZI and the ring modulator, which leads to an improvement of the linearity.

In addition to improving the linearity of the ring modulator, the stability of the ring modulator is another important issue that can be studied future. It is well known that the ring modulator is temperature-dependent, which means that the resonant wavelength will shift when the temperature changes.

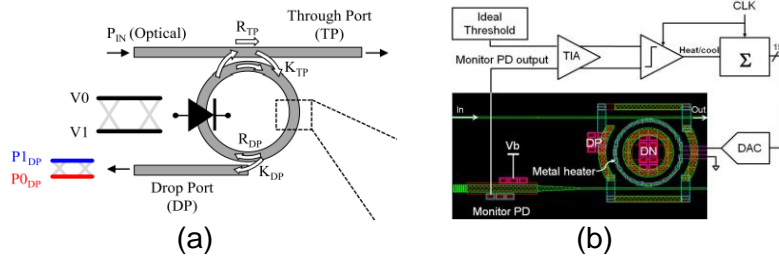


Fig. 5.2. Wavelength-locking of the ring modulator. Based on (a) drop-port optical modulation amplitude monitoring (figure from [5]) and (b) optical average power monitoring with co-integrated Ge PD (figure from [6]).

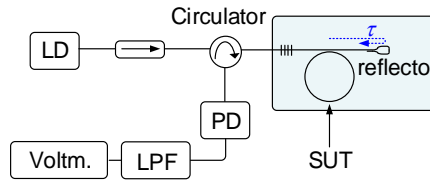


Fig. 5.3. Instantaneous frequency measurement system based on a silicon ring modulator and a reflector.

Since the modulation efficiency is related to the wavelength of the resonant wavelength, as presented in Chapter 2 and Chapter 3, wavelength-locking of the silicon ring modulator is highly desirable [5, 6]. Fig. 5.2 shows two examples. In Fig. 5.2(a), an optical modulation amplitude (OAM) measurement was applied to the drop-port of the ring modulator, which can reflect the wavelength drift. Then, a feed-back loop was constructed according to the strength of the OAM [5]. In Fig. 5.2(b), a Ge-based monitor PD was integrated in the drop port of the ring modulator to measure the mean power of the modulated signal. The obtained value was used to build a closed loop to align and lock the ring modulator [6].

Besides, in this thesis, the full-duplex SSB-based RoF system only uses the property that the modulation efficiency is dependent on the wavelength of the optical carrier sent into the ring modulator. Actually, the ring modulator also has other distinct features compared to the conventional traveling-wave (TW)-electrodes-based MZM, which can also be applied to other MWP systems. For example, since the ring modulator does not have the velocity mismatch problem that usually exists in a TW-based MZM, it can realize

bidirectional electro-optic modulation. Exploiting this property, a microwave photonic instantaneous frequency measurement (IFM) system can be realized, as shown in Fig. 5.3. An optical carrier is sent to the ring modulator and modulated by a signal-under-test (SUT). If the angular frequency of the optical carrier and the SUT are ω_c and ω_{SUT} , respectively, the modulated optical signal can be expressed as

$$E_1 = \cos(\omega_c t + \beta \cos \omega_{\text{SUT}} t) \quad (1)$$

where β is the modulation index. Then, the modulated optical RF signal is reflected by an optical reflector. If the optical time delay is τ when the optical signal is transmitted from and returned back to the ring modulator, the delayed optical signal can be written as

$$E_2 = \cos[\omega_c (t - \tau) + \beta \cos \omega_{\text{SUT}} (t - \tau)] \quad (2)$$

The reflected optical signal is re-injected into the ring modulator and re-modulated by the SUT again, so the optical signal after bidirectional modulation is given by

$$E_3 = \cos[\omega_c (t - \tau) + \beta \cos \omega_{\text{SUT}} (t - \tau) + \beta \cos \omega_{\text{SUT}} t] \quad (3)$$

When the optical signal goes through an optical circulator and is sent to a PD, the obtained electrical signal can be calculated as

$$i \propto [\cos \omega_{\text{SUT}} (t - \tau) + \cos \omega_{\text{SUT}} t]^2 \quad (4)$$

An electrical low pass filter (LPF) then follows to extract the DC component, which gives

$$V_{\text{DC}} \propto 1 + \cos \omega_{\text{SUT}} \tau \quad (5)$$

As can be seen from Eq. (5), since the time delay is fixed, the obtained DC voltage is totally determined by the frequency of the SUT. Therefore, by measuring the DC voltage, photonic IFM can be realized. The reflector in Fig. 5.3(a) can be realized on chip via an waveguide Bragg grating [7] or Sagnac loop mirror [8].

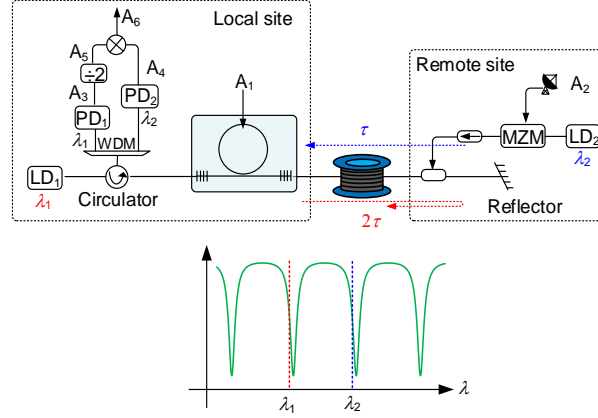


Fig. 5.4. Phase-stable RF signal transmission based on a silicon ring modulator.

Another potential application is phase stable signal transmission, which is of importance for distributed RF systems, such as distributed radar systems for defence applications, distributed antenna system (DAS) for wireless communication or radio astronomy systems for deep-space detection [9, 10]. Based on the silicon ring modulator, a phase stable signal transmission can be realized, as presented in Fig. 5.4. In the local site, an LD (LD₁) produces an optical carrier (λ_1) with a wavelength aligned to one of the resonant wavelengths and sent to the ring modulator. A local RF signal (denoted as A_1) is applied to the ring modulator, which is expressed as

$$A_1 = \cos(\omega_l t + \phi_l) \quad (6)$$

where ω and ϕ are the angular frequency and phase of the local signal. The modulated signal is transmitted to the remote side via a certain length of fiber. In the remote side, the optical signal is reflected by an optical reflector and combined with another optical signal carrying the received RF signal that need to be transmitted to the local site (A_2). It should be noted that the received RF signal is modulated onto another optical carrier (λ_2) with a wavelength aligned to the different resonant wavelength of the ring modulator. If the frequency of the received RF signal is ω_r , we have

$$A_2 = \cos(\omega_r t + \phi_r) \quad (7)$$

where φ is the phase. When the combined optical signal is transmitted back to the local site through the same optical fiber, the optical signals at different wavelength will be remodulated by the local signal again. Through this kind of bidirectional modulation, photonic microwave mixing is applied to both the reflected local signal and the received RF signal from the remote site. Then, the remodulated signal is separated by a WDM and sent to two different PDs (PD₁ for the local link and PD₂ for the remote link, respectively).

If the time delay introduced by the fiber link is τ , for the local signal A_1 , since it travels a round trip, the time delay is 2τ , the output electrical signal of PD₁ can be written as

$$\begin{aligned} A_3 &= \cos(\omega_l t + \varphi_l) \cdot \cos(\omega_l t - 2\omega_l \tau + \varphi_l) \\ &\propto \cos(2\omega_l t - 2\omega_l \tau + 2\varphi_l) + \dots \end{aligned} \quad (8)$$

While for the received RF signal, it undergoes one-way trip, so the time delay is τ , thus the electrical signal outputs from PD₂ is given by

$$\begin{aligned} A_4 &= \cos(\omega_l t + \varphi_l) \cdot \cos(\omega_r t - \omega_r \tau + \varphi_r) \\ &\propto \cos[(\omega_l + \omega_r)t - \omega_r \tau + \varphi_l + \varphi_r] + \dots \end{aligned} \quad (9)$$

It should be noted that in Eq. (8) and Eq. (9), only the sum-frequency components are taken into account, which can be realized by using two electrical bandpass filters (not shown in the figure). If an 1/2 frequency divider is used after PD₁, a frequency-divided signal is obtained

$$A_5 = \cos\left[\frac{1}{2}(2\omega_l t - 2\omega_l \tau + 2\varphi_l)\right] = \cos(\omega_l t - \omega_l \tau + \varphi_l) \quad (10)$$

Finally, an electrical mixer is used to apply frequency mixing between A_4 and A_5 , which is given by

$$\begin{aligned} A_6 &= \cos(\omega_l t - \omega_l \tau + \varphi_l) \cdot \cos[(\omega_l + \omega_r)t - \omega_r \tau + \varphi_l + \varphi_r] \\ &\propto \cos[\omega_r t - (\omega_r - \omega_l)\tau + \varphi_r] \end{aligned} \quad (11)$$

As can be seen from Eq. (11), if the angular frequency of the local RF signal is identical to that of the remoted RF signal, i.e., $\omega_l = \omega_r$, Eq. (11) can be rewritten as

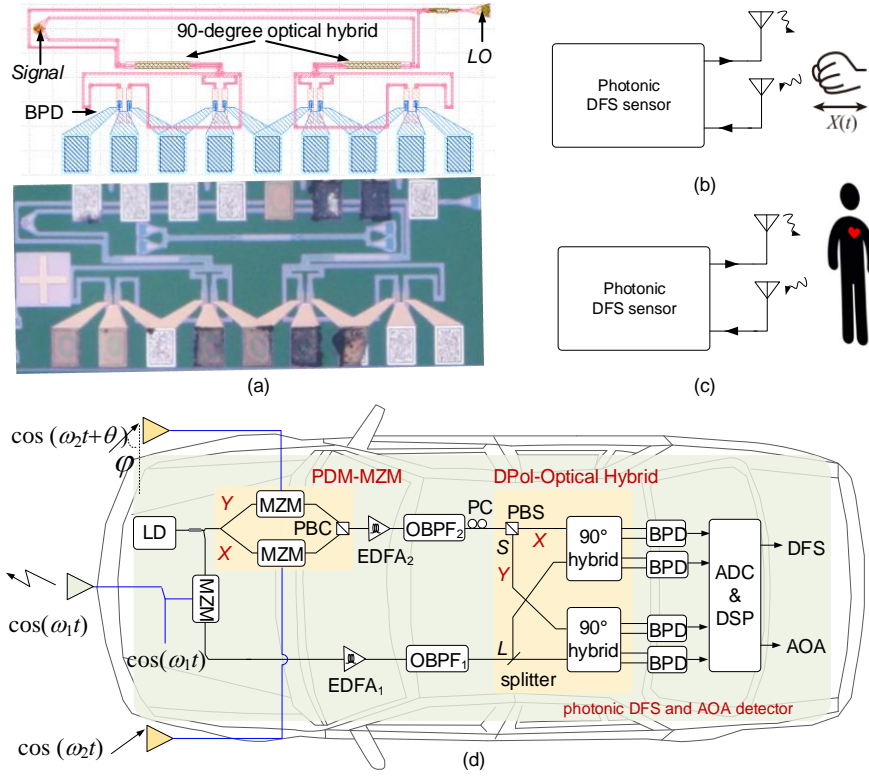


Fig. 5.5. Future work of coherent receiver. (a) dual-polarization coherent receiver, and applications of photonic DFS measurements. (b) human gesture monitoring system, (c) heart rate monitoring system and (d) DFS & AoA measurement for automotive radar (figure from [15]).

$$A_6 = A_2 = \cos(\omega_r t + \varphi_r) \quad (12)$$

Obviously, the frequency and the phase of A_6 obtained in the local site equal to that of A_2 in the remote site, indicating that phase stable RF transmission is achieved from the remote site to the local site.

In Chapter 4, a photonic DFS measurement system based on a single-polarization coherent receiver is proposed. On the one hand, to make use of the freedom of polarization, the coherent receiver can be extended to a dual-polarization coherent receiver [11, 12]. Fig. 5.5(a) shows the layout and picture of such a dual-polarization coherent receiver. Unlike the single-polarization coherent receiver, a polarization-division-multiplexed coupler is

used to separate the *Signal* light into two orthogonal branches, and an optical splitter is used to split the *LO* light into two portions. Then, each *Signal* light is combined with each *LO* light by an MMI-based 90-degree optical hybrid. Finally, two pairs of BPDs are connected to the outputs of the MMI to realize photodetection along the two orthogonal polarization directions. The dual-polarization coherent receiver is under measurement, and detailed results will be presented in our future work.

Moreover, in this thesis, only the DFS measurement is performed. In the future work, the attentions can be paid to the actual DFS sensing applications based on the coherent receiver. For example, Fig. 5.5(b) shows a schematic diagram of a human gesture monitoring system based on the photonic DFS measurement [13]. In this system, the DFS resulted from the changing of the human gestures can be monitored, which is of importance for the scenarios such as somatosensory games, securities, and so on. Fig. 5.5(c) shows another application of human heart rate monitoring based on photonic DFS measurement [14]. The DFS information obtained by the proposed system can be used to know the situation of the patients. Finally, if the dual-polarization coherent receiver is available, a photonic-based system that can measure both the DFS and angle of arrival (AoA) of a moving target could be implemented, which is shown as Fig. 5.5(d). A proof-of-concept experiment based on fiber-optic devices was previously demonstrated by myself [15]. The DFS information is obtained from the *x*-polarization branch, and the AoA information is acquired by comparing the phase difference of the IF signals obtained from the *x*-polarization and *y*-polarization branch, respectively.

Reference

- [1] M. Song, L. Zhang, R. G. Beausoleil, and A. E. Willner, "Nonlinear Distortion in A Silicon Microring-Based Electro-Optic Modulator for Analog Optical Links," *IEEE Journal of Selected Topics in Quantum Electronics*, vol. 16, no. 1, pp. 185-191, 2009.
- [2] L. Chen, J. Chen, J. Nagy, and R. M. Reano, "Highly Linear Ring Modulator from Hybrid Silicon and Lithium Niobate," *Optics Express*, vol. 23, no. 10, pp. 13255-13264, 2015.

- [3] A. Hosseinzadeh and C. T. Middlebrook, "Highly Linear Dual Ring Resonator Modulator for Wide Bandwidth Microwave Photonic Links," *Optics Express*, vol. 24, no. 24, pp. 27268-27279, 2016.
- [4] J. Cardenas et al., "Linearized Silicon Modulator Based on A Ring Assisted Mach-Zehnder Inteferometer," *Optics Express*, vol. 21, no. 19, pp. 22549-22557, 2013.
- [5] S. Agarwal, M. Ingels, M. Pantouvaki, M. Steyaert, P. Absil, J. Van Campenhout, "Wavelength Locking of a Si Ring Modulator Using an Integrated Drop-Port OMA Monitoring Circuit," *IEEE J. Solid-State Circuits*, vol. 51, no. 10, pp. 2328-2344, Oct. 2016.
- [6] X. Zheng et al., "A High-Speed, Tunable Silicon Photonic Ring Modulator Integrated with Ultra-Efficient Active Wavelength Control," *Optics Express*, vol. 22, no. 10, pp. 12628-12633, 2014.
- [7] I. Giuntoni, A. Gajda, M. Krause, R. Steingrüber, J. Bruns, and K. Petermann, "Tunable Bragg Reflectors on Silicon-On-Insulator Rib Waveguides," *Optics Express*, vol. 17, no. 21, pp. 18518-18524, 2009.
- [8] J. Wu, T. Moein, X. Xu, and D. J. Moss, "Advanced Photonic Filters Based on Cascaded Sagnac Loop Reflector Resonators in Silicon-On-Insulator Nanowires," *APL Photonics*, vol. 3, no. 4, p. 046102, 2018.
- [9] M. Calhoun, S. Huang, and R. L. Tjoelker, "Stable Photonic Links for Frequency and Time Transfer in The Deep-Space Network And Antenna Arrays," *Proceedings of the IEEE*, vol. 95, no. 10, pp. 1931-1946, 2007.
- [10] J. Wei, F. Zhang, Y. Zhou, D. Ben, and S. Pan, "Stable Fiber Delivery of Radio-Frequency Signal Based on Passive Phase Correction," *Optics Letters*, vol. 39, no. 11, pp. 3360-3362, 2014.
- [11] K. Roberts et al., "Performance of Dual-Polarization QPSK for Optical Transport Systems," *Journal of Lightwave Technology*, vol. 27, no. 16, pp. 3546-3559, 2009.
- [12] C. R. Doerr et al., "Monolithic Polarization and Phase Diversity Coherent Receiver in Silicon," *Journal of Lightwave Technology*, vol. 28, no. 4, pp. 520-525, 2010.
- [13] T. Fan et al., "Wireless Hand Gesture Recognition Based on Continuous-Wave Doppler Radar Sensors," *IEEE Trans. Microw. Theory Techn.*, vol. 64, no. 11, pp. 4012-4020, Nov. 2016.

- [14] M. Nosrati and N. Tavassolian, "High-Accuracy Heart Rate Variability Monitoring Using Doppler Radar Based on Gaussian Pulse Train Modeling and FTPR Algorithm," *IEEE Trans. Microw. Theory Techn.*, vol. 66, no. 1, pp. 556-567, Jan. 2018.
- [15] Z. Z. Tang and S. L. Pan, "Simultaneous Measurement of Doppler-Frequency-Shift and Angle-of-Arrival of Microwave Signals for Automotive Radars," in *2019 IEEE International Topical Meeting on Microwave Photonics*, Oct. 7-10, 2019, Ottawa, Canada.

